## **Producing photocatalytic Titania Surfaces with Direct Laser Interference Patterning (DLIP)**

### **Dissertation**

zur Erlangung des Grades des Doktors der Ingenieurwissenschaften der Naturwissenschaftlich-Technischen Fakultät III Chemie, Pharmazie, Bio- und Materialwissenschaft und Werkstofftechnik der Universität des Saarlandes



von

**Tobias Fox** 

Saarbrücken

März 2025

Tag des Kolloquiums: 22.08.2025

Dekan: Prof. Dr.-Ing. Dirk Bähre

Berichterstatter: Dr.-Ing. Florian Schäfer

Vorsitz: Prof. Dr. Guido Kickelbick

Akad. Mitarbeiter: Dr.-Ing. Florian Schäfer

"As I contemplate what is, I dive ever deeper into the depths of possibility.

Then I set an experiment in motion and watch the truth rise to the surface."

- Gyre Engineer

### **Abstract**

This work investigates a novel approach to produce photocatalytic surfaces via ultrashort pulsed direct laser interference patterning of titanium. The interference pattern caused by two laser pulses results in a periodic intensity distribution that leads to localized ablation on the µm scale. This ablation leads to the creation of complex surface geometries, surface oxidation and redeposition of titanium oxides. Using this approach, surfaces with varying phase composition and topography are produced aiming to achieve high photocatalytic activity. Based on the analysis of the resulting surfaces and their formation mechanism, it was concluded that heat treatments during and after the patterning could further increase the photocatalytic activities of the resulting surfaces.

Finally, promising pattern parameters are used to produce a prototype to demonstrate the approach's feasibility for water treatment. To simulate the removal of pollutants from water, 1.5 litres of an organic dye solution (methylene blue) were treated in a reactor built with off-the-shelf materials. It could be shown that the prototype achieves degradation rates similar to the lab setup when accounting for active surface area and UV irradiance. This shows that DLIP poses a viable alternative to existing approaches for the creation of photocatalytic surfaces and could be used for water purification, self-cleaning and antifouling surfaces and possibly antimicrobial implants.

### Zusammenfassung

Diese Arbeit untersucht die Herstellung photocatalytischer Oberflächen mittels ultrakurz gepulster direkter Laserinterferenzstrukturierung von Titan. Das bei DLIP erzeugte Interferenzmuster führt zu lokaler Ablation im µm-Bereich bewirkt und damit zur Entstehung komplexer Oberflächengeometrien, zur Oxidation und zur Rückablagerung von Titanoxiden. Dadurch werden Oberflächen mit unterschiedlicher Phasenzusammensetzung und Topographie erzeugt, um eine hohe photocatalytische Aktivität zu erzielen. Basierend auf der Analyse der resultierenden Oberflächen und ihres Entstehungsmechanismus wurde untersucht, ob Wärmebehandlungen während und nach der Strukturierung die photocatalytische Aktivität der resultierenden Oberflächen weiter steigern können.

Schließlich wurden vielversprechende Parameter genutzt, um einen Prototyp zur Demonstration für die Wasseraufbereitung herzustellen. Dazu wurden 1,5 Liter einer organischen Farbstofflösung (Methylenblau) in einem Reaktor behandelt, der aus handelsüblichen Materialien gebaut wurde. Es konnte gezeigt werden, dass der Prototyp Abbauraten erzielt, die - normiert auf die aktive Oberfläche und die UV-Bestrahlung - mit denen im Labor vergleichbar sind. Dies zeigt, dass DLIP eine vielversprechende Alternative zu bestehenden Verfahren zur Herstellung photocatalytischer Oberflächen darstellt und für die Wasseraufbereitung, selbstreinigende und Antifouling-Oberflächen sowie möglicherweise für antimikrobielle Implantate eingesetzt werden könnte.

### Acknowledgements

I want to start by thanking Professor Mücklich for the possibility of writing this thesis at his institute, for his continuous trust in my abilities and for his guidance throughout the process. I am deeply grateful for the professional research environment and the vast suite of possibilities that your support enabled.

On that note, I would also like to thank the entire team at the institute for the excellent work environment, uncountable valuable discussions, and the good times they helped to create. Special thanks go to Christoph Pauly and Sebastian Suarez, who were always open to my questions and helped me navigate both scientific and organisational hurdles and to Bruno Alderete for his meticulous proofreading. Additional thanks go to Jörg Schmauch for the HR-TEM measurements and Professor Kickelbick and his team for their support regarding the many UV-Vis measurements included in this thesis. I would also like to express sincere gratitude to Professor Busch for his role as my second reviewer.

This work would furthermore not have been possible without all the students who dedicated their theses to the topic itself or adjacent ones and thereby contributed directly via experiments and data or indirectly through general discussions and pointed questions. Namely, Pablo Delfino, Francisco Cortés and Fabian Bonner contributed to the topic directly through their master theses, while Walter Garcia, Francisco Almeida and Niklas Müller explored adjacent areas.

Finally, I want to extend my gratitude to my friends and my family who have always been a source of encouragement and joy. I am certain that without their continuous support, this work would not have been possible.

### **Table of Contents**

1		Intro	oduction	. 1
2		The	oretical Background and State of the Art	. 2
	2.1	Basi	ics of Photocatalysis	. 2
	2.2	Cha	rge Carrier Creation	. 3
	2.3 Creating Reactive Species			. 3
	2.4	Incr	easing photocatalytic Activity	. 4
	2.4.1	1	Doping	. 4
	2.4.2	2	Defect Creation	. 5
	2.4.3	3	Dye Sensitization	. 6
	2.4.4	1	Metal Particles	. 6
	2.4.5	5	Combining Semiconductors	.7
	2.4.6	5	Employing hierarchical Structuring	. 8
	2.5	Mix	ed Phases and Heterojunctions	10
	2.6	Proc	ducing photocatalytic Surfaces	10
	2.6.1	l	Thermal Oxidation	10
	2.6.2	2	Anodization	10
	2.6.3	3	Hydrothermal Processing	11
	2.6.4	1	Sol-Gel methods	11
	2.6.5		Deposition of prefabricated nanoparticles	11
	2.6.6	5	Laser-based Techniques	11
	2.6.7		Direct Laser Interference Patterning (DLIP)	12
	2.7	Effe	ects of laser radiation on titanium and its oxides	14
	2.8	Sun	nmary	16
3		Obje	ectives	16
4		Methods		
	4.1	Sam	pple Preparation	18
	4.2	Dire	ect Laser Interference Patterning (DLIP)	18
	4.3	Con	focal Laser Scanning Microscopy	18
	4.4		nning Electron Microscopy (SEM), Focused Ion Beam (FIB) and Energies X-ray spectroscopy (EDS)	
	4.5	X-R	ay Diffraction (XRD)	19
	4.6	Met	hylene Blue Degradation and UV-Vis Spectroscopy	19
5		Resi	ults	21
6		Unp	oublished Results	55
	6.1	Mas	ster Thesis Walter Garcia	55
	6.2	Bac	helor and Master Theses Niklas Müller	56

6.3	M	aster Thesis Francisco Udo Almeida	56
6.4	TI	EM-Analysis	57
6.4	4.1	Selected Area Electron Diffraction (SAED)	57
6.4	4.2	HR-TEM	58
7	Co	onclusions and Outlook	59
8	Bi	bliography	61

### 1 Introduction

Over the course of the last decades, solar power has emerged as one of the most efficient and promising approaches to power humanity's energy needs and enable the transition from fossil fuels to renewables. The ability of semiconducting materials to produce electric currents and thereby power our industries and homes has somewhat overshadowed the surprising abilities of another set of photoactive semiconductors. Materials like TiO<sub>2</sub>, ZnO and CdS are also able to produce charge carriers when irradiated by the sun. However, in contrast to the carriers generated in solar panels, these carriers have an electric potential that is high enough to directly split water or engage in other chemical reactions with surrounding media. This means that the material can directly influence the surrounding chemistry when it is irradiated by a suitable light source. [1-3]The most relevant reaction in that regard is the splitting of water and the subsequent production of hydrogen and/or a large variety of reactive oxygen species (ROS) like H<sup>+</sup>,  $O_3^-$  or the extremely reactive hydroxyl radical (OH). These reactive radicals can subsequently degrade most organic contaminants. For this reason, photocatalytic materials have been used to clean heavily polluted waters or to produce self-cleaning and antifouling surfaces. [2,4–6] The potential to directly produce hydrogen has also drawn attention as an alternative to electrolytic water splitting. The Australian company "Sparc Hydrogen" is currently investigating the scalability of the approach using large-scale test reactors. [7] Additionally, photocatalytic materials have the potential to reduce CO<sub>2</sub> and nitric oxides from the air which could be of great use to combat climate change and to improve the air quality in cities. [1,8,9] To this day, titanium dioxide remains the most relevant material for photocatalysis as it is highly efficient, chemically stable, abundant and relatively easy to manufacture.

However, for all this potential TiO2 comes with a number of drawbacks. First and foremost, its large bandgap energy of around 3 eV. As a result, light in the UV range is required to initiate charge carrier creation meaning that a large part of the solar spectrum cannot be utilized. Current approaches to address this issue mainly focus on doping, the creation of lattice defects, and the formation of an efficient mix of different titanium oxides. [5,10–12] A second challenge to the widespread application of TiO<sub>2</sub> is the large surface area required for high activities which favours the widespread use of nanoparticles. The problem with this approach lies in the applicability of those particles in the real world. For water treatment, nanoparticles show great potential to degrade contaminants but finding a way to efficiently remove them from treated water has proven to be challenging. [13–15] To avoid this issue, the photocatalytic layer can be produced as a surface coating. This approach avoids the need to remove the active agents from the solution and opens applications like antifouling or antimicrobial surfaces. The coating processes however generally require either nanoparticles as precursors that are then applied to the surface or alternative processes that come with drawbacks like the need for complex reactors, harmful chemical agents, and challenging process control. [16,17] particle-containing coatings have drawn a lot of attention especially in the form of photocatalytic paints. For such paints the loss of particles to the environment (chalking) and as a result the loss of functionality presents a major problem as the binder itself is oftentimes suspect of photocatalytic degradation. [18–21]

This work investigates an alternative approach to produce photocatalytic surfaces that in contrast to established methods, utilizes no nanoparticles, precursors, chemical agents or multi-step methods. Instead, a single laser treatment is performed to produce a porous hierarchical surface structure consisting of various titanium oxides. The high surface area and complex oxidic structure produced in this single processing make this approach very promising for the large-scale production of photocatalytic surfaces.

### 2 Theoretical Background and State of the Art

### 2.1 Basics of Photocatalysis

That many polymers become brittle if exposed to the sun for too long is a phenomenon, that most people know from everyday life. Similarly, the sun's UV radiation will bleach most organic paints if given enough time. The underlying destruction of molecules by light is called photolysis, a widely known phenomenon where light (usually sunlight) breaks down complex particles into simpler ones. In the field of photocatalysis this effect is complemented by a catalyst that absorbs the photons and facilitates the breakdown of surrounding media without being used up itself. The effect has first been described in 1972 by Fujishima and Honda [22] in titanium dioxide and has since then been observed in various semiconducting materials that share common features, such as a relatively large bandgap, chemical stability, and the ability to create reactive oxygen species when in contact with water. As described by Yuan et al. [23] the utilized materials include metal oxides like TiO<sub>2</sub> and ZnO, sulphides like CdS and even selenides, oxynitrates and organic molecules. Despite the plentiful newer options, TiO<sub>2</sub> remains one of the most investigated photocatalysts as it shows a good photocatalytic performance, is chemically very stable and abundantly available. Additionally, its inertness and non-toxicity are hugely beneficial regarding its practical use. As the focus of this work lies on titanium oxide based photocatalysts, the following sections will primarily focus on these materials, while alternative approaches are only briefly mentioned in the suitable sections.

The key requirement for a photocatalytic material is semiconducting behaviour with a bandgap that is sufficiently large to split water and create reactive oxygen species (ROS). These ROS can then break down any complex molecules in the surrounding media which enables the degradation of organic pollutants, nitric oxides, sulfides, and other potentially harmful pollutants like methane. Additionally, when an electric potential is applied, the process can be tailored for carbon capture from CO<sub>2</sub> as well as green hydrogen production. [2,24–26]

When simplified, the photocatalytic process can be broken down into three process steps as depicted in Figure 1. First, a photon with sufficiently large energy must be absorbed by the material in order to create an electron-hole pair. These charge carriers must then avoid recombination and reach the material surface. There they then need to either directly degrade any adsorbed pollutants or as is more common, react with surrounding water to create the aforementioned reactive oxygen species. Those ROS can then, get in contact with the surrounding pollutants to achieve efficient degradation.

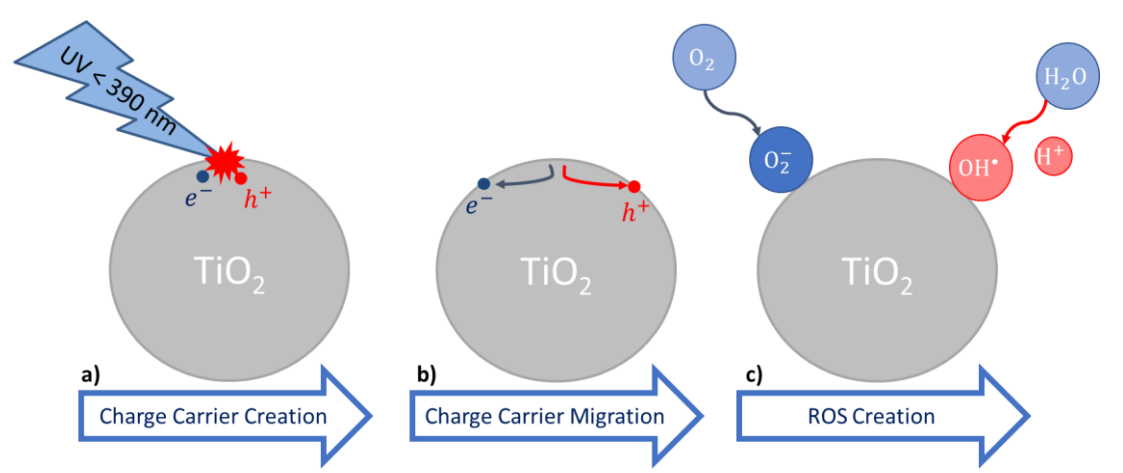


Figure 1: Overview of critical phases in photocatalysis: a) Charge carrier creation by UV-radiation, b) charge carrier separation and migration to the surface, c) reaction with surrounding media and formation of reactive oxygen species.

The following sections will first provide a brief overview of charge carrier and ROS creation before detailing how each step of the photocatalytic process can be improved.

### 2.2 Charge Carrier Creation

When a photon with an energy larger than a semiconductor's bandgap energy is absorbed, it can produce an electron-hole pair. For most photocatalytic materials, the energy required to overcome the bandgap energy lies in the range of 2.3 eV to 5 eV which corresponds to required wavelengths between 540 nm and 248 nm. This relatively large bandgap is required to ensure that the level of the conduction band lies below 0 eV to enable the creation of  $H^+$  while the valence band level lies above 1.23 eV to make the formation of  $O_2$  possible. [23] However, for the creation of the most effective water-based radicals, the hydroxyl and the superoxide radicals ('OH and  $O_2^-$ ), it is not only necessary that the bandgap is larger, it must also be ensured that the valence and conduction bands have sufficient oxidative and reductive potentials. As a result, the valence band must be at least at 2.29 V to enable the formation of 'OH and the conduction band must lie at -0.33 V or lower.

Anatase TiO<sub>2</sub> with its bandgap energies of 2.69 V and -0.51 V not only fulfils these requirements but also overshoots which results in a relatively large bandgap of 3.2 eV. [2] The second relevant TiO<sub>2</sub> phase Rutile only shows a slightly smaller bandgap of 3.0 eV. These bandgap energies are comparatively high and correspond to photon energies in the UV-range (413 nm and 387 nm respectively). Although the bandgap energy of anatase is larger than that of rutile, anatase's photocatalytic activity is much higher. One major reason for this lies in the bandgap structure of both materials. While rutile has a direct bandgap, anatase's bandgap is indirect. Therefore, the electrons and holes can only recombine in anatase if additional momentum is supplied by a suitable phonon. This dramatically increases the lifetimes and diffusion lengths of charge carriers in anatase compared to those in rutile, where recombination can occur much more easily.

Additionally, rutile has a much lower concentration of active sites on its surface. This means that there are relatively few locations on the surface where water or other molecules can adsorb and interact with the charge carriers produced in the semiconductor. This greatly reduces the material's activity as it makes it less likely that charge carriers participate in chemical reactions at the material surface and more likely that they will eventually recombine. The passivation layer that forms on titanium surfaces due to exposure to atmospheric oxygen generally consists of amorphous TiO<sub>2</sub> with a thickness of 5-10 nm where the lower layers show a decrease in oxygen concentration. As amorphous TiO<sub>2</sub> shows an extremely low charge carrier mobility it is generally considered inactive.[27–29]

### 2.3 Creating Reactive Species

When electrons and holes reach the material surface, they can reduce and oxidize surrounding molecules. Although this can lead to the direct degradation of adsorbed pollutants, it is generally much more likely that the charge carriers combine with adsorbed water and thereby kickstart a variety of possible reaction paths depicted in Figure 2. Many of those reactive species like the hydroxyl radical ( ${}^{\bullet}$ OH) and the superoxide ( ${}^{\bullet}$ O ${}^{-}$ ) are highly reactive and can even degrade resistant organic compounds or nitric oxides. The  ${}^{\bullet}$ OH radical, in particular, plays a huge role in the atmosphere as it is generated by the interaction of sunlight with ozone and degrades a wide variety of potentially harmful gases like  ${}^{\bullet}$ CO<sub>2</sub>, methane and the fluorine based PFCs. [2,30]

An overview of the various reaction pathways and the reactive species they can produce is given in Figure 2. After a photon is absorbed (1) an electron hole pair is created and potentially recombines shortly after (2). Alternatively, the hole can reach the material

surface and combine with an electron delivered from an electron donor in the surrounding medium (3). If no such donor is encountered the holes will generally oxidise surrounding water molecules, either completely to form O<sub>2</sub> and H<sup>+</sup> (4) or incompletely leading to the formation of hydroxyl radicals (5). In Figure 2, the electrons in the conduction band were either photoexcited or injected via dye sensitization (12) which is discussed in the next section. Similarly to the holes, these electrons can either combine with a suitable electron acceptor (6) or react with water to form a variety of reactive species like H<sub>2</sub>O<sub>2</sub>, 'OH and OH<sup>-</sup> (9;10;11). Alternatively, the electrons can combine with the H<sup>+</sup> ions formed by the oxidation processes to regenerate H<sub>2</sub> and water (7;8). The created reactive species can then scavenge for pollutants, although it has been shown that especially the 'OH radical tends to stay close to the material surface. [2,4]

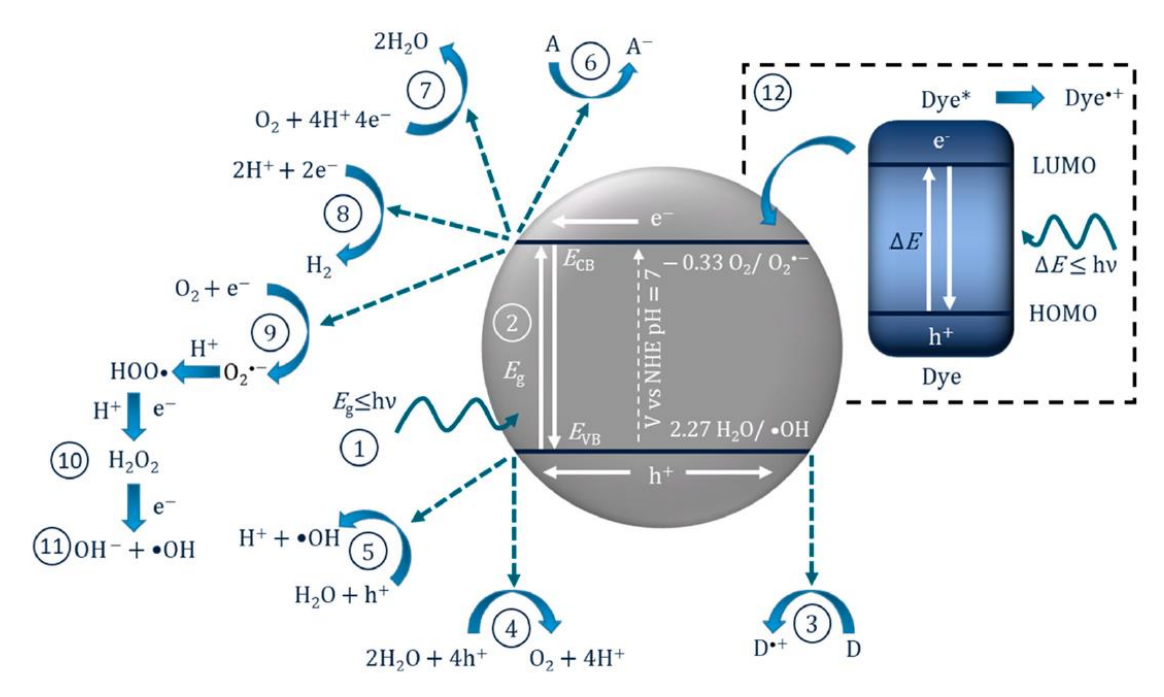


Figure 2: Overview of the reaction paths in water and the resulting reactive species during photocatalysis (reproduced from McMichael et al. 2021). [2]

### 2.4 Increasing photocatalytic Activity

As a result of the large bandgap and the resulting absorption band in the UV-range, only about 5% of the sunlight's energy can actually be utilized by pure TiO<sub>2</sub>. Additionally, a relatively large percentage of charge carriers recombine before reaching the material surface. Therefore, there exists a variety of approaches to both increase the percentage of absorbed sunlight by altering the bandgap energy of the semiconductor and to improve charge carrier separation to ensure they reach the material surface without recombination. The following section will provide a brief overview of the techniques implemented to improve photocatalytic activity in this regard.

### 2.4.1 *Doping*

Doping probably constitutes the most intuitive approach to influence the bandgap of a semiconductor as the effective size of the bandgap can be influenced as depicted in Figure 3. The photocatalytic activity of TiO<sub>2</sub> can be increased by doping it with Fe, Mo, Ru, Os, V, Rh, N and S while doping with Co and Al has shown to decrease the activity. [31,32] As this behaviour indicates, a decrease in bandgap energy and the resulting shift of the absorption band towards visible wavelengths does not automatically lead to increased

activity. The reason for this lies in the individual nature of the dopant and his behaviour regarding charge carriers. Some dopants, like Al and Co, can act as trapping and recombination sites for charge carriers meaning electrons and holes are less likely to reach the surface of the material and more likely to become trapped at a dopant and recombine there. For the same reason, a dopant concentration that is too high will also decrease the activity as the benefit of a decreased bandgap energy is eventually mitigated by the increased number of crystal defects and, consequently, trapping sites.

However, if employed correctly, doping can broaden the absorption band, increase charge carrier creation and even influence the reactive species that are eventually created at the material surface. This is because dopants can influence if the TiO<sub>2</sub> behaves like a n- or a p-type semiconductor. The electric field within a n-type photocatalysts will push any generated holes towards the material surface and the electrons deeper into the material. This effect not only reduces recombination but can also lead to an increased formation of hydroxyl radicals. The opposite is true if a p-type photocatalyst is used. It should be noted, however, that this is only true if the material exists in the form of a conductively connected electrode as it is not possible to produce a significant surplus of one charge carrier if the system is insulated. [11,32–34]

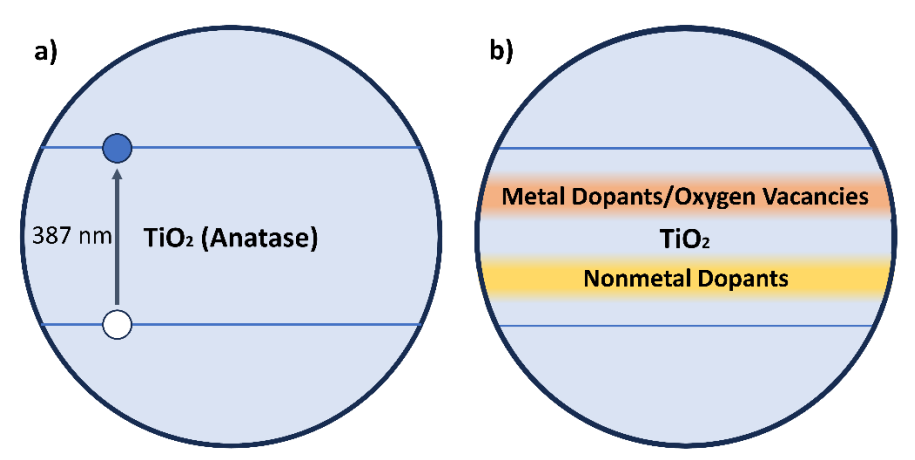


Figure 3: Charge charrier creation in pure anatase (a) and the influence of dopants on the bandgap structure of TiO2 (b)

### 2.4.2 Defect Creation

An alternative to doping is the creation of defects in the TiO<sub>2</sub> lattice. These defects include self-doping, oxygen vacancies, Ti-H bonds, and surface hydroxyl groups. Various chemical modifications, such as high-pressure hydrogenation or the reaction with Mg, have shown to produce such defects in the outer layers of the material. The result is creation of additional possible states in the conduction band and thereby a reduced bandgap energy which can greatly increase the material's absorption spectrum into the visible range, resulting in grey or even black titania. However, as the crystal defects also constitute potential trapping sites and recombination centres there is no direct correlation between increased solar absorption and increased photocatalytic activity. In general, some amount of crystal defects can be seen as desirable while too many defects promote recombination or even reduce the bandgap to an extent that the electric potential is no longer sufficient to produce reactive species. [12,24,35]

An alternative to chemical processing routes is pulsed laser irradiation with UV pulses in the nanosecond range. This has been applied to nanoparticles in aqueous solution as well as photocatalytic films. In both cases, the laser irradiation creates a defect-rich, oxygendeficient TiO<sub>2-x</sub> crystal on the material surface that presents a reduced bandgap energy and therefore enables light harvesting in the visible range. [36–38]

### 2.4.3 Dye Sensitization

Organic dyes that absorb in the visible range can be used to directly inject charge carriers into the photocatalyst's conduction band. This is possible as the injection usually occurs on a femtosecond timescale while the recombination of change carriers within the dye ranges in the nanoseconds to even milliseconds. However, an appropriate dye needs not only to absorb a suitable range of wavelengths but also to produce electrons with enough energy that they can be injected into the conduction band of TiO<sub>2</sub>. Such dyes have been shown to cause a major increase of photocatalytic activity especially under visible light which makes them very appealing especially for the green generation of hydrogen. However, self-degradation of the dyes is the main drawback of this approach as the organic molecules themselves can be attacked and destroyed by the produced radicals. This process is further amplified by the fact that for the electron injection to work, the dye needs to be adsorbed directly onto the photocatalysts surface. There exists a variety of approaches to overcome this problem such as the use of sacrificial agents or various redox systems. [11,39]

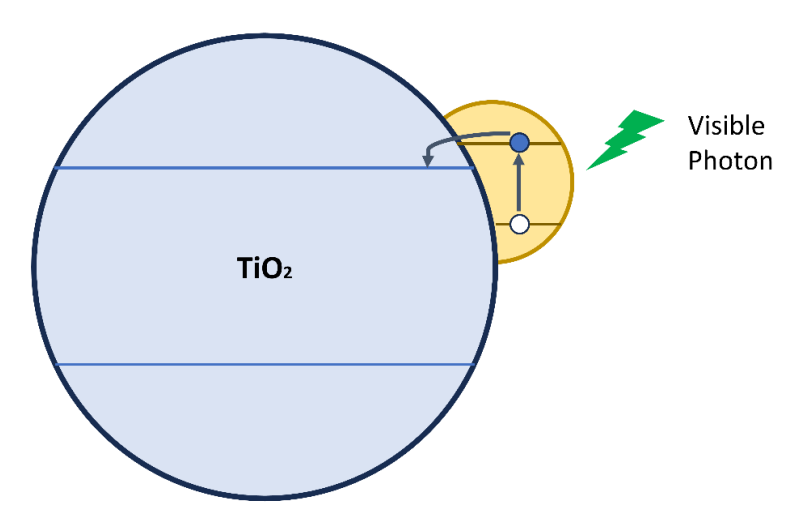


Figure 4: Dye molecule injecting a photogenerated electron into the conduction band of TiO2

### 2.4.4 Metal Particles

In addition to being efficient dopants, various noble metals like Au, Ag, and Pt can increase the photocatalytic activity when added to the system in the form of nanoparticles. This can be explained by the Fermi levels of those metals which are lower than that of TiO<sub>2</sub>. As a result, if the metal particle is conductively attached to the TiO<sub>2</sub>, it attracts the photogenerated electrons while the nature of the resulting Schottky contact does not allow for holes to pass. This leads to an efficient separation of electrons and holes thereby reducing recombination and increasing activity.

An additional beneficial effect is the improved light harvesting enabled by respectively designed nanoparticles. This behaviour is based on the plasmonic resonance, which occurs when appropriately sized nanoparticles interact with light. The generated surface plasmons can lead to an injection of charge carriers into the photocatalytic semiconductor. In this manner the metallic nanoparticle can act similarly to the aforementioned dyes by effectively increasing the material's absorption as a whole and enable photocatalytic activity at higher wavelengths. In contrast to the first mechanism this process has even been shown to work if there is an insulating layer between metal and semiconductor as the plasmon within the metal "antenna" can create a sufficiently large field to create an electron hole pair in the semiconductor. [11,40]

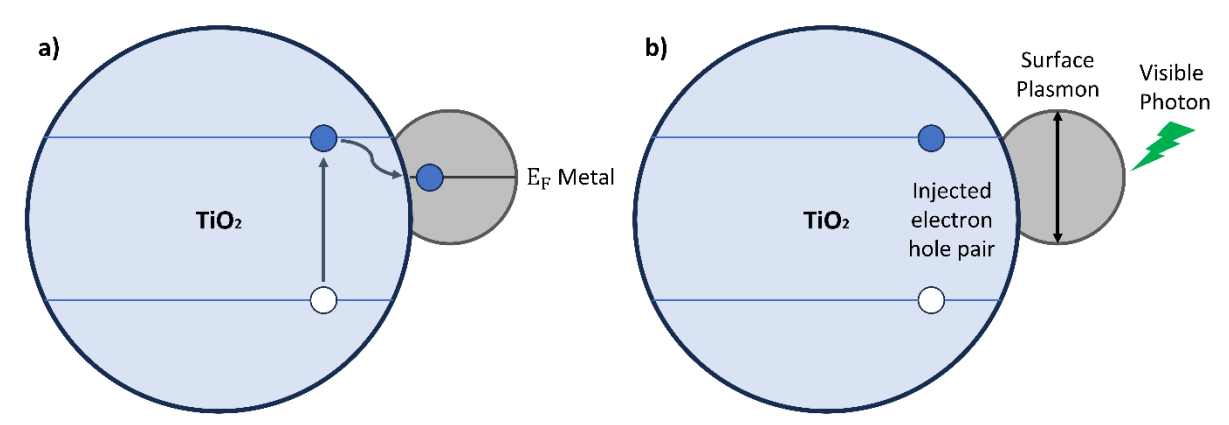


Figure 5: Effects of metal particles as electron traps (a) and antennae generating charge carriers (b)

### 2.4.5 Combining Semiconductors

Semiconductors like CdS, with a bandgap energy of only 2.4 eV can be used to increase the activity of TiO<sub>2</sub> as they, similarly to the organic dyes, enable the absorption of visible light (540 nm for CdS) and then lead to the injection of charge carriers into the TiO<sub>2</sub>. Similarly, to the organic dyes these systems are affected by self-degradation and photocorrosion if there are no suitable hole scavengers present to absorb the holes in the CdS.

However, the combination of different semiconductors can also lead to an increase in activity if both show a relatively large bandgap. Perhaps the simplest example of this is the combination of the two most common TiO<sub>2</sub> phases rutile and anatase. While they possess similar bandgap energies (3.2 eV and 3.0 eV) their combination has shown far higher activity than the individual phases. The reason for this can be explained using Figure 6. As both the valence and conduction bands of each semiconductor are shifted with respect to those of the other, generated charge carriers experience a potential difference that causes the migration of electrons towards rutile and of holes towards anatase. This results in an effective separation of charge carriers as long as they are created sufficiently close to the interface of the two semiconductors. It should be noted that a conductive connection (type 2 heterojunction) between the phases is required for this transfer to occur as a mixture of both phases without a heterojunction will generally result in an activity equal to the weighted average of both phases. The exact pathway of this process is not yet entirely clarified as several authors have observed reversed electron-hole migrations, i.e., electrons moving from rutile to anatase. [21,25,31,41–43] Other semiconductors with large bandgaps, like ZnO (3,4 eV) and SnO<sub>2</sub> (3.5 eV) can also be used for this effect; however, the most commonly used commercially available photocatalytic nanomaterial Evonik AEROXIDE® consists of a mixture of about 70% anatase and 30% rutile. [11,44–46]

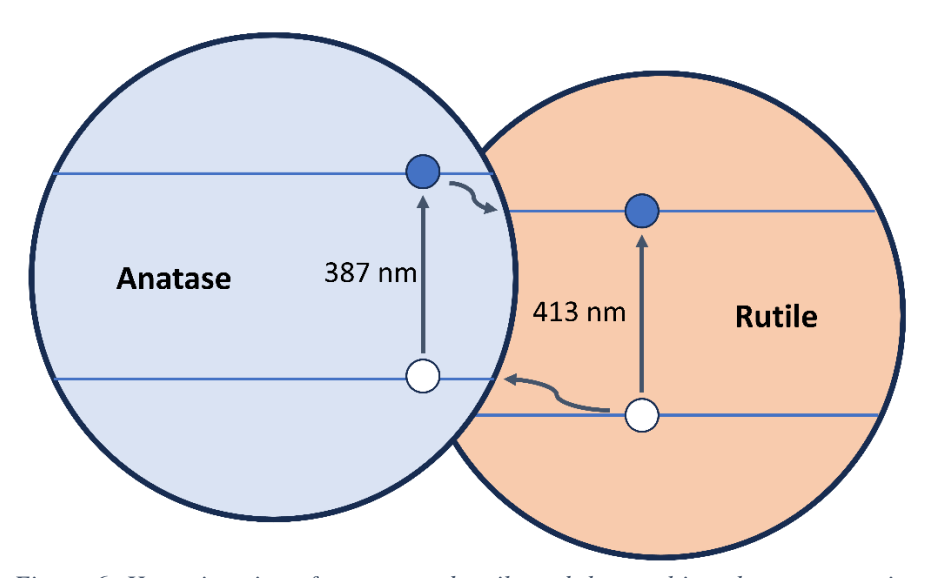


Figure 6: Heterojunction of anatase and rutile and the resulting charge separation. While this bandgap configuration is widely observed, some studies indicate a reversed situation in which rutile's bandgap lies higher than that of anatase.

The combination of rutile and anatase has not only proven beneficial for nanoparticles but has also shown be effective in surfaces. Kawahara et al. [47] deposited stripes of anatase onto a rutile film and demonstrated an increase in activity for the combined surface. They additionally observed that the distance between those stripes influenced the activity of the surface with a decrease in line distance resulting in an increase in activity. However, the efficient production of both phases in the coating poses a challenge as both phases need to be electrically connected while possessing a large free surface area. Generally speaking, most processing techniques, especially wet chemical ones firstly produce TiO<sub>2</sub> in its amorphous or anatase phase. However, as rutile possesses a lower Gibbs free energy than anatase at all temperatures, it is more stable and anatase transforms irreversibly to rutile at elevated temperatures. As the difference in Gibbs free energy only amounts to 2.3 kJ/mol various factors can influence the stability of both phases which is why no definite transition temperature can be given and although findings are centred around 600°C, reports range from 400°C to 1200°C. The small difference in free energy also makes it possible that anatase's smaller surface energy stabilizes anatase at particle sizes below approximately 40 nm. Similarly, anatases higher molar volume makes it so that the formation of rutile is favoured by elevated pressures. [21,48–50]

### 2.4.6 Employing hierarchical Structuring

As described in the sections above, a large surface area is crucial for photocatalysis as critical processes like light absorption, and radical creation take place at the material surface. However, other parameters like connectivity, electron mobility and exposed active sites also play an important role. While the pure surface area can be maximized by employing nanoparticles, agglomeration and sedimentation often reduce the accessibility of the surface. For this reason, hierarchical surfaces with a defined nanoscale subsurface are very promising. The following sections will highlight the various parameters that can be influenced by multiscale patterning as depicted in Figure 7.

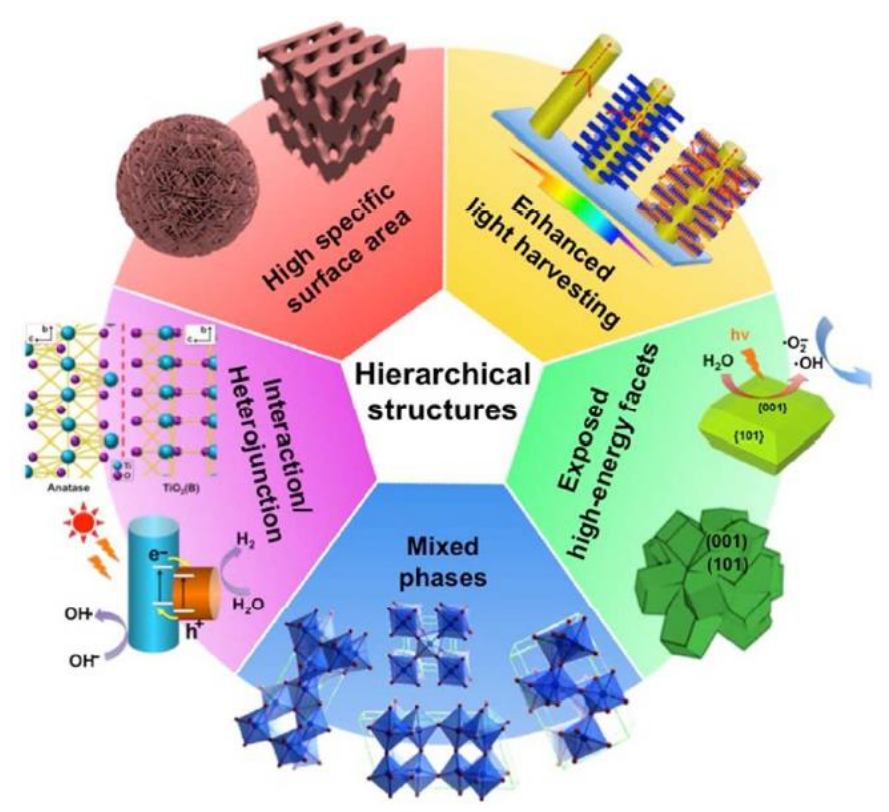


Figure 7: Schematic diagram depicting the potential benefits of hierarchical photocatalysts (reproduced with permission from Gao et al. 2015) [28]

### Surface Area

As mentioned above, a high surface area alone is not sufficient to ensure high photocatalytic activity. Instead, it must be ensured that the surface is easily accessible to both water and any pollutants that are to be degraded. To achieve this, nanoparticles of various shapes (dots, rods, spikes, plates) can be fixed onto larger spheres. As a result of their larger size, these spheres are less susceptible to van-der-Waals forces and the resulting agglomeration. Additionally, the larger particle size makes it easier to remove these particles from treated solutions.

When applied to surfaces instead of particles, the required accessibility leads to the need for open-pored systems that allow for easy water penetration while presenting a large nanoscale surface to increase the adsorption of both water and pollutants. [6,28]

### Light Harvesting

As photocatalysis relies on the absorption of photons, surface structures that increase light absorption can lead to an increase in activity as more electron-hole pairs and hence radicals are created. Light absorption can be enhanced by structures that promote multiple reflections and light trapping as the induced additional light-matter interactions lead to further absorption. A small-scale substructure that is as big or smaller than the wavelength of the relevant photons can further increase the absorption by reducing reflection losses through a gradient refractive index. [28]

### High energy Facets

Different crystallographic orientations of anatase show varying surface energies with the  $\{001\}$  orientation showing the highest with  $0.90 \text{ J/m}^2$  and  $\{101\}$  the lowest with  $0.44 \text{ J/m}^2$ . As many crucial processes like adsorption and surface reactivity are affected by the surface energy the different orientations show varying photocatalytic activities with the

{001} plane being far more reactive than the relatively stable {101} plane. Unfortunately, the high surface energy of {001} also results in the preferential formation of the more stable {101} plane. As a result, only about 5% of the exposed surface are oriented in {001} while about 94% are oriented in {101}. However, to date, the only feasible method to produce large amounts of exposed {001} facets involves hydrofluoric acid to cap the exposed facets and promote the growth of the {001} orientation. [1,28]

### 2.5 Mixed Phases and Heterojunctions

As mentioned in the "Combining Semiconductors" section, a mix of different phases can increase charge separation and thereby improve performance. For this reason, it can be beneficial to have various different phases present in the surface. However, as was also mentioned above, a conductive connection (heterojunction) between these phases must be present. Additionally, the connectivity between the two phases must be high to make sure that the distances any generated charge carrier must travel are as short as possible. [1,28,31]

### 2.6 Producing photocatalytic Surfaces

As is to be expected, there exists a large variety of synthesis methods for photocatalytic titanium oxide surfaces. These techniques can be classified into those that synthesise an active layer directly on a surface and those where pre-synthesised particles are deposited on a material surface. As the approach presented in this thesis belongs to the first class, the emphasis of this section is placed on these approaches. The second class of synthesis techniques is discussed relatively briefly at the end of this chapter.

### 2.6.1 Thermal Oxidation

The simplest approach to produce an oxygen-rich surface is the thermal treatment of titanium. While the native passivation layer that forms on titanium surfaces through contact with atmospheric oxygen is usually 5-10 nm thick and generally amorphous, thermal treatment can be used to produce thicker crystalline layers. As the most stable TiO<sub>2</sub> phase is the relatively inactive rutile phase, these surfaces are usually not photocatalytically active. By carefully choosing the treatment temperatures and times, mixtures of rutile and anatase can also be produced. These films are generally dense and have a relatively small surface area which limits their activity. [50,51]

### 2.6.2 Anodization

Anodization is commonly used to produce passivation layers or coloration effects based on the oxide layer thickness. However, depending on the electrolyte and process parameters, such as voltage and temperature, a variety of phases and even phase mixtures can be produced. Common additives for the electrolytes include hydrogen peroxide, sulfuric acid, phosphoric acid, and oxalic acid. A key feature of anodization is that it can be adapted to produce complex nanostructures such as orderly arrays of nanotubes that exhibit extremely large surface areas and high light absorption. To achieve this, the electrolyte generally consists of a mixture of fluorides, ethylene glycol or glycerol, and water. The nanotube morphology can then be controlled by the process parameters. However, the as-processed nanotubes consist of amorphous TiO<sub>2</sub> and therefore show no major photocatalytic activity unless they are post-processed e.g., by thermal treatment at 450°C for several hours. This thermal treatment can induce crystallization and even a phase mixture, but it generally also leads to a reduction in surface area as the nanotubes are partially sintered. [50,52–55]

### 2.6.3 Hydrothermal Processing

In hydrothermal processing, TiO<sub>2</sub> nanomaterials are produced from a solution containing a precursor like TiCl<sub>4</sub> and either an alkaline solution like NaOH or an acid like HCl. Together with a suitable substrate, the solution is placed in a Teflon-lined container and exposed to elevated temperatures for several hours. The samples are then usually washed with acid and annealed at 300-600°C. Depending on the process parameters, a large variety of nanomaterials such as particles, rods, sheets and flowers expressing various TiO<sub>2</sub> phases can be produced. However, as the resulting structures highly depend on the substrate parameters such as chemistry, roughness, shape and even the position of the substrate in the reactor, process control still poses a major challenge. [17,56,57]

#### 2.6.4 Sol-Gel methods

Sol-Gel methods represent a well-established group of coating techniques, such as spin coating, dip coating, or spray pyrolysis. Generally speaking, a metal-containing precursor (e.g., titanium ethoxide) is dissolved in a mixture of solvent and water leading to the formation of a gel-like material which can then be coated on a substrate using e.g., the aforementioned techniques. After the coating procedure, the solvents are left to evaporate. The result is either a thin film or a nanoparticle coating where the film thickness or nanoparticle density/size can be adjusted by the coating parameters. Additional calcination steps can be employed to alter the coating's properties like density, crystallinity, and phase. The technique is relatively simple and can be used to produce extremely thin, transparent coatings e.g., on glass surfaces that are generally less useful for photocatalytic processes than for UV protection or a tailored wetting behaviour caused by the creation of polar radicals on the surface and the resulting superhydrophilicity. While this method can also be used to produce nanoparticle coatings in fabrics that could have interesting self-cleaning properties, the loss of particles over time still presents a major issue not only because it results in a loss of functionality, but also because those particles are potentially released into the environment. [58]

### 2.6.5 Deposition of prefabricated nanoparticles

A variety of processing techniques aim to deposit a nanoparticle layer on top of a substrate. These methods include but are not limited to: dip, spin, and spray coating, electrospinning, thermal spraying as well as the use of paints and varnishes. Most of these techniques make use of a nanoparticle solution that is coated on the surfaces and subsequently evaporated. However, some methods like thermal spraying use various approaches to spray a powder, liquid, or suspension onto a material surface. Generally speaking, the film's thickness and porosity can be controlled by the process parameters. As these coating techniques are, for the most part, well established, there is a large variety of studies using these methods for various applications with commercially available or self-made nanoparticles. However, as mentioned before, the loss of porosity as a result of the coating process, as well as the loss of particles to the environment over time limit these processes especially as health concerns regarding titania nanoparticles become more prevalent. [21,59]

### 2.6.6 Laser-based Techniques

There exist several laser-based approaches to produce photocatalytic materials. The most relevant one is probably laser ablation in liquid (LAL). As the name implies, a short- or ultrashort-pulsed laser is used to ablate a titanium target, which is usually submerged in water, although other solvents are also possible. The laser then creates a confined high-pressure plasma at the material surface inside which the ablated titanium reacts with the constituents of the solvent before being quenched by the surrounding solvent. Thereby

this process presents a relatively simple approach to produce oxidic nanoparticles with various sizes and phases. Pulsed laser deposition (PLD) does not rely on a liquid and instead uses a titanium or titanium dioxide target where material is ablated and then deposited on a substrate surface. This then results in a photocatalytic film on the substrate surface. Additionally, the process can be adapted by changing the atmosphere as well as the composition of the target where additional elements like Zn or Ag can be incorporated. Matrix-assisted pulsed laser evaporation (MAPLE) is similar to PLD but uses pre-existing nanoparticles within a binder matrix as a target. The matrix material is chosen in a way that it absorbs the employed laser wavelength very well resulting in an efficient release of the loaded nanoparticles upon irradiation and their deposition on the substrate. [59–62] In 2020, Fathi-Hafshejani et al. used a nanosecond laser to directly produce both anatase and rutile on a titanium surface. The authors could control the composition of the resulting oxide by adjusting the laser parameters with anatase emerging at lower pulse overlap and rutile forming at high pulse overlap. [63,64] Medvids et al. subsequently used a similar approach to produce layers consisting of anatase or an anatase - rutile mixture but also performed photocatalytic degradation tests as well as antibacterial trials. However, their surfaces only show a minor methylene orange degradation and the high antibacterial effect may be contributed rather to the UV irradiation (125 W; 365 nm) than to the photocatalytic activity of the surfaces. [65]

### 2.6.7 Direct Laser Interference Patterning (DLIP)

Deterministic structures on the micro- and sub-microscale could be beneficial for a large variety of industrial applications in fields ranging from optical applications to electric or tribological problems or even biomedical surface structures. However, producing such structures reliably with processing speeds that are industrially relevant is still a major challenge. Direct laser interference patterning presents one option to produce periodic surface structures on the micron and sub-micron scale. To do so a laser is not focused as usual on a material to produce a pattern that is defined and also limited by the laser's focal diameter. Instead, the laser beam is split into two or more sub-beams that are then overlapped on the material's surface. As depicted in Figure 8, this results in a periodic interference pattern within the entire overlap volume. Two beams of equal intensities thereby result in a line pattern and three beams create a point pattern where the respective periodicities depend on the laser wavelength and the angles between the beams. Various other periodic interference patterns can be created by employing different beam configurations. Additional variety can be achieved by altering the intensities and polarizations of individual beams.

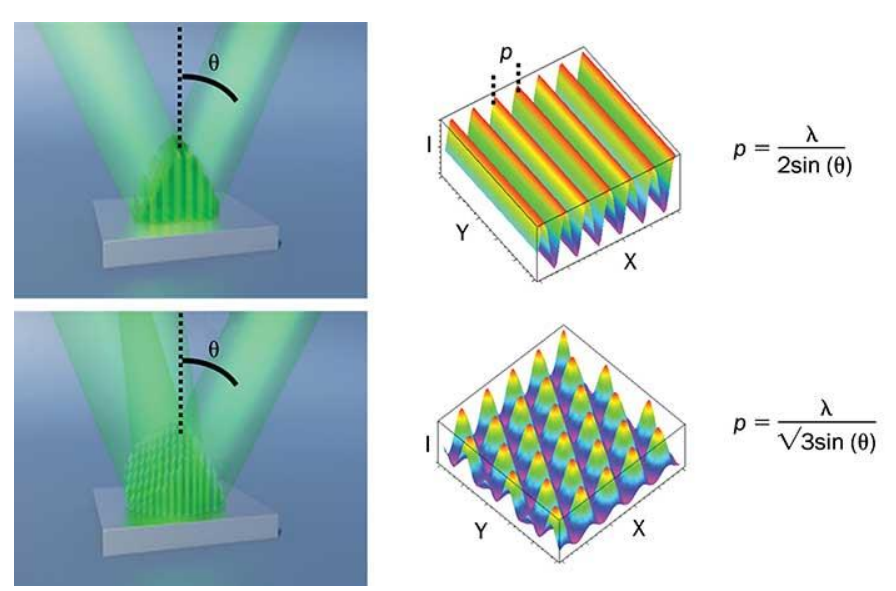


Figure 8: Intensity distributions created by two and three-beam interference as well as the respective beam configurations to achieve these distributions. Reproduced from [66]

To make use of this interference pattern, direct laser interference patterning employs powerful laser pulses to create an interference pattern with sufficiently high intensities in the interference maxima to achieve selective material processing. Most commonly, the laser is used to melt or ablate material and thereby transfer the interference pattern onto the substrate resulting in a periodic surface structure. As the interference pattern is thereby used to pattern a relatively large area with a single pulse, the process is much faster than comparable scanning techniques. Simultaneously the technique makes it possible to produce features in the micron or submicron range which is hard to achieve with a scanning approach where the feature size is limited by the employed focal diameter. [67] One crucial parameter in direct laser interference patterning is the pulse duration. For metals, the pulses in the nanosecond range generally selectively heat the material and locally cause melting or evaporation at the interference maxima. Marangoni convection then causes the molten material to move to the relatively cool areas of the interference minima. Ideally, the molten fronts from the interference maxima meet and resolidify resulting in a relatively smooth and approximately sinusoidal surface. Insufficient pulse energy can cause the molten fronts to solidify before meeting, while excessive pulse energy will result in splashes and droplets of material on the surface. Generally speaking, this process strongly affects the microstructure of the surface as the extremely fast cooling rates can lead to very mall grain sizes, metastable phases and even glass phases. Oxides generally mainly form at the surface of the resolidified material. The pattern periodicities are limited mainly by the heat conductivity of the material as especially for materials with a high thermal conductivity, heat will travel from the intensity maxima to the minima reducing the thermal gradient and thereby the driving force behind the Marangoni convection. The pattern depth is also restricted by the depth of the melt pool and fluid dynamics. On the opposite end of the spectrum, ultrashort laser pulses in the femtosecond range cause an extreme overheating at the material surface which leads to spallation of material or even direct evaporation. Therefore, the ultrashort pulses are decoupled from the materials thermal conductivity and can produce patterns in the submicron range. Additionally, relatively deep patterns are possible as the process does not rely on fluid dynamics. Instead, each laser pulse will cause ablation and the effects of multiple laser pulses will thereby add up to achieve more ablation and thereby deeper patterns. This process is limited by the fact that at some point the ablated material can no longer leave the pattern without redepositing on the walls. Additionally, at some point, the pattern

walls become so steep that the laser radiation coming from above interacts with a large area, which can ultimately cause the irradiance to fall below the ablation threshold. Generally speaking, in femtosecond laser processing, the material is ejected at very high velocities and very little molten material remains at the surface. This results in a very low amount of oxide forming at the material surface. However, a fraction of evaporated material can condense in the surrounding air and redeposit on the surface as a loosely bonded "flake-like" structure that appears almost like a snow cover when observed with a scanning electron microscope. [68–71]

For this work, a laser with a pulse duration of 10 ps was chosen. This was done because with this pulse duration higher amounts of oxide can be formed than with the femtosecond laser, and the oxides form a stronger bond with the substrate, making them far harder to remove. In contrast to the nanosecond laser pulses, the material interaction with picosecond pulses results in only minor melt formation and migration. Instead, the predominant formation mechanism is still the ablation of material, often in the form of particles or even material vapor. This made the picosecond laser an ideal candidate to investigate the formation of different stable and metastable oxides in direct laser interference patterning and the interplay of oxide chemistry and morphology with the resulting microstructure.

### 2.7 Effects of laser radiation on titanium and its oxides

Both continuous and pulsed lasers are used to oxidize titanium surfaces. The most common application for this is the production of coloured surfaces through interference effects based on the oxide layer thickness. Using various laser powers and scan speeds, a variety of different oxide thicknesses and thereby colours can be created. For continuous lasers, it was observed that these oxide films tend to consist of Ti<sub>2</sub>O, Ti<sub>2</sub>O<sub>3</sub>, TiO<sub>2</sub>, and TiN. However, especially at the material surface the titanium nitrides tend to oxidize forming TiO<sub>2</sub> and nitrogen. Slower scanning speeds and the resulting higher surface temperatures lead to higher oxygen contents and therefore the favoured formation of TiO<sub>2</sub> in both the rutile and anatase phase. As the oxygen content of these films is mainly diffusion-limited, the lower regions tend to still contain the more oxygen deficient phases. [72,73]

As described in 2.6.6, several laser-based approaches already exist to produce photocatalytically active materials from both pure titanium and TiO<sub>2</sub>. Especially in laser ablation in liquids, the extreme conditions within the confined plasma plume lead to the formation of oxidic nanoparticles expressing various phases. However, for the laser treatment under atmospheric conditions there exists much less literature. Nevertheless, several studies have shown that short and ultrashort laser pulses can produce rutile and anatase in atmospheric conditions.

Rasti et al. [74] demonstrated in 2011 that a pulsed laser (100 ns) can be used to create a mixture of anatase, rutile and hongquiite (TiO) in the surface of a titanium sample. Especially the formation of anatase was attributed to the high cooling rates of the molten phase. In fact Li et al. [75] have shown that a rapid re-solidification favours the formation of anatase despite its slightly higher Gibbs free energy. The reason for this mainly lies in the lower amount of reordering required for the formation of anatase than for the formation of rutile. Additionally, anatase's lower surface energy leads to its stability for very small particles (ca. 40 nm and below) meaning that anatase is favoured for fast nucleation processes. [21,48–50]

In a similar experiment performed by Landis et al. [76] a 100 fs Ti:sapphire laser was used to treat titanium samples under controlled atmospheres. As nitrides were only found after treatment in pure nitrogen while the samples treated in air and in pure oxygen

showed no meaningful differences, it could be concluded that the formation of oxides is prioritised over that of nitrides as long as there is oxide present. Additionally, XPS was used to show that the resulting surfaces, that showed LIPSS, expressed mainly TiO<sub>2</sub> and possibly some oxygen deficient oxides (Ti<sub>2</sub>O<sub>3</sub> and TiO). Additional XRD and Raman measurements revealed that the surfaces were of amorphous nature implying that the femtosecond pulses led to the creation of mainly TiO<sub>2</sub> but the temperatures and cooling rates during the process only allowed for the formation of an amorphous oxide film.

To examine the fundamentals of the interaction with laser pulses with amorphous TiO<sub>2</sub> Van Ovenschelde et al.[49] used a 248 nm excimer laser with a pulse duration of 25 ns to create nanoparticles within an amorphous TiO<sub>2</sub> film. They observed that in a low fluence regime, the photochemical breakage of bonds within the substrate lead to a rearrangement of the amorphous TiO<sub>2</sub> into anatase. In contrast, at higher fluences the thermal influence as well as the increased mechanical stresses favoured the formation of rutile. Similarly, Qiao et al. [43] used a near infrared laser with a pulse duration of 50 fs to initiate crystallization within amorphous TiO2 nanotubes. Their observations matched those of van Overschelde et al. in that anatase formed at lower fluences and rutile when the fluence was increased. In between, a mixture of both phases could be created. In the anatase, they additionally observed increased expression of exposed {010} facets which have a higher surface energy and show greater photocatalytic activity than the more stable {101} facets that typically form under equilibrium conditions. Lastly, they could observe rutile-anatase heterojunctions which are, as explained in section 2.4.5, crucial to harness the synergistic effects of having a combination of both semiconductors in the surface. Similar observations regarding the formation of anatase and rutile were made by Robert et al. [77] for laser irradiated anatase powder. These experiments indicate that fast cooling rates and small particle sizes favour the formation of anatase while extended exposure to heat as well as bigger particle sizes favour rutile formation.

These observations are also made with non-laser processes. For example by Yang et al. [78] who performed flame spraying experiments where deposited particles showed a correlation between particle size and phase meaning the smaller particles consisted of anatase while the bigger ones were rutile. Additionally, upon exposure to heat, either by a post-treatment or during the coating process as a result of the extended exposure to the flame, the anatase gradually transformed into rutile.

A transformation in the opposite direction i.e., from rutile to anatase was observed by Ma et al. [79,80] after the irradiation of a rutile singe crystal with near-infrared radiation from a titanium-sapphire laser source with a pulse length of 150 fs. While this result was attributed to the mechanical stresses (especially compressive stresses) induced in the surface, it appears more likely that a partial melting and rapid re-solidification were the cause for their observation. This is because as mentioned in section 2.4.5, compressive stresses tend to favour the formation of rutile as a result of anatase's higher molar volume. The rapid re-solidification after melting can however favour the formation of anatase. [75]

Krenek et al. [81] used a laser with pulse duration of 200 ns to produce rectangular wells with an edge length of 500 μm and a depth of 300 μm. XRD experiments showed the prevalence of both titanium and oxygen-deficient titanium oxides (TiO, Ti<sub>2</sub>O, Ti<sub>2</sub>O<sub>3</sub>) with only small amounts (ca. 5%) of TiO<sub>2</sub> in both, the anatase and the rutile forms. However, the very smooth, round shape of the created particles indicates that the high cooling speeds after irradiation favoured the formation of amorphous oxides. Additionally, it was found that the titanium removed by the laser redeposited at the sites that were not irradiated, and that oxidation occurred during this material transport. Similar observations were made by Zwahr et al. [82] for picosecond DLIP patterns on titanium that showed an accumulation of oxides at the structure maxima. However, as the oxides were only

analysed by EDS, no statements about their phase could be made.

In 2021, Toma et al. [83] used a DLIP setup to improve the photocatalytic performance of suspension-sprayed nanoparticle coatings. For this, several photocatalytic coatings with varying compositions of rutile and anatase were produced. In a second processing step, a 1053 nm laser setup with a pulse length of 15 ns was used to produce cross patterns on these surfaces. It was observed that lower pulse numbers resulted in only minor melt formation and the predominant formation of anatase, while higher pulse numbers caused more melt formation and an increase in rutile. It was shown that the surfaces treated with more pulses exhibited higher photocatalytic activity which correlates with a more efficient light-trapping ability that results in increased light absorption. This increase in light absorption was observed by UV-Vis spectroscopy but could also be seen with the naked eye as the samples successively got darker with increased laser exposure.

### 2.8 Summary

Current methods to produce photocatalytic surfaces come with several disadvantages as they mostly rely on nanoparticles or wet chemical processes that require potentially harmful chemicals. Additional problems arise when considering the large-scale industrial application of these processes as they are often limited by reactor sizes, part geometries, or issues related to the loss of nanoparticles over time and the resulting loss of functionality, not to mention regulatory and safety concerns.

For these reasons, this work investigates an alternative approach in which the required oxides are produced in situ as the process oxides of a DLIP process that simultaneously increases the active surface by creating a suitable micropattern. To determine if this approach is viable, the following questions need to be answered:

- Can DLIP produce a sufficient amount of active, surface-bound oxide?
- Is DLIP required for this, or can a conventional laser process achieve the same?
- Can the process parameters be adapted to favour the formation of more photocatalytically active oxides or a mix of oxides that is especially active?
- How else can the resulting oxides be manipulated to achieve maximum activity?

### 3 Objectives

To answer the questions formulated in the previous section, a number of key objectives were defined:

### **Objective 1: Precise calculation of laser parameters**

The oxidation process and the formation of different oxidic phases likely strongly depend on the applied laser and scanning parameters. As a result, the resulting surface topography cannot be used as an indication to evaluate surfaces. For example, two surfaces with identical surface parameters, such as pattern periodicity, depth and roughness could differ vastly in their activity depending on the specific laser parameters used to produce those structures and the resulting oxide compositions. For this reason, a robust methodology for the determination of rather elusive but crucial patterning parameters had to be developed. These parameters, like the accumulated fluence on the sample surface or the total number of pulses a given point of the surface was exposed to, are generally already calculated and reported in literature, however, as they are instrumental for this work, established approaches need to be revisited and reevaluated.

### Objective 2: Methodology development and initial tests

To evaluate if it is possible to use direct laser interference patterning to produce photocatalytic surfaces, first tests on a small range of parameter combinations need to be performed. Most importantly, a reliable method to measure and quantify the photocatalytic activity must be established.

### Objective 3: Expanded parameter screening and surface analysis to understand the oxide formation and its effect on the activity

With a proof of concept established, the utilised laser parameters need to be expanded to cover a wider range and to include different pattern types to find an optimal combination of parameters. Additionally, the resulting surfaces must be analysed and evaluated to develop an understanding of the oxidation process and the occurring material transport. The developed theories are necessary to understand and then better utilise the approach.

### Objective 4: Further improving the activity using the insights gained in the previous steps

Based on the results of objective 3, additional beneficial adaptations to the laser process or suitable pre- and post-treatments for the samples should be identified and tested to both verify the previously defined theories and predictions about the process and to further increase the reactivity of the surfaces.

### Objective 5: Creation of a scaled-up prototype using off-the-shelf materials

Finally, the practicality of the investigated approach should be verified. To do so the setup should be scaled up to a simple reactor. While the insights gathered in the previous steps are crucial to design this reactor, the materials in this setup should be cheap and easily available. This way, it can be tested if the results obtained on expensive, highly pure, and mirror-polished samples can be transferred to industrial materials, which is crucial for later applications.

### 4 Methods

### 4.1 Sample Preparation

To avoid disturbances from other elements a titanium sheet of 99.995 wt.% purity was acquired from HMW Hanauer GmbH and cut using electric discharge machining to achieve 1 mm thick pieces with a size of 5 x 5 mm. The samples were then heat-treated in a vacuum ( $\approx 10^{-5}$  mbar) at 700°C (well below the  $\alpha$ - $\beta$  transition) with a holding time of ten minutes and heating/cooling rates of 1°C/min to remove potential surface contamination and to mitigate potential thermal effects of the electric arc at the sample edges.

To ensure that the laser interacts with a flat and clean surface, the samples were mirror-polished to a deformation-free finish ( $S_a < 0.2 \mu m$ ). The following routine was developed for this purpose:

- 1. Grinding with SiC grinding paper: #600 for 200 seconds and #1200 for 600 seconds
- 2. OPS polishing: 8 min polishing with oxide particle suspension (OPS) from Struers mixed with 2% H<sub>2</sub>O<sub>2</sub> (30% w/v) and 2% NH<sub>3</sub> (25% v/v)
- 3. Etching: 45 seconds in Beraha 1 stock solution (500 ml distilled water; 100 ml HCl (32%); 12 g ammonium bifluoride) to remove existing deformation layers
- 4. OPS polishing identical to step 2

After the polishing, the samples were cleaned in an ultrasonic bath with ethanol. All grinding and polishing steps were performed with an automated Struers TegraPol grinding and polishing machine.

### **4.2** Direct Laser Interference Patterning (DLIP)

As described in section 2.6.7 direct laser interference patterning uses several laser beams that are overlapped on the material surface, generating an interference pattern that is transferred to the material surface through melt movements, evaporation, or direct ablation. In this work, lasers with pulses in the femtosecond and the picosecond regimes were used to pattern the surfaces. The initial laser experiments, published in the first paper, were performed using a Spitfire Ti:sapphire laser with a centre wavelength of 800 nm and a pulse duration of 100 fs. During the experiments regarding fluence accumulation and spot overlap, it became clear that the pulse lengths in the femtosecond regime did not produce sufficient amounts of oxide during the processing for it to be a viable tool for producing photocatalytic surfaces. For this reason, the subsequent experiments were performed using an EdgeWave px Nd:YAG laser with a pulse length of 12 ps and a maximum output power of 10 W at a wavelength of 532 nm. To split the initial beams delivered by the laser systems, both setups employed diffractive optical elements. The resulting sub-beams are then focused on the material surface using lenses and, in the case of the picosecond laser, a prism. Further details regarding the beam paths and setups can be found in the respective publications.

### 4.3 Confocal Laser Scanning Microscopy

Topographical analysis was performed with an OLS 4100 confocal laser scanning microscope from Olympus. This contactless measurement can map the three-dimensional surface of the samples with a maximal lateral resolution of 0.12  $\mu$ m and a height resolution of 10 nm. The pattern depth was extracted from line profiles by evaluating (Rc) which represents the average height of the features in a periodic pattern. [84,85]

### 4.4 Scanning Electron Microscopy (SEM), Focused Ion Beam (FIB) and Energy dispersive X-ray spectroscopy (EDS)

Two SEM/FIB dual-beam workstations (Thermo Fisher Helios G4 PFIB CXe and FEI Helios Nanolab600) were used to image the surfaces produced in this work. This was generally done using secondary electrons measured with the ICE detector of the PFIB instrument. Besides imaging the patterned surfaces, focused ion beams (xenon and gallium ions, respectively) were used to create cross-sections of the patterns. This allowed the surface topography to be investigated in more detail and the depth of the patterns to be determined. This was especially helpful, as the depth of the deeper patterns could not be determined accurately using the confocal laser scanning microscope. Additionally, cross-sections were used to gather information about the oxide distribution. This was initially done using the primary electron and secondary ion contrasts. More detailed chemical information was then obtained via EDS using the EDAX Octane Elite Super EDS detector of the PFIB. The data obtained from this measurement was analysed with the APEX v2 measurement and analysis software. Both the SEM imaging and the EDS analyses were performed with an acceleration voltage of 5 kV.

### 4.5 X-Ray Diffraction (XRD)

A PANalytical X'Pert Pro MPD diffractometer with copper  $K\alpha$  radiation was used for the diffraction experiments. As the relevant oxides were only present in the surface, a Goebel mirror was used to perform the measurements in grazing incidence mode with an incidence angle of  $0.8^{\circ}$ . To minimize shadowing effects caused by the surface structures, the pattern was oriented parallel to the incident beam. Most measurements were performed in a 2Theta range of  $20\text{-}75^{\circ}$  with a step size of  $0.05^{\circ}$ . The dwell time was adjusted according to the sample geometry and pattern type to achieve acceptable signal-to-noise ratios.

### 4.6 Methylene Blue Degradation and UV-Vis Spectroscopy

The photocatalytic activities of the produced samples were determined by measuring the degradation rate of methylene blue in a 50  $\mu$ M aqueous solution under UV-A light. For each sample condition, three samples were placed randomly in an array, and each was exposed to 125  $\mu$ L MB-solution. This sample holder was then placed in a mirrored reaction chamber ("Nailstar" model NS-01-UK&EU) equipped with four 8 W fluorescent lamps emitting a centre wavelength of 365 nm. After an initial waiting period to allow for adsorption, the samples were exposed to the UV-A radiation for a total of two hours. Evaporation was minimized by covering the sample holder with a UV-transparent piece of PMMA. Combined with the minimal UV adsorption of the methylene blue solution this setup ensured that the incident light could reach the sample surface.

After the experiment 90 µL of solution were retrieved to determine the remaining concentration via UV-Vis spectroscopy.

The experimental details for the prototype can be found in the respective publication. Here, it should only be noted that the sample volume extracted at various times during the experiment was the same as in the previous experiments (90  $\mu$ L). This was done to keep the determination of the concentration by UV-Vis analysis consistent.

For the UV-Vis measurements, the sample was diluted with 160  $\mu$ L distilled water to achieve a total sample volume of 250  $\mu$ L. The sample cuvette with an optical path of 10 mm (UV-Cuvette micro, Band GmbH, Wertheim, Germany, or PerkinElmer Spectroscopy cell B0631070) was then placed in the beam path of a Lambda 750 spectrometer (Perkin Elmer Inc., Shelton, USA). The device analyses the absorbance of the sample at various wavelengths by detecting the transmitted light energy. To isolate

the absorption of MB, an identical cuvette filled with distilled water was placed in the reference beam path and subtracted from the measurement.

The MB molecule has an absorption maximum at 664 nm. As the absorbance of a solution depends strongly on its concentration, UV-Vis spectroscopy can be used to efficiently determine the remaining concentrations after the degradation experiments. However, as there is not necessarily a linear dependency between concentration and absorption, a calibration curve was measured by determining the absorption values of solutions with known concentrations at 664 nm. Using this calibration curve, the concentrations of the sample solutions were then determined by evaluating their absorbance at 664 nm. The measurements were performed in a wavelength range from 600 nm to 700 nm with one measurement taken every 4 nm and an integration time of 0.2 seconds.

### 5 Results

In the following sections, the objectives stated in section 3 are addressed, and for each one, the results achieved within the scope of this thesis are briefly summarised, and the associated papers are referenced. Figure 9 presents an overview of the papers included in this thesis and their respective contents.

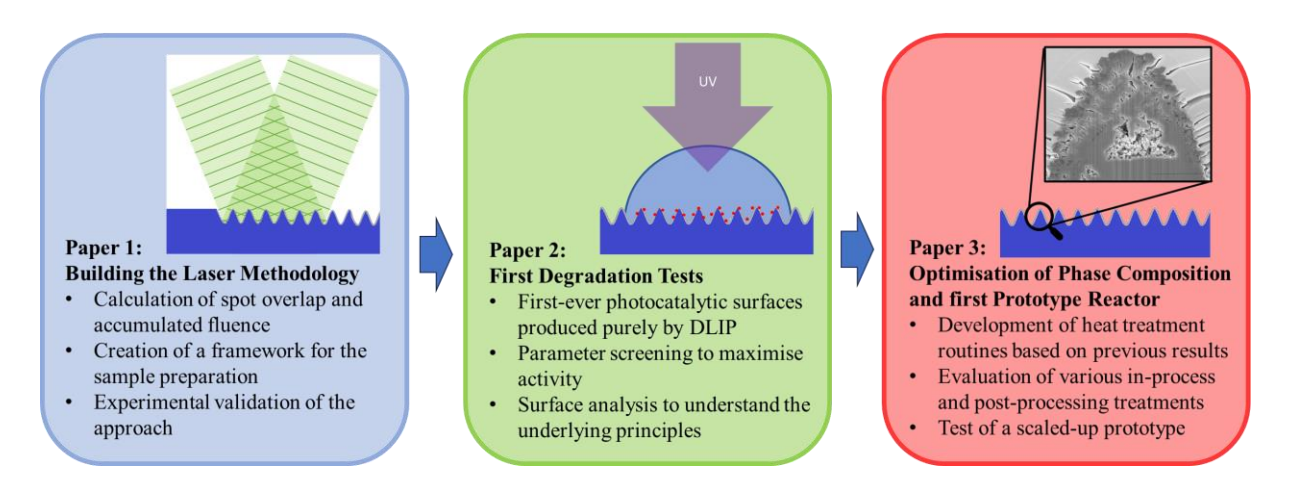


Figure 9: Schematic of the results presented in this thesis

### **Objective 1: Precise calculation of laser parameters (Publication 1)**

When it comes to structure development and especially to the formation of various oxides, it is expected that the total laser energy a surface has been exposed to, as well as the number of pulses by which this energy has been delivered are crucial parameters. Therefore, commonly used approaches for the calculation of pulse overlap, accumulated fluence, and other laser parameters were surveyed and compared. It was found that state-of-the-art approaches to calculate the accumulated fluence on the surface come with an error of over 20%. For this reason, an alternative approach for calculating these parameters was developed and tested. It was shown that, with this approach, the input parameters for a patterning process that achieves a desired accumulated fluence, pulse fluence, and number of pulses per point can be calculated using a simple spreadsheet. Additionally, it was shown that this accurate assessment of the processing parameters can be used to determine the effect different input parameters have on the resulting pattern periodicity.

### Objective 2: Methodology development and initial tests (Publication 2)

A methodology to test the photocatalytic activity of samples was developed based on methylene blue (MB) degradation under UV-A irradiation. For this purpose, several light sources were tested until a commercially available nail polish hardener was chosen for the experiments, as it provided a homogenous irradiation with 365 nm UV radiation within a mirrored enclosure. After the experiment, the remaining MB concentration was determined using UV-Vis spectroscopy. With this methodology in place, a series of experiments was performed, and it was shown that the single-step production of photocatalytic surfaces is not only possible using DLIP technology, but also that the surfaces processed with DLIP perform far better than those only processed with one beam.

### Objective 3: Expanded parameter screening and surface analysis to understand the oxide formation and its effect on the activity (Publications 2 and 3)

As planned, the range of parameters was expanded upon. Various accumulated fluences, pulse numbers, pattern periodicities, and pattern types were tested. The resulting surfaces were then analysed with regard to their topography and chemistry. The results showed that especially large numbers of pulses, each with a relatively low fluence were ideal to create surfaces with high photocatalytic activities. The chemical analysis revealed that various oxides are present in the surfaces. Apart from the two dominant TiO<sub>2</sub> phases, anatase and rutile the oxygen-deficient titanium oxides TiO, and Ti<sub>2</sub>O<sub>3</sub> were also produced in significant amounts. It was found that the more active surfaces show lower TiO contents. Finally, a theory was developed to explain the observed oxide formation and its dependency on the laser parameters.

### Objective 4: Further improving the activity using the insights gained in the previous steps (Publication 3)

To further improve the photocatalytic activity of the most promising surfaces and to form a better understanding of the oxide formation mechanism, multiple heat treatments were performed. Those treatments were applied both during the patterning process and afterwards in an additional post-treatment. The impact of these treatments was largely beneficial for the photocatalytic activity although some sintering that led to a reduction of surface area could be observed. The effect of the heat treatments on the existing phases was investigated and together with the results from objective 3, a comprehensive model of the oxide formation mechanism was developed.

### Objective 5: Creation of a scaled-up prototype using off-the-shelf materials (Publication 3)

A scaled-up prototype reactor was built in which, instead of the previous 125  $\mu$ L of methylene blue solution, 1.5 litres of solution were continuously pumped over a laser-treated titanium foil. The resulting degradation rate was comparable to that of the laboratory setup, although the titanium foil was neither highly pure nor surface-treated in any way prior to the laser treatment, except for a minor cleaning with isopropanol. This result indicates that the approach can be scaled up to larger reactors employing artificial or solar light to remove contaminants from aqueous solutions.

### Development and validation of a calculation routine for the precise determination of pulse overlap and accumulated fluence in pulsed laser surface treatment

Tobias Fox<sup>1</sup>, Frank Mücklich<sup>1</sup>

Chair of Functional Materials, Department of Materials Science, Saarland University, 66123, Saarbrücken, Germany.

Published "Advanced Engineering Materials" 2022 (CiteScore 5.7 by 2023) https://doi.org/10.1002/adem.202201021

#### Abstract:

In laser material processing, a variety of parameters like pulse fluence, total dose, step size, and pulse-to-pulse overlap are used to define and compare laser processes. Of these parameters, the pulse-to-pulse overlap can be the hardest to access as it is not implemented directly but instead depends on the spot diameter, its shape, and the respective scanning path that is used to cover the surface. This article shows that existing calculation routes overestimate the actual overlap by up to 21%. A novel calculation route is developed that greatly facilitates the determination of the pulse overlap and thereby the average number of laser pulses that interact with a given point on the surface. This approach makes it possible to achieve more reliable and comparable laser processes, which in return leads to better control of the procedure as the effect of individual parameters on a given output can be determined with greater precision.

### **Author Contribution**

Conceptualization: Lead; Formal analysis: Lead; Investigation: Lead; Methodology: Lead; Validation: Lead; Writing - original draft: Lead; Writing - review & editing: Lead

www.aem-journal.com

# Development and Validation of a Calculation Routine for the Precise Determination of Pulse Overlap and Accumulated Fluence in Pulsed Laser Surface Treatment

Tobias Fox\* and Frank Mücklich

In laser material processing, a variety of parameters like pulse fluence, total dose, step size, and pulse-to-pulse overlap are used to define and compare laser processes. Of these parameters, the pulse-to-pulse overlap can be the hardest to access as it is not implemented directly but instead depends on the spot diameter, its shape, and the respective scanning path that is used to cover the surface. This article shows that existing calculation routes overestimate the actual overlap by up to 21%. A novel calculation route is developed that greatly facilitates the determination of the pulse overlap and thereby the average number of laser pulses that interact with a given point on the surface. This approach makes it possible to achieve more reliable and comparable laser processes, which in return leads to better control of the procedure as the effect of individual parameters on a given output can be determined with greater precision.

#### 1. Introduction

The overlapping of circular laser spots plays a crucial role in laser surface functionalization where homogeneous surface coverage is required. (1-6) Other techniques like cutting, welding, and 3D manufacturing using pulsed lasers also require the scanning of surfaces and consequently, the overlap of multiple laser spots. This is generally achieved by overlapping multiple uniaxial scan lines consisting of individual spots with a defined line-to-line distance, the so-called hatching distance, until the desired surface is covered. The total pulse-to-pulse overlap resulting from the overlaps in both scan directions marks one of the most important parameters in laser processing as it describes the average number of pulses that interact with a given point on the surface. Together with the pulse fluence, the total overlap is generally altered systematically to perform parameter

T. Fox, F. Mücklich Chair of Functional Materials Saarland University Campus D3.3, Saarbrücken 66123, Germany E-mail: tobias.fox@uni-saarland.de

The ORCID identification number(s) for the author(s) of this article can be found under https://doi.org/10.1002/adem.202201021.

© 2022 The Authors. Advanced Engineering Materials published by Wiley-VCH GmbH. This is an open access article under the terms of the Creative Commons Attribution-NonCommercial License, which permits use, distribution and reproduction in any medium, provided the original work is properly cited and is not used for commercial purposes.

DOI: 10.1002/adem.202201021

screenings to characterize and optimize processes. Consequently, it is crucial that the overlap is calculated and reported correctly to ensure flawless experiments and comparability. However, as the pulse overlap depends strongly on the spot shape and the employed scanning routine, its calculation can be challenging.<sup>[7–15]</sup>

The impact of the applied scanning routine on the quality of a resulting surface is especially evident in the case of direct laser interference patterning (DLIP). This is because this technique produces an interference-based periodic pattern within the individual scan lines. [16] If the hatching distance ( $\Delta \gamma$ ) between these scan lines is too large the surface modulation caused by the Gaussian profile of the

laser beam can cause a superimposed periodicity as shown in Figure 1.

To avoid periodic surface modulation, the hatching distance is usually reduced until the outer regions of each scan line overlap sufficiently to form a homogeneous surface. The pulse-to-pulse overlap (OL) thereby defines the number of pulses  $n_x$  interacting with a given point in the surface and is generally calculated using Equation (1), where  $\Delta x$  refers to the step size within the scan line according to Figure 1 and D refers to the respective spot diameter.

$$OL = \left(1 - \frac{\Delta x}{D}\right) \times 100 = (1 - 1/n_x) \times 100$$
 (1)

However, as this equation only considers the overlap within a single scan line (given by  $\Delta x$ ) and not the overlap of separate lines (given by  $\Delta y$ ) there is an intrinsic error that leads to an underestimation of the overlap. This effect is relatively small if the overlap in the x-direction is significantly greater than the one in the y-direction, but it becomes significant if the overlap between lines is increased. [1,4,17]

Additionally, if the overlap in the y-direction is increased the overlap in the x-direction must be decreased respectively to keep the overlal overlap constant. This, however, leads to the second cause of the error as Equation (1) can only be used for rectangular spots or as an approximation for circular spots with step sizes that are relatively small compared to the spot radius r. For bigger step sizes the overlap of two circular spots is instead described more accurately by Equation (2). [18,19] While Equation (2) can be used to calculate the overlap within one scan line for a given step size  $\Delta x$ , it also does not consider the overlap of different

2201021 (1 of 7)

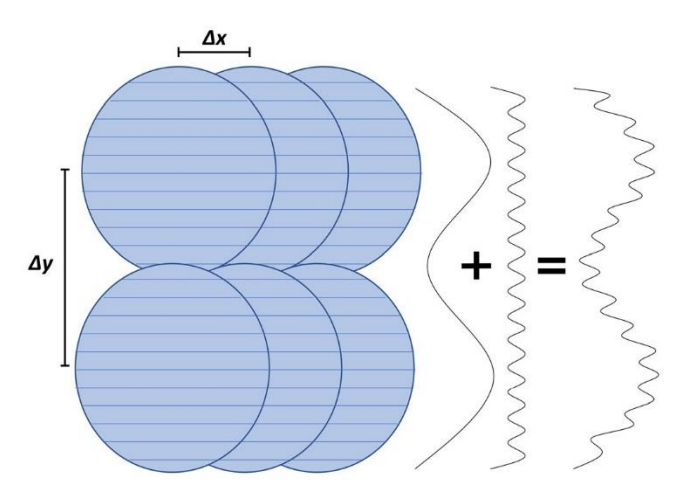


**Figure 1.** Schematic surface scan in which the hatching distance  $\Delta y$  is too large resulting in a periodical surface modulation in addition to the desired interference pattern.

scan lines and most importantly, cannot be solved for  $\Delta x$ . Therefore, Equation (2) cannot be used to calculate the step sizes that are required to achieve the desired overlap. Especially, if the  $\gamma$ -direction is considered as well approximating Equation (2) and solving the approximation for  $\Delta x$  is unfeasible.

$$OL = \frac{2 \times r^2 \times \cos^{-1}\left(\frac{\Delta x}{2r}\right) - \frac{\Delta x}{2} \times \sqrt{4 \times r^2 - \Delta x^2}}{\pi \times r^2} \times 100$$
 (2)

The following section describes a calculation route that aims to avoid the described errors and makes it possible to calculate the spot overlap for a wide variety of spot profiles. This further makes it possible to calculate the spot overlap and accumulated fluence on a processed area even if the hatching distance is reduced. This generally leads to a more even surface coverage and a more homogenous intensity distribution. The approach is then verified in two experiments for which titanium was chosen as reference material. Titanium was chosen because it is widely used in applications that require precise surface treatments like aerospace and biomedicine and because of its use in additive manufacturing that also requires defined scanning routines.[20-23] For those reasons, a significant amount of research on laser processing of this material has already been conducted and reported. Comparing these results can, however, oftentimes be challenging as many publications miss crucial details, like the used spot diameter, when describing the experimental setup or do not clearly describe how a stated overlap was calculated. If the overlap is calculated, it is generally done using Equation (1) which comes with the aforementioned intrinsic errors as it assumes rectangular spots and does not consider the overlap between scan lines. [24-32] With that in mind, this work proposes a relatively simple and straightforward calculation route that could, when implemented widely, greatly improve the comparability and reproducibility of experiments across various fields of research and facilitate the transfer to industry.

#### 2. Results and Discussion

The following section presents a detailed derivation that leads to a set of equations that can be used to determine crucial process parameters such as pulse overlap, accumulated fluence, or the required step sizes needed to achieve the desired number of laser pulses per point in the surface. The model is then validated using ultra short pulsed DLIP on titanium surfaces.

#### 2.1. Formalism Development

To start the calculation a rectangular reference surface  $A_{\rm ref}$  with

$$A_{\rm ref} = x_{\rm ref} \times y_{\rm ref} \tag{3}$$

can be assumed. With given pulse distances  $\Delta x$  and  $\Delta y$  the total number of pulses  $n_{\text{ref}}$  applied to this reference area is defined by Equation (4).

$$n_{\rm ref} = \frac{x_{\rm ref}}{\Delta x} \times \frac{y_{\rm ref}}{\Delta y}$$
 (4)

The accumulated fluence  $F_{\rm acc}$  on the reference surface is then given by the single pulse energy  $E_{\rm Pulse}$ , the number of pulses and the reference area according to Equation (5).

$$F_{\rm acc} = \frac{E_{\rm Pulse} \times n_{\rm ref}}{A_{\rm ref}} \tag{5}$$

Equation (5) can then be combined with Equation (4) to eliminate the reference values and achieve Equation (6).

$$F_{\rm acc} = \frac{E_{\rm Pulse}}{\Delta x \times \Delta y} \tag{6}$$

It is important to note that Equation (6) does not rely on the spot area or shape and can therefore be used without requiring the complex calculation of overlap areas as in Equation (2).

The total number of pulses  $n_{\rm acc}$  by which the accumulated fluence is applied on a given point of the surface can be calculated with Equation (7) and is then used to calculate the averaged pulse overlap (OL) via Equation (8).

$$n_{\rm acc} = \frac{F_{\rm acc}}{F_{\rm Pulse}} = \frac{F_{\rm acc} \times A_{\rm Spot}}{E_{\rm Pulse}} \tag{7}$$

$$OL(\%) = (1 - 1/n_{acc}) \times 100$$
 (8)

In contrast to Equation (2), this set of equations can easily be solved for  $\Delta x$  meaning that the necessary pulse distance required to achieve the desired overlap can be calculated. This greatly facilitates parameter screenings that aim to systematically vary the pulse overlap.

An example of the calculation of process parameters using these equations is given in the experimental section. As can be seen from Equation (7), the area of a single laser spot  $A_{\rm Spot}$  is required for the last calculation step. While for Gaussian beam profiles, this value can be easily determined mathematically, in the case of more complex beam profiles it is recommended to first observe the effective spot diameter with the desired pulse fluence on the surface. Apart from the spot area, the transversal

2201021 (2 of 7)

www.advancedsciencenews.com

www.aem-journal.com

ADVANCED ENGINEERING MATERIALS

beam profile is not considered any further as the objective of the scanning routine is to achieve homogenous surface coverage and thereby even out the intensity distribution. Therefore, only the average values are considered.

#### 2.2. Experimental Validation

The approach derived in Section 2.1 was validated in two separate experiments. This was done using the USP-DLIP setup described in Ref. [2] employing a titanium–sapphire femtosecond laser with a pulse duration of 100 fs and a repetition rate of 1 kHz. This setup ensures that heat accumulation within a scan line and between different scan lines is neglectable as it can be assumed that the material reaches equilibrium before the next pulse arrives. The periodicity of the applied interference pattern was fixed to 3  $\mu m$ . Further details on the patterning method and the setup used are given in the experimental section.

### 2.2.1. Validation of a Model Surface

To cover a surface with a defined average number of pulses per point ( $n_{acc}$ ), the required step sizes in the x- and y-directions need to be calculated, respectively. The following section illustrates the shortcomings of state-of-the-art approaches to do so and investigates the newly developed model.

A scan with an average surface coverage of one pulse per point on the surface was performed. In case of spherical spots, where a surface coverage without gaps is not possible, this task requires some spot overlap. This way, if the surface area without any laser interaction is equal to the area with two interactions, each point on the surface experiences an average of one interaction. The average pulse number of one pulse per point was chosen due to the simplicity of evaluation of the resulting surfaces (Figure 2) and because this example shows that the widely established approach of employing Equation (1) to calculate the fluence fails to consider the free spaces between non-rectangular spots. Instead, if Equation (1) is applied to the same problem, the result would be a step size equal to the beam diameter resulting in a surface with no overlap but significant unirradiated areas.

In contrast to Equation (1), Equation (2) considers the circular shape of the spot. However, it cannot be solved for  $\Delta x$  and the necessity to consider the second scan direction and the respective overlap in  $\Delta y$  makes numeric solutions unfeasible. Additionally, deviations from the circular shape would easily result in errors while the newly developed method only requires the spot area regardless of shape.

To verify that the proposed calculation route can determine the step sizes in the x- and y-directions, the surface depicted in Figure 2a was produced. The spot diameter was 79  $\mu$ m resulting in step sizes in the x- and y-directions of 70  $\mu$ m. While the step sizes in the x- and y-directions do not need to be equal, the calculation was adapted to meet this condition. The detailed calculation is given in the experimental section.

The produced surface is depicted in Figure 2a and appears to be close to the ideal arrangement of spots in Figure 2d. To determine the surface fractions that interacted with 0, 1, or 2 pulses

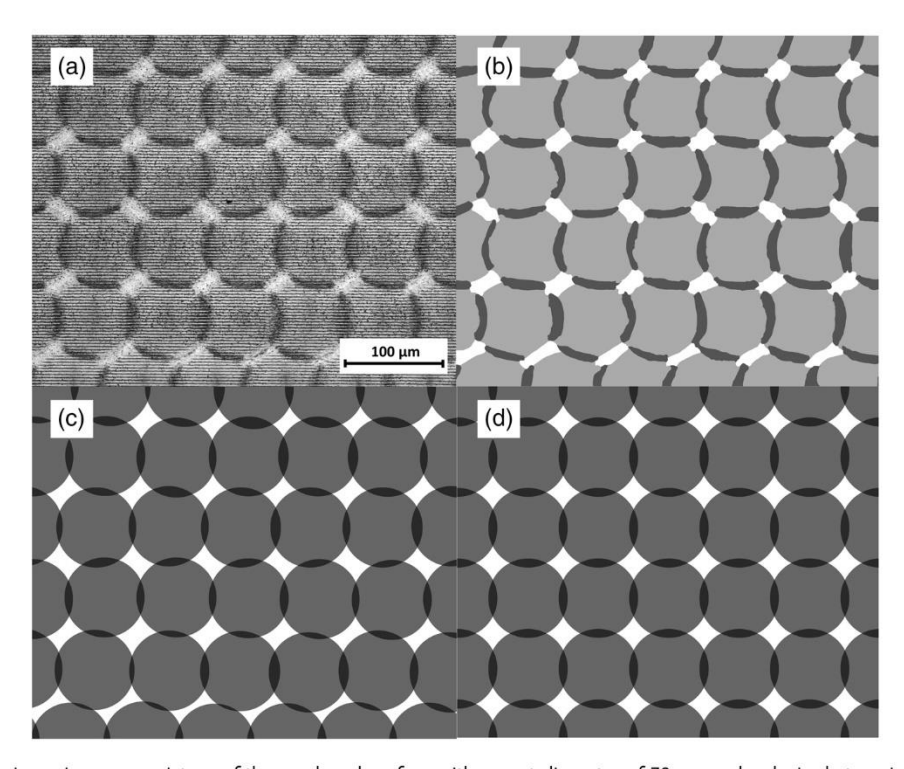


Figure 2. a) Laser scanning microscope picture of the produced surface with a spot diameter of 79 μm and a desired step size of 70 μm in the *x*- and *y*-directions. b) Segmentation of image a) to determine the surface fractions that experienced one (light gray), two (dark gray) or zero (white) laser interactions. c) Approximating a) with circles to determine the idealized surface area fractions. d) Ideal grid for step sizes of 70 μm.

2201021 (3 of 7)

ENGINEERING

the image was segmented manually as shown in Figure 2b. Additionally, circles were fitted to the spots in (a) to determine idealized surface fractions for the real surface.

The images (b) to (d) were analyzed via image analysis to obtain the regions of the surface that interacted with 0, 1, or 2 pulses. This was done by employing a grayscale threshold, where the bright areas represent 0 interactions, the gray areas 1 interaction, and the dark areas 2 interactions. The results are given in **Table 1**.

It becomes evident that the results for the ideal grid meet the expectation that the area affected by two pulses is equal to that affected by 0 pulses, resulting in an average of one interaction per point on the surface as was the premise of the calculation. The results for the idealized surface are close to this result. However, the inaccuracy of the sample stage led to a distortion of the theoretical grid and thereby to a deviation from the theoretical values.

Interestingly, the real surface shows a strong increase in the area subjected to two pulses that cannot be explained by the given model. To explain this result, it must be considered that the patterned regions show a lower ablation threshold than the polished surface as a result of an increased surface roughness, oxidation, and damage accumulation. [2,33,34] This results in an increase in the effective spot diameter in the overlap areas as shown in **Figure 3**, as the outer regions of the beam profile that did not

**Table 1.** Surface coverage of the real surface (Figure 2b), its idealized approximation (c), and of the ideal grid (d).

	0 Pulses	1 Pulse	2 Pulses
Real Surface	7.93%	75.96%	16.11%
Idealized Surface	8.96%	83.02%	8.02%
Ideal Grid	9.20%	81.60%	9.20%

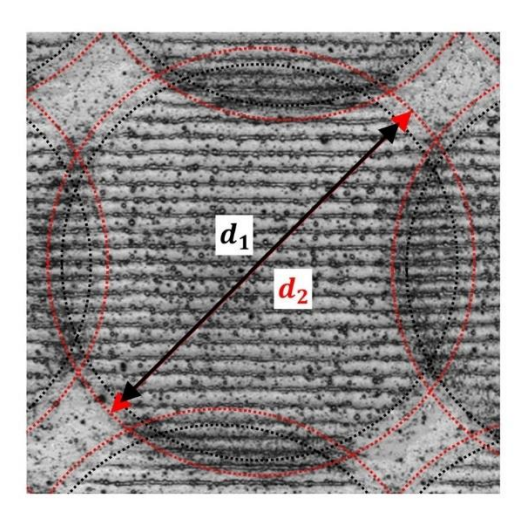


**Figure 3.** Detailed view of one of the spots from Figure 2a. The black circles indicate the spot diameter on the polished surface  $(d_1 = 79 \, \mu m)$  that was used for the calculations. The red circles indicate the increased effective spot diameter  $(d_2 = 85.2 \, \mu m)$  within the patterned regions. This increase in effective spot diameter causes an additional two-pulse overlap (dark regions between red circles) that is not accounted for in the model.

cause ablation on the polished areas can interact significantly with the already patterned areas. This leads to additional two-pulse areas. While the model only expects the overlap between the black circles showing the formerly measured spot diameter of 79  $\mu m$ , the apparent spot diameter on the patterned surfaces increases to around 85.2  $\mu m$ , and additional two-pulse areas between the red circles are produced. When calculating the expected overlap of circles with a diameter of 85.2  $\mu m$  using Equation (2) and the used step size of 70  $\mu m$  the resulting 17.6% are relatively close to the measured two-pulse area in the real surface (16.11%). This demonstrates that a correct assessment of the effective spot area is crucial to calculate relevant process parameters.  $^{[33-36]}$ 

To assess how strongly this additional absorption influences the obtained results, multiple surfaces were produced and systematically analyzed in the next section.

#### 2.2.2. Validation of the Model for Fully Patterned Surfaces

To evaluate the processing parameters on fully patterned surfaces, an exemplary study was carried out, observing the pattern depth of a DLIP line pattern with 3  $\mu$ m periodicity and its dependence upon the pulse fluence  $F_{\rm Pulse}$ , the number of pulses per point  $n_{\rm acc}$ , and the step size in  $\gamma$  direction  $\Delta\gamma$ . The evaluated factors and the results including the standard deviation of the nine measurements taken per parameter combination are given in **Table 2**. It is expected that  $\Delta\gamma$  has no effect on the pattern depth, as the step size in the  $\gamma$ -direction is balanced with a respectively calculated step size in the x-direction to keep  $n_{\rm acc}$  on the desired level. Two exemplary surfaces are shown in **Figure 4**.

The data from Table 2 was evaluated using the software "Minitab 19" (Minitab GmbH) to produce the Pareto chart shown in Figure 4. This chart shows to what extent the different input parameters influence the output parameter, i.e., the pattern depth. As expected, the pulse fluence and the number of pulses per point have the strongest influence on the resulting pattern depth. Their interaction also shows a strong effect meaning that the two parameters do not influence the result independently but show a strong synergy. The step size in the  $\gamma$ -direction and its interactions with the other parameters shows only a minor effect

**Table 2.** Experimental design to investigate the three parameters  $F_{\text{Pulse}}$ ,  $n_{\text{acc}}$ , and  $\Delta y$  with two levels each.  $\Delta x$  was determined using the model above. The spot diameter was 70  $\mu$ m.  $\sigma$  refers to the standard deviation of the measured pattern depths.

$F_{\rm Pulse}[{ m J cm}^{-2}]$	n <sub>acc</sub> -	$\Delta y \ [\mu m]$	$\Delta x [\mu m]$	Pattern Depth [µm]	$\sigma$ [ $\mu$ m]
0.5	10	6	64	451.56	27.46
0.5	10	24	16	479.89	30.29
0.5	20	6	32	800.56	21.43
0.5	20	24	8	801.67	55.91
1	10	6	64	884.44	77.38
1	10	24	16	1070.44	50.42
1	20	6	32	1804.56	141.82
1	20	24	8	1849.56	97.71

2201021 (4 of 7)

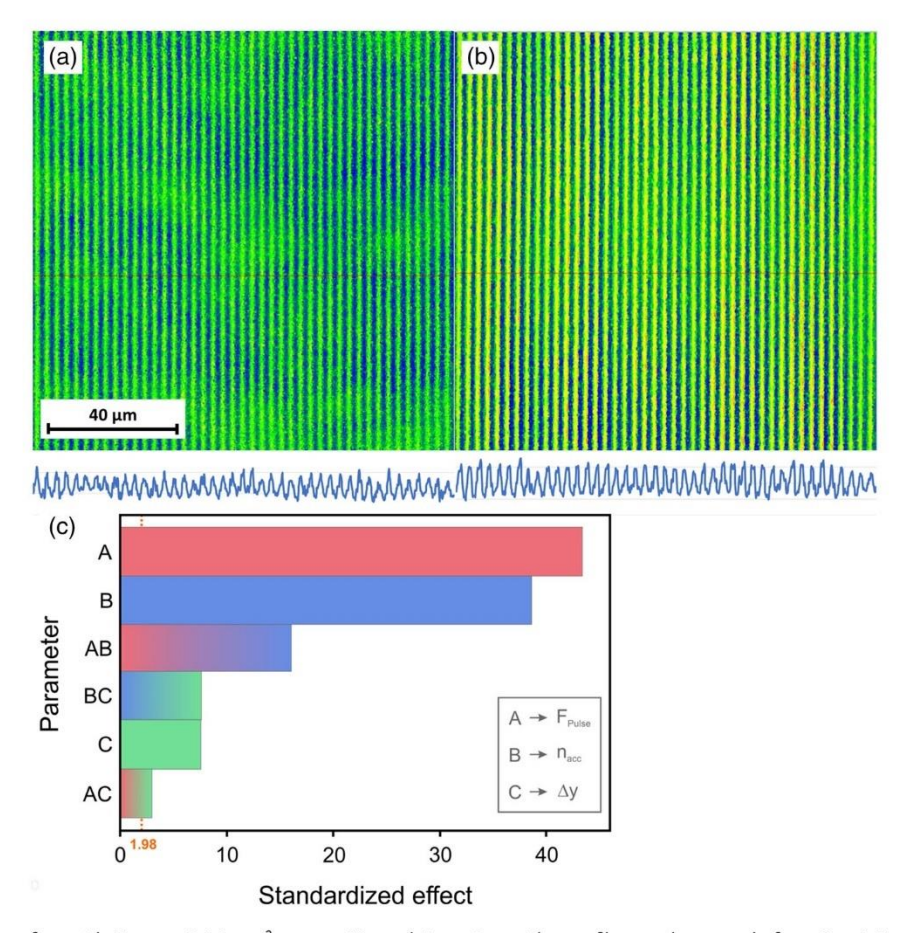


Figure 4. a) Exemplary surface with  $F_{Pulse}=0.5$  J cm $^{-2}$ ,  $n_{acc}=10$ , and  $\Delta\gamma=6\,\mu m$ . The profile scan has a scale from 0 to 1.5  $\mu m$ . b) Exemplary surface with  $F_{\text{Pulse}} = 1 \, \text{J cm}^{-2}$ ,  $n_{\text{acc}} = 20$  and  $\Delta y = 24 \, \mu\text{m}$ . The profile scan has a scale from 0 to 4  $\mu$ m. c) The Pareto chart for the given data set shows that the pulse fluence and the number of pulses have a strong effect on the resulting pattern depth. The interaction between those two factors also influences the depth strongly. The weakest effects are associated with  $\Delta y$  meaning that this factor has very little influence on the resulting depth.

that is, however, not below the significance threshold of 1.98. This remaining effect of  $\Delta y$  likely originated from the discrepancy between the observed spot diameter on a polished surface and the effective spot diameter within the pattern that was observed in Section 2.2.1.

It should be noted that using Equation (1) to calculate the overlap in the x- and y-direction for the patterns in Table 2 would result in an overestimation of the actual overlap by over 21%. This observation underlines the importance of the correct calculation route to systematically assess the effect of the laser parameters on the resulting surface. Equation (2) gives correct results for circular spots but is restricted in its applicability as it cannot be solved for  $\Delta x$  meaning it cannot be used to calculate the step sizes required to achieve the desired pulse number. In research, a discrepancy between the calculated and the true parameters can have major effects as the main objective of most parameter screenings lies in finding the ideal combination of pulse fluence and overlap that is required to achieve the desired effect. If these values are not calculated or reported correctly other research groups are not able to produce comparable surfaces without repeating the parameter screening themselves. Perhaps more importantly, errors in the parameter calculation can lead to major difficulties when the laser process is transferred to the industrial application as these transfers generally aim to translate the ideal laser parameters found in the lab to an industrial scale setup that generally employs vastly different input parameters like pulse power, spot size, and frequency. It is therefore crucial that parameters like overlap, pulse fluence, and accumulated fluence are calculated and reported as precisely as possible.

#### 3. Concluding Remarks

The calculation route developed in this contribution allows the straightforward calculation of the spot overlap and the accumulated fluence on an irradiated material's surface with higher precision than established methods. This is especially true for complex scanning paths or non-Gaussian beam profiles as the average number of pulses on a given point of the surface is calculated using only the step sizes and the spot area. This makes it possible to evaluate the influence of single process parameters with greater precision and to compare surfaces that were produced with different parameters or setups. Having access to

2201021 (5 of 7)

www.advancedsciencenews.com

www.aem-journal.com

the exact process parameters that resulted in a given structure also makes it possible to develop more precise models and make sound predictions for their respective properties. As stated earlier, the alternative of using established methods to calculate the overlap in the x- and y-direction can lead to an error of over 21% in the estimation of the overlap and consequently, the total accumulated fluence on the surface.

The main challenge of the technique lies in the determination of the effective spot size, a requirement for the determination of the pulse fluence. This is because the reference spots on a polished surface, which are generally used to determine the spot size, show a smaller diameter than the spots within the patterned surface, where the material usually shows a lower ablation threshold as a result of oxidation, roughening and damage accumulation. This problem is shared with established calculation routines as they too need to determine the effective spot diameter prior to the patterning.

Future works could employ a scan with bigger step sizes like the scan with one pulse per point conducted in this work to determine the spot diameter within a patterned surface experimentally. Alternatively, a focus on the precise laser-material interaction of the system could enable researchers to quantify the reduction of the ablation threshold caused by the patterning. This way the effective spot size within the patterned area could be accessed even for higher pulse numbers.

### 4. Experimental Section

Material Preparation: Titanium samples were cut out of a sheet (HMW Hanauer GmbH; 99.995 wt.%) using wire-cut electrical discharge machining (EDM).

The samples were prepared with the following steps: 1) Heat treatment in vacuum ( $\approx\!10^{-5}$  mbar) at 700 °C for 10 min. (heating/cooling rate: 1 °C min $^{-1}$ ). The main purpose of this treatment was to remove surface contaminations and potential thermal influences on the sample edges caused by the EDM. 2) Grinding: The samples were grinded using SiC grinding discs (#600–200 s; #1200–600 s) 3) OPS polishing: OPS + 2%  $H_2O_2$  (30%  $_{W/V}$ ) + 2%  $NH_3$  (25%  $_{V/V}$ ) for 8 min. 4) Etching in Beraha I stock solution for 45 s. This step is used to remove the deformation layer that forms on the Ti surface during the previous steps. 5) OPS polishing identical to three.

The resulting surfaces were cleaned in an ethanol ultrasonic bath for 10 min immediately after the polishing as well as immediately before and after the laser processing.

Laser Processing: The laser patterning was conducted using a Titanium-Sapphire laser with a centered wavelength of 800 nm, a pulse duration of 100 fs, and a repetition rate of up to 1 kHz. Ultrashort pulsed direct laser interference patterning was used to produce a line pattern with a periodicity of 3 µm within the individual laser spots. To achieve this, the main beam is split into two coherent sub-beams that are then brought to interference on the sample surface to create a periodical, line-shaped interference pattern. This pattern is then transferred to the material surface through a combination of direct ablation and thermal processes. Further details on the technique and the setup used can be found in Müller et al. [3] In contrast to a related work, [10] the setup uses a mask to reduce the beam diameter of the Gaussian beam from 8 to 3 mm. This way an approximate top hat profile is achieved.

The set of equations given in Section 2 was fed into an Excel spreadsheet and used to calculate the required structuring parameters. To illustrate this, the calculation process to produce the surface depicted in Figure 2a is given below.

Given parameters:

Spot Diameter:  $D = 79\mu m$ .

Desired number of pulses per point:  $n_{acc} = 1$ .

Laser Power: P = 26.7mW.

Expected losses in the DLIP system, here: L = 10%.

Laser repetition rate:  $f = 250 \,\text{Hz}$ . Additional condition:  $\Delta x = \Delta y$ .

Generally, this condition is not required. Instead, one of the step sizes can be chosen freely but should generally be a multiple of the DLIP periodicity in the respective direction.

$$E_{\text{Pulse}} = \frac{P \times (1 - L)}{f} = 96.12 \,\mu\text{J}$$
 (9)

$$F_{\text{Pulse}} = \frac{E_{\text{Pulse}}}{A_{\text{Spot}}} = 1.96 \,\mu\text{J cm}^{-2} \tag{10}$$

$$F_{\text{Pulse}} = \frac{E_{\text{Pulse}}}{\Delta x \times \Delta y} = \frac{E_{\text{Pulse}}}{\Delta x^2} \tag{11}$$

$$\Delta x = \Delta y = \sqrt{\frac{E_{\text{Pulse}}}{F_{\text{Pulse}}}} = 70 \,\mu\text{m} \tag{12}$$

Surface Analysis: An OLS4100 confocal laser scanning microscope was used to determine the respective spot diameters and surface profiles. Image segmentation was then performed using the software "Amira" (version 5.3.1). For the simplified images (Figure 2b,c) the image analysis was performed with the software "Gimp".

The analysis of the experimental design (Section 2.2.2) was performed using the software Minitab 19 (Version 2020.1).

### Acknowledgements

The authors gratefully acknowledge funding for the ZuMat project, supported by the State of Saarland from the European Regional Development Fund (Europäischen Fonds für Regionale Entwicklung, EFRE).

Open Access funding enabled and organized by Projekt DEAL.

### Conflict of Interest

The authors declare no conflict of interest.

### **Data Availability Statement**

The data that support the findings of this study are available on request from the corresponding author. The data are not publicly available due to privacy or ethical restrictions.

#### Keywords

direct laser interference patterning (DLIP), laser surface functionalization, laser surface oxidation, process control, pulse overlap, selective laser melting

Received: July 14, 2022 Revised: July 28, 2022 Published online:

2201021 (6 of 7)

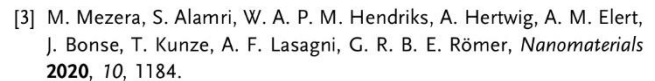
A. I. Aguilar-morales, S. Alamri, T. Kunze, A. F. Lasagni, Opt. Laser Technol. 2018, 107, 216.

<sup>[2]</sup> D. W. Müller, T. Fox, P. G. Grützmacher, S. Suarez, Sci. Rep. 2020, 10

www.advancedsciencenews.com

www.aem-journal.com

FNGINFFRING



- [4] A. J. Antończak, Ł. Skowroński, M. Trzcinski, V. V. Kinzhybalo, Ł.K. Łazarek, K. M. Abramski, Appl. Surf. Sci. 2014, 325, 217.
- [5] B. Voisiat, A. I. Aguilar-Morales, T. Kunze, A. F. Lasagni, Materials 2020, 13, 1.
- [6] S. Milles, M. Soldera, B. Voisiat, A. F. Lasagni, Sci. Rep. 2019, 9, 1.
- [7] C. Leone, S. Genna, A. Caggiano, V. Tagliaferri, R. Molitierno, Proc. CIRP 2015, 28, 64.
- [8] K. L. Wlodarczyk, A. Brunton, P. Rumsby, D. P. Hand, Opt. Lasers Eng. 2016, 78, 64.
- [9] L. Shanjin, W. Yang, Opt. Lasers Eng. 2006, 44, 1067.
- [10] Y. Singh, J. Singh, S. Sharma, A. Sharma, J. Singh Chohan, *Mater. Today Proc.* 2021, 48, 1021.
- [11] P. Bajaj, J. Wright, I. Todd, E. A. Jägle, Addit. Manuf. 2019, 27, 246.
- [12] S. C. Chou, M. Trask, J. Danovitch, X. L. Wang, J. P. Choi, M. Brochu, Mater. Charact. 2018, 143, 27.
- [13] Y. Lo, B. Liu, H. Tran, Int. J. Adv. Manuf. Technol. 2019, 105, 2989.
- [14] N. Singh, P. Hameed, R. Ummethala, G. Manivasagam, K. G. Prashanth, J. Eckert, Mater. Today Adv. 2020, 8, 100097.
- [15] A. Ghosh, D. Misra, S. K. Acharyya, Lasers Manuf. Mater. Process. 2019, 6, 228.
- [16] A. F. Lasagni, C. Gachot, K. E. Trinh, M. Hand, A. Rosenkranz, T. Roch, S. Echhardt, T. Kunze, M. Bieda, D. Günther, V. Lang, F. Mücklich, in Laser-Based Micro- and Nanoprocessing Vol. XI, San Diego Convention Center, San Diego, California, United States 2017, p. 1009211.
- [17] M. K. Mohammed, U. Umer, O. Abdulhameed, H. Alkhalefah, Appl. Sci. 2019, 9, 1.
- [18] J. Jiménez, Á. Gómez, M. D. Buhrmester, V. Alexandra, W. Harvey, W. B. Swann, Soc. Sci. Comp. Rev. 2015, 5, 215.
- [19] E. W. Weisstein, Mathworld. Wolfram. Com, 2022, https://mathworld. wolfram.com/Circle-CircleIntersection.html (accessed: May 2022).

- [20] M. Liu, R. Zhou, Z. Chen, H. Yan, J. Cui, W. Liu, J. H. Pan, M. Hong, Coatings 2020, 10, 450.
- [21] X. Miao, M. Wu, J. Han, H. Li, X. Ye, Materials 2020, 13, 3940.
- [22] C. Zwahr, D. Günther, T. Brinkmann, N. Gulow, S. Oswald, Adv. Healthc. Mater. 2017, 6, 1.
- [23] C. Zwahr, R. Helbig, C. Werner, A. F. Lasagni, Sci. Rep. 2019, 9, 1.
- [24] C. Florian, R. Wonneberger, A. Undisz, S. V. Kirner, K. Wasmuth, D. Spaltmann, J. Krüger, J. Bonse, Appl. Phys. A: Mater. Sci. Proc. 2020, 126, 1.
- [25] A. Peter, A. H. A. Lutey, S. Faas, L. Romoli, V. Onuseit, T. Graf, Opt. Laser Technol. 2020, 123, 105954.
- [26] F. Schell, S. Alamri, A. Hariharan, A. Gebert, A. F. Lasagni, T. Kunze, Mater. Lett. 2022, 306, 130920.
- [27] L. Gemini, M. Faucon, L. Romoli, R. Kling, in Laser-Based Micro- and Nanoprocessing, Vol. XI, San Diego Convention Center, San Diego, California, United States 2017, p. 10092.
- [28] A. H. A. Lutey, L. Gemini, L. Romoli, G. Lazzini, F. Fuso, M. Faucon, R. Kling, Sci. Rep. 2018, 8, 1.
- [29] C. Du, C. Wang, T. Zhang, L. Zheng, ACS Appl. Bio Mater. 2021, 5, 272.
- [30] H. Zhu, M. Ehrhardt, P. Lorenz, J. Zajadacz, J. Lu, K. Zimmer, Appl. Phys. A: Mater. Sci. Proc. 2019, 125, 1.
- [31] K. Yin, H. Du, X. Dong, C. Wang, J. A. Duan, J. He, Nanoscale 2017, 9, 14620.
- [32] I. Gnilitskyi, T. J. Y. Derrien, Y. Levy, N. M. Bulgakova, T. Mocek, L. Orazi, Sci. Rep. 2017, 7, 1.
- [33] P. T. Mannion, J. Magee, E. Coyne, G. M. O'Connor, T. J. Glynn, Appl. Surf. Sci. 2004, 233, 275.
- [34] F. Di Niso, C. Gaudiuso, T. Sibillano, F. P. Mezzapesa, A. Ancona, *Phys. Proc.* **2013**, *41*, 698.
- [35] S. E. Kirkwood, A. C. Van Popta, Y. Y. Tsui, R. Fedosejevs, Appl. Phys. A: Mater. Sci. Proc. 2005, 81, 729.
- [36] L. M. Machado, R. E. Samad, W. De Rossi, N. Dias, Opt. Express 2012, 20, 4114.

# Single-step Production of Photocatalytic Surfaces via Direct Laser Interference Patterning of Titanium

Tobias Fox<sup>1</sup>, Pablo Maria Delfino<sup>1</sup>, Francisco Cortés<sup>1</sup>, Christoph Pauly<sup>1</sup>, Daniel Wyn Müller<sup>1</sup>, Max Briesenick<sup>2</sup>, Guido Kickelbick<sup>2</sup>, Frank Mücklich<sup>1</sup>

Published "ChemNanoMat" 2023 (CiteScore 6.1 by 2023) https://doi.org/10.1002/cnma.202300314

#### Abstract:

State of the art approaches to produce photocatalytic surfaces generally require multiple processing steps to achieve highly active surfaces. Following recent trends to facilitate the production of active surfaces, this work presents a single-step method to create porous photocatalytic surfaces via direct laser interference patterning (DLIP) of a titanium substrate with pulses in the picosecond range. The resulting surfaces contain a variety of titanium oxides while both their composition and morphology can be controlled through the laser process parameters. This makes it possible to tailor these surfaces for specific applications such as antimicrobial surfaces, implant materials or water treatment. Surface characterization was executed by applying scanning electron microscopy complemented by focused ion beam cross-sectioning and energy dispersive X-ray spectroscopy as well as gracing incidence X-ray diffractometry. The photocatalytic activity achieved by different laser parameters is assessed by methylene blue degradation under UV-A light. As DLIP is already established in industrial applications, this approach could greatly facilitate the use of photocatalytic surfaces for water treatment or medical applications, as it does not require nanoparticle synthesis or additional coating steps.

#### **Author Contributions:**

Conceptualization: Lead; Data curation: Lead; Formal analysis: Lead; Investigation: Lead; Methodology: Lead; Writing – original draft: Lead

<sup>&</sup>lt;sup>1</sup> Chair of Functional Materials, Department of Materials Science, Saarland University, 66123, Saarbrücken, Germany.

<sup>&</sup>lt;sup>2</sup> Inorganic Solid-State Chemistry, Department of Chemistry, Saarland University, 66123, Saarbrücken, Germany.





Check for updates

www.chemnanomat.org

# Single-step Production of Photocatalytic Surfaces via Direct Laser Interference Patterning of Titanium

Tobias Fox,\*<sup>[a]</sup> Pablo Maria Delfino,<sup>[a]</sup> Francisco Cortés,<sup>[a]</sup> Christoph Pauly,<sup>[a]</sup> Daniel Wyn Müller,<sup>[a]</sup> Max Briesenick,<sup>[a]</sup> Guido Kickelbick,<sup>[a]</sup> and Frank Mücklich<sup>[a]</sup>

State of the art approaches to produce photocatalytic surfaces generally require multiple processing steps to achieve highly active surfaces. Following recent trends to facilitate the production of active surfaces, this work presents a single-step method to create porous photocatalytic surfaces via direct laser interference patterning (DLIP) of a titanium substrate with pulses in the picosecond range. The resulting surfaces contain a variety of titanium oxides while both their composition and morphology can be controlled through the laser process parameters. This makes it possible to tailor these surfaces for specific applications such as antimicrobial surfaces, implant

materials or water treatment. Surface characterization was executed by applying scanning electron microscopy complemented by focused ion beam cross-sectioning and energy dispersive X-ray spectroscopy as well as gracing incidence X-ray diffractometry. The photocatalytic activity achieved by different laser parameters is assessed by methylene blue degradation under UV-A light. As DLIP is already established in industrial applications, this approach could greatly facilitate the use of photocatalytic surfaces for water treatment or medical applications, as it does not require nanoparticle synthesis or additional coating steps.

#### Introduction

Photocatalytic materials can be used in water treatment, air purification and sterilization since they possess the ability to generate highly reactive species when irradiated with a proper light source. As a photocatalytic material, titanium dioxide shows high chemical stability, low cost and a sufficiently high bandgap energy to produce water-based radicals which makes it the most used photocatalytic material to date. [1-5] Of the three TiO<sub>2</sub> allotropes that are stable at room temperature (i.e., anatase, rutile and brookite), anatase shows the highest photocatalytic activity. However, multiple studies have shown that the combination of anatase and rutile results in a significant increase in activity, as their different affinity for electrons and holes facilitates electron-hole separation and thereby prevents recombination. [3,4,6-8] It should however be noted that a type two heterojunction between the two phases is required to enable the respective charge carriers to travel from one phase to the other. This requirement can pose a challenge especially for nanoparticle powders but also for photocatalytic surfaces with low interconnectivity of the present phases. [9,10] The commercial product Evonik AEROXIDE® TiO2 P25 makes use of the synergistic effects of the combination of rutile and anatase by employing 20% rutile and 80% anatase.[11] These nanoparticles can be applied to a surface either by means of a binder or by techniques like thermal spraying or suspension spraying. Both approaches significantly reduce the active surface of the particles and especially for the binder-based films, degradation of the binder limits the film's lifetime.<sup>[4,12–14]</sup>

For these reasons recent research aims to facilitate the production of photocatalytic surfaces by employing single step production methods and alternative means to fixate the active agents on a carrier material. Examples for these strategies include but are not limited to: Plasma electrolytic oxidation, adsorption of nanoparticles to porous carriers, in-situ calcination of porous matrices containing active particles and the synthesis of fibrous active materials.<sup>[5,15–18]</sup>

This work explores a bottom-up approach, where direct laser interference patterning (DLIP) is used to produce a suitable oxidic film on titanium substrates with a single processing step. Laser oxidation is a well-established process to produce dense films of titanium oxide for optical purposes or to increase corrosion resistance. [19,20] Thereby laser based processes can have distinct advantages compared to electrolytic or chemical surface treatments as they can be incorporated in existing manufacturing chains with relative ease and can also be used for parts with complex shapes. In a recent approach relatively long pulse durations (200 ns) were used in combination with silicon monoxide particles to produce biocompatible surfaces that also showed some degree of photocatalytic activity. However, the applied laser oxidation has shown to produce mainly metastable, oxygen deficient titanium oxides which are not ideal for photocatalytic applications. [21] Short and ultrashort pulses are more promising for the production of active surfaces as they have shown to produce oxides with high active surface areas and can produce both, anatase and rutile depending on the used fluence.[22-27] In the experiments presented here, DLIP was applied at a pulse duration of 12 ps, since a higher amount of oxide is produced within this pulse

<sup>[</sup>a] T. Fox, P. Maria Delfino, F. Cortés, Dr. C. Pauly, D. Wyn Müller, M. Briesenick, Prof. Dr. G. Kickelbick, Prof. Dr. F. Mücklich Chair of Functional Materials, Saarland University, Campus D3.3, Saarbrücken 66123 (Germany) E-mail: tobias.fox@uni-saarland.de

<sup>© 2023</sup> The Authors. ChemNanoMat published by Wiley-VCH GmbH. This is an open access article under the terms of the Creative Commons Attribution License, which permits use, distribution and reproduction in any medium, provided the original work is properly cited.



**CHEMNANOMAT** Research Article

regime than with even shorter pulses while the power density was still large enough to generate anatase.

The resulting surfaces are highly porous and contain variable stoichiometries of rutile, anatase and other metastable titanium oxides. Methylene blue (MB) degradation experiments were conducted to measure the activity of the produced surfaces, so that the influence of laser parameters like accumulated fluence and pulse number as well as the applied DLIP pattern and the cycling stability of the produced samples could be investigated.

#### **Results and Discussion**

#### **Surface Characterization**

The DLIP process used in this work not only alters the surface topography through ablation and redeposition of material but also produces a highly porous oxide layer at the topographic maxima of the pattern. To understand the effect of various laser parameters on the resulting surfaces and their photocatalytic activity a broad spectrum of varying surfaces was produced and investigated with scanning electron microscopy (SEM) and grazing incidence X-Ray diffraction (GI-XRD) before performing the methylene blue (MB) degradation assays. While the results of the MB degradation are presented for all samples, the following sections discuss the results of the surface characterization with the aid of representative images and spectra to keep the frame of this work. As explained in greater detail in the experimental section, the sample denotation follows the following scheme:

- pattern type (line/cross) and periodicity
- accumulated fluence
- number of pulses

#### Morphology and chemistry of the surfaces

The oxide layers produced in the DLIP process were imaged via secondary electrons and FIB cross sections. Especially the cross sections show a general trend towards deeper patterns and thicker oxide layers with increasing accumulated fluence (Figure 1). While the secondary electron (SE) contrast does not allow to distinguish between titanium substrate and the redeposited porous oxide layer, secondary ion (SI) contrast clearly separates both as the oxide shows a significantly higher sputter rate under irradiation by the Ga ion beam than the titanium substrate. This way, it could be shown that the original sample surface stayed intact at the locations with low laser power while material that was ablated at the intensity maxima of the interference pattern has agglomerated at the topographical peak regions (Figure 1f).

It is expected that oxidation occurs within the plasma plume and during material transport, similar to Zwahr et al. [28] Hence, the valleys of the patterns act as sources for particles that can agglomerate at the topographic peaks where they are not removed by consecutive laser pulses as depicted in Figure 2. As both nucleation and oxidation primarily occur within the plasma plume and its close vicinity the laser parameters and the existing surface are expected to affect the size of particles and agglomerates as well as their chemical composition. Since the cooling rate of matter within the plasma plume is largely a result of adiabatic cooling caused by the plumes expansion, a faster expanding plume experiences a higher cooling rate. Therefore, a lower cooling rate is expected for the deeper patterns as the plume's expansion is restricted within the patterns minima as depicted in Figure 2. Additionally, deeper patterns require a longer transportation path within the plasma plume. Both conditions are expected to increase the size and alter the phase composition of the resulting particles which is likely to affect the topography of the resulting agglomerates on the sample surface. [29,30]

In contrast, surfaces that were produced without an interference pattern (i.e. with only a single beam) show only a thin, relatively homogenous oxide layer throughout the surface. As in this case the whole surface was exposed to laser radiation the resulting particles could not agglomerate and the oxide laver stayed thin even at high fluences as can be seen in Figure 1 h.

To verify the observations made in Figure 1 f) regarding the chemical composition, an EDS mapping was performed exemplarily on an 10-1000-3300 sample. As expected, the mapping in Figure 3 shows a clear oxygen signal in the porous structures atop the remaining titanium substrate.

Cross structures were produced by rotating the sample by 90° between two line-like patterning procedures of which each applied half the total number of pulses on the surface. The cross structures show a very similar behavior as the line pattern as an increase in accumulated fluence leads to an increase in pattern depth and oxidation. For low pulse numbers the cross shaped patterning leads to a significant removal of oxide. As can be seen in Figure 4a) the area fraction of the pattern maxima is relatively small compared to that of the minima. This leads to a relative reduction of the oxide content in the surface. In contrast, the sample depicted in Figure 4b) which was produced with high accumulated fluence shows more oxidation and almost resembles a line pattern. This is because the cross pattern is produced by two subsequent line scans and the oxide produced by the second line scan partially covers the initial pattern. A change in pulse energy between the samples  $10-500-1650~(30~\mu J)$  and  $10-500-3500~(10~\mu J)$  shows that the pulse energy affects the oxide topography as the latter, which was patterned with many low-fluence pulses shows a more porous oxide layer with a larger active surface than the sample produced with fewer, high-fluence pulses. It can however be noted that for the high fluence sample (Figure 4b) which was produced with the high pulse energy, the oxide also shows an open pored topography that rather resembles the surfaces produced with low pulse energy (Figure 4d).

vinloaded from https://oniheilbrary.wiley.com/doi/10.1002/cmna.202300314 by Universitated Des Sarlandes, Wiley Online Library on [08/08/2023]. See the Terms and Conditions (https://onlinelibrary.wiley.com/erms-and-conditions) on Wiley Online Library for rules of use; OA archies are governed by the applicable Creative Commonsorum.

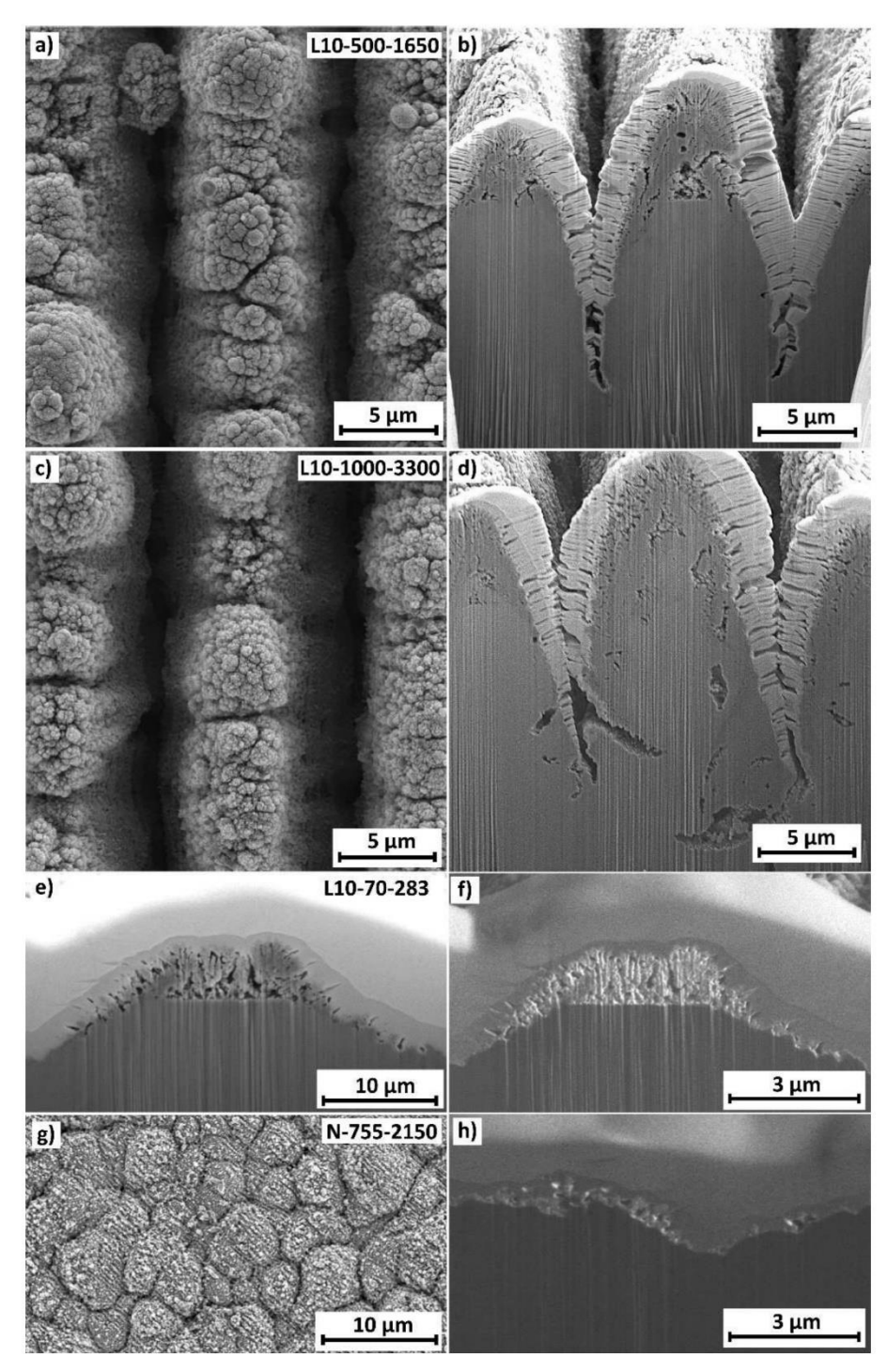


Figure 1. a–d) SEM images of surfaces with 10 μm periodicity in SE contrast and their FIB cross sections showing an increase in porosity and depth with increasing accumulated fluence. e–f) The same section of a 10 μm pattern imaged with secondary electrons (e) and secondary ions (f). The contrast created by the difference in sputter rate makes it possible to see the oxide layer in much more detail when secondary ions are used. g–h) Single-beam surface without an interference pattern (SE contrast) and cross section of its respective oxide layer (SI contrast).

#### Phase composition analysis

This section summarizes the most relevant findings of the performed XRD analysis with aid of representative diffractograms shown in Figure 5. As can be seen in the two diffractograms of line-like patterns L10-100-330 and L10-500-1650, a

trend towards more oxide formation for higher accumulated fluences is observed. The former, treated with 100 J/cm² shows predominantly the  $\alpha$ -Ti peaks from the substrate as well as the metastable hongquite (TiO) phase. The second sample that was treated with 1650 pulses per point instead of 330 shows a lower Ti signal and instead, both anatase and rutile together with a

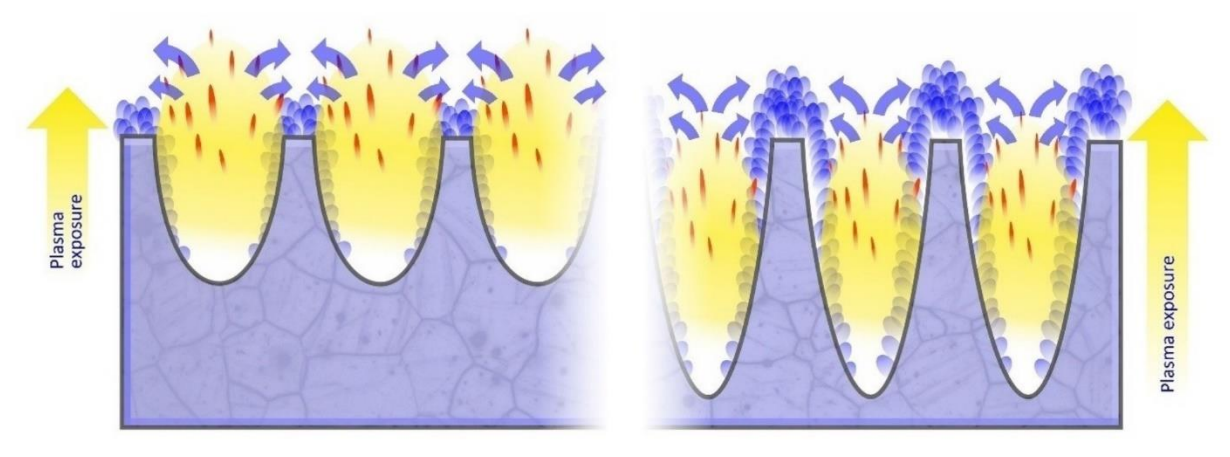


Figure 2. Proposed mechanism of material transport from topographic minima to maxima with simultaneous oxidation for shallow and deep patterns.

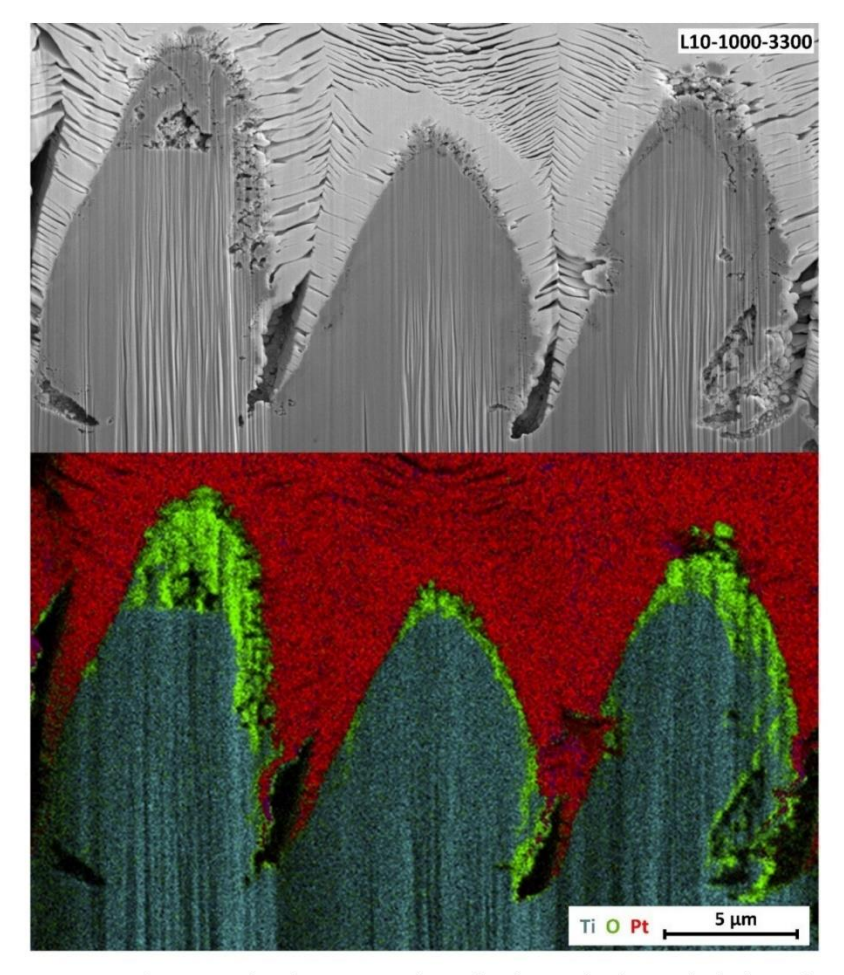
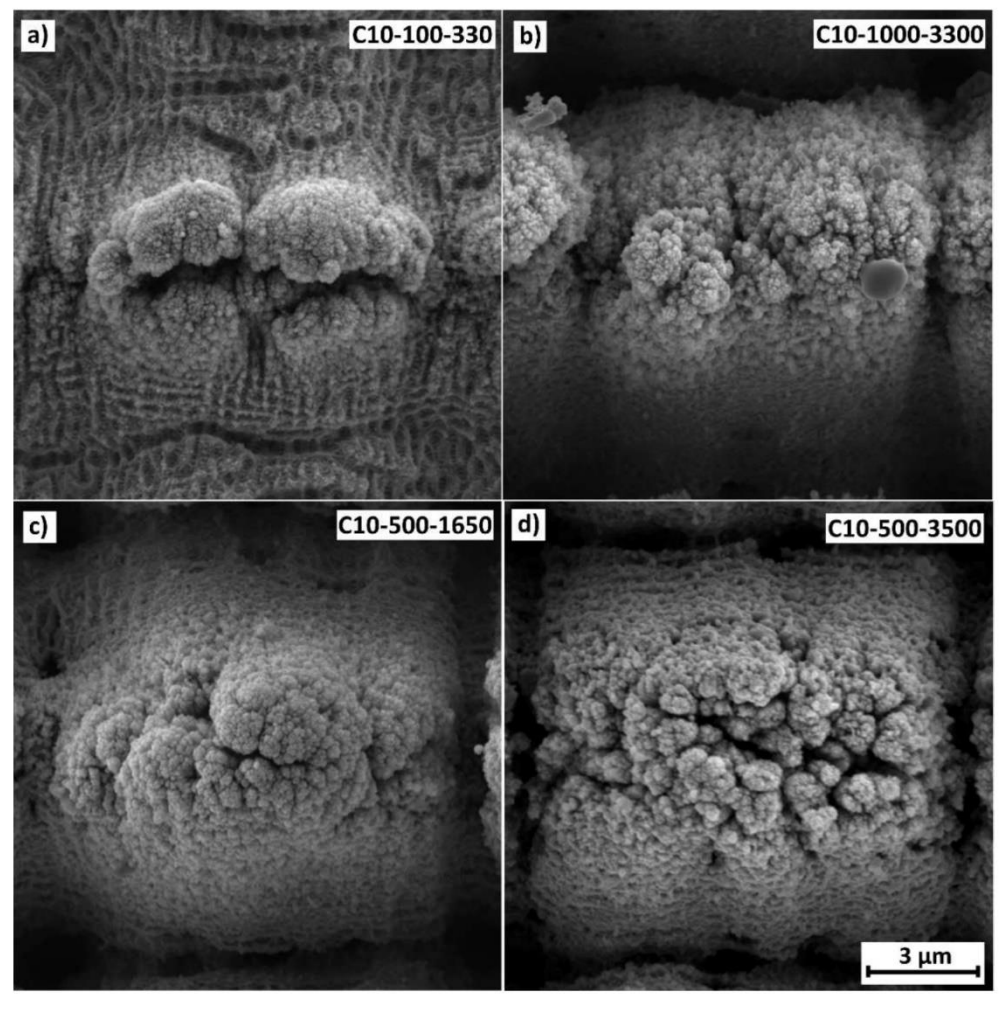


Figure 3. EDS area scan of a FIB cross section from a sample with 10  $\mu$ m periodicity. The element distribution clearly shows that a porous oxide layer is present at the structure's maxima.

minor peak at  $32.7^{\circ}$  that indicates the presence of tistarite ( $Ti_2O_3$ ).

The authors assume that the incomplete oxidation of the first sample is a result of the limited amount of oxygen that is present in the plasma plumes of the initial pulses. This low oxygen content not only leads to the formation of oxygen

deficient titanium oxides like TiO and  ${\rm Ti_2O_3}$  but can also cause the reduction of any existent  ${\rm TiO_2}$  by the excess titanium. However, if the pulse number is increased the re-ablation of these oxides leads to an increased oxygen content within the plasma which facilitates the formation of the more stable  ${\rm TiO_2}$  phases. To validate this oxidation mechanism most of the



**Figure 4.** SEM images of cross structures. Sample C10-500-3500 was produced with the low pulse energy of 10  $\mu$ J, the rest with the high pulse energy of 30  $\mu$ J.

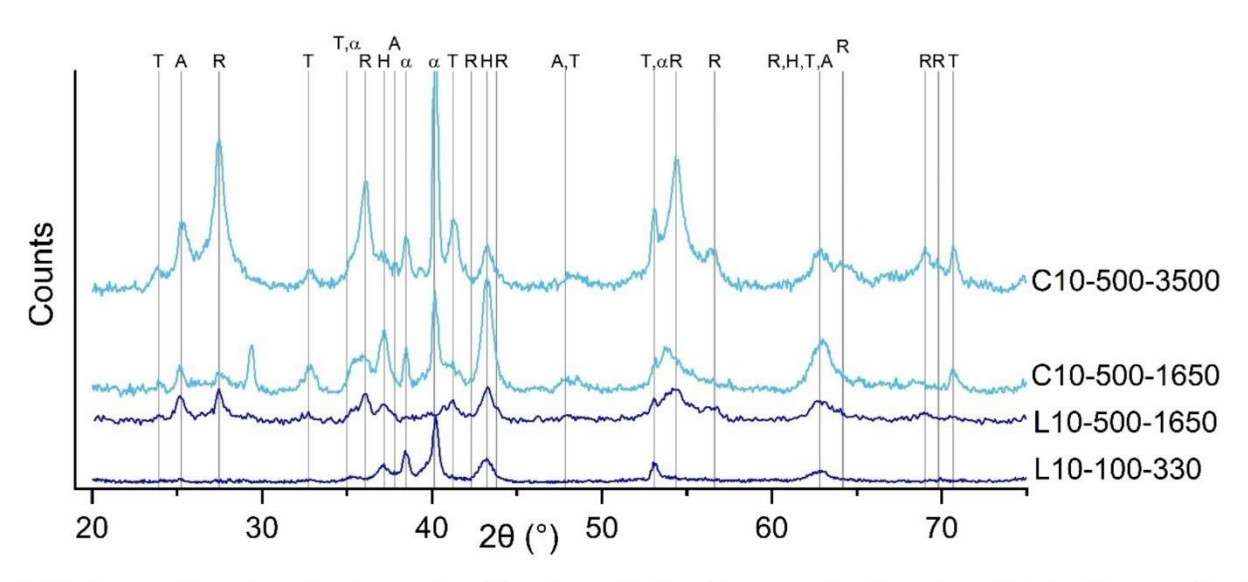


Figure 5. Diffractograms of line patterns (L) and cross patterns (C) produced with different laser parameters. The peaks are labelled as follows:  $\alpha$ :  $\alpha$ -Titanium; R: Rutile; A: Anatase; T: Tistarite ( $Ti_2O_3$ ); H: Hongquite (TiO). The unlabelled peaks at 29.4° and 39,3° originate from the calcium carbonate in the clay that was used to fix the samples.

surface oxide was removed by ultrasonication in ethanol for 10 minutes. The resulting surface lacked the porous oxide structures and only possessed a relatively compact layer of the oxide that forms in the first stages of oxidation. Figure 6 compares the diffractogram of the ultrasonicated sample to its original state. It can be observed that the cleaning removed almost all  ${\rm TiO_2}$  and  ${\rm Ti_2O_3}$  while the intensity of the titanium substrate and the  ${\rm TiO}$  phase increased. This indicates that the majority of the  ${\rm TiO_2}$  is present in the porous top layers that were deposited last while the underlying materials contains more oxygen deficient  ${\rm TiO}$ .

When comparing the line pattern L10-500-1650 with the cross pattern C10-500-1650 in Figure 5, it becomes clear that although the same patterning parameters were used, the resulting surfaces present different oxide layers. The cross pattern presents more unstable oxides, namely tistarite (Ti<sub>2</sub>O<sub>3</sub>) and especially hongquite (TiO), and fewer rutile in its surface than the line pattern. This difference in the oxide composition likely results from the partial removal of oxide by the second scan and therefore an insufficient agglomeration of oxide in the surface. The difference in signal from the titanium substrate is probably not a result of the oxide thickness as the SEM analysis has shown that all samples possess a thick oxide layer at the structure peaks and almost none in the valleys. Instead, the difference in titanium signal likely results from the sample positioning during the XRD experiment. This is because the line pattern was aligned parallel to the incoming X-ray radiation to prevent shadowing effects. However, even a small offset in this angle could lead to a shadowing of the valleys and consequently, a lower titanium signal. As the cross-patterns are less susceptible to this misalignment and present less overall peak area they show a stronger substrate signal than the linepatterns.

When the C10-500-3500 is compared to the C10-500-1650 that was exposed to the same accumulated fluence but with a lower number of stronger pulses, it can be observed that the

latter shows a strong signal of the metastable TiO and Ti<sub>2</sub>O<sub>3</sub> and less signal from anatase and rutile. As the difference in pulse energy marks the only difference between these two samples, it can be concluded that the fewer strong pulses favor the formation of the metastable TiO rather than the more stable TiO<sub>2</sub> phases. This effect can also be attributed to the oxide formation inside the plasma plumes produced by the individual pulses. As the stronger pulses ablate more material, the titanium to oxygen ratio favors metastable oxygen deficient oxides like TiO and Ti<sub>2</sub>O<sub>3</sub>. [31,33] In contrast, the weaker pulses ablate less material per pulse creating a more favourable titanium to oxygen ratio. Additionally, the higher number of pulses leads to a continuous re-ablation of the oxides which also increases the oxygen ratio in the plasma plume. As both, increased pressure and fast cooling rates can lead to the amorphization of particles, it is reasonable to assume that a significant portion of the observed oxide could be amorphous, which cannot be detected reliably with XRD.[30,34] Future research should therefore focus on TEM, XPS and Kelvin probe imaging to unequivocally determine the spatial distribution of phases and the presence of heterojunctions and amorphous phase.

#### Methylene Blue Degradation

#### First parameter screening

In a first experiment, the accumulated fluence on the sample surface ( $F_{acc}$ ) and the number of pulses by which this fluence was delivered ( $N_{acc}$ ) were varied in a relatively low fluence regime. Additionally, two different structural periodicities (3  $\mu$ m and 10  $\mu$ m) were investigated. To quantify the photocatalytic activity samples were brought in contact with 50  $\mu$ M methylene blue solution and exposed to UV-A light (365 nm) for 2 hours. Photocatalytic degradation of the organic methylene blue dye

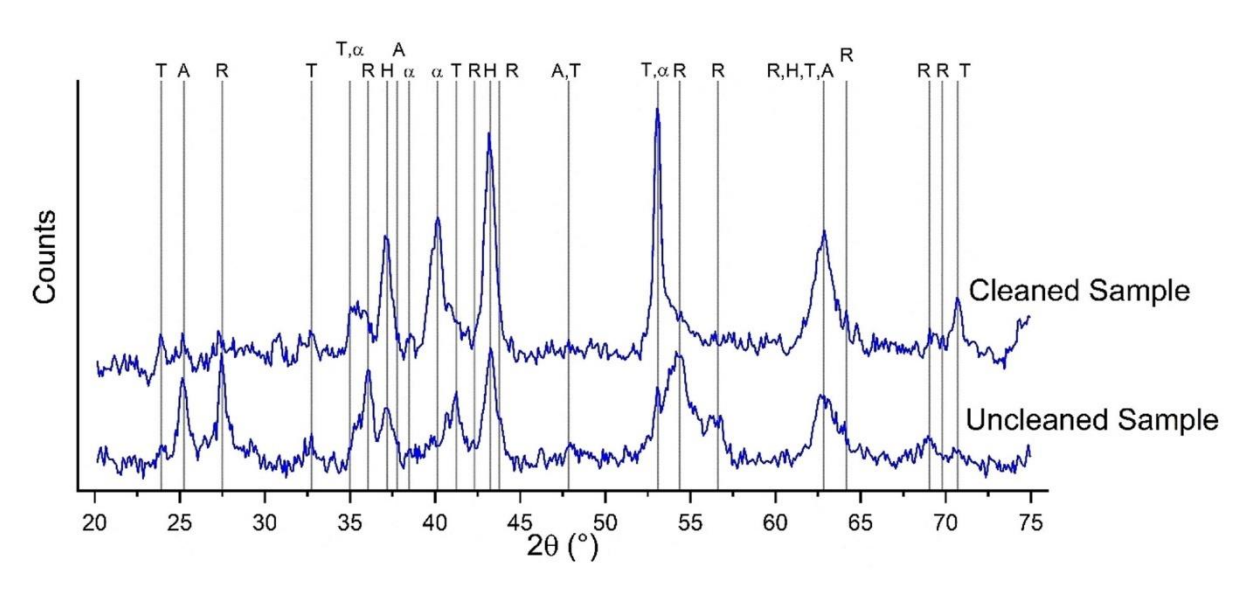


Figure 6. X-ray diffractograms of cleaned and uncleaned samples of the L10-500-1650 variant. The ultrasonic cleaning has removed most of the rutile and anatase from the surface.

causes a color change of the sample solution that can be quantified and correlated to a change in concentration using UV-Vis spectroscopy. This way the photocatalytic activity of individual samples can be compared.

The results of the methylene blue experiment are shown in Figure 7. For the plot, the concentration of the remaining solution C was normalized with the initial concentration. As expected, the titanium reference showed no activity, whereas the degradation on the other samples varies between 0% and 48%. High activity was observed especially on the samples with accumulated fluences over 700 J/cm² and over 2000 pulses per point in the surface. The pattern periodicity does not seem to play a major role. To improve the clarity of the following plots the untreated titanium references are not plotted in the subsequent figures as no significant changes could be observed.

The results depicted in Figure 7 indicate that higher accumulated fluence generally increases the photocatalytic activity. This is consistent with the observations made in the sections 2.1.1 and 2.1.2 where it was shown that higher

accumulated fluences not only produce a more porous oxide layer at the structure peaks but also tend to produce higher amounts of the photocatalytically active TiO<sub>2</sub> phases (especially anatase). The TiO produced by the lower accumulated fluences seems to show no relevant photocatalytic activity.

#### DLIP influence

To investigate the effect of the DLIP pattern on the resulting activity in more detail, surfaces without an interference pattern were produced and tested together with the line-like structures. This was done by modifying the laser setup to work with only a single beam. The laser power was adjusted accordingly, to keep the number of pulses and the accumulated fluence on the surface the same. The SEM images of the resulting surfaces in Figure 8 show that on all surfaces, a sub structure consisting of laser induced periodic surface structures (LIPSS) is observable. The periodicity of ca. 400 nm is consistent with expected values for green light on titanium. [35,36]

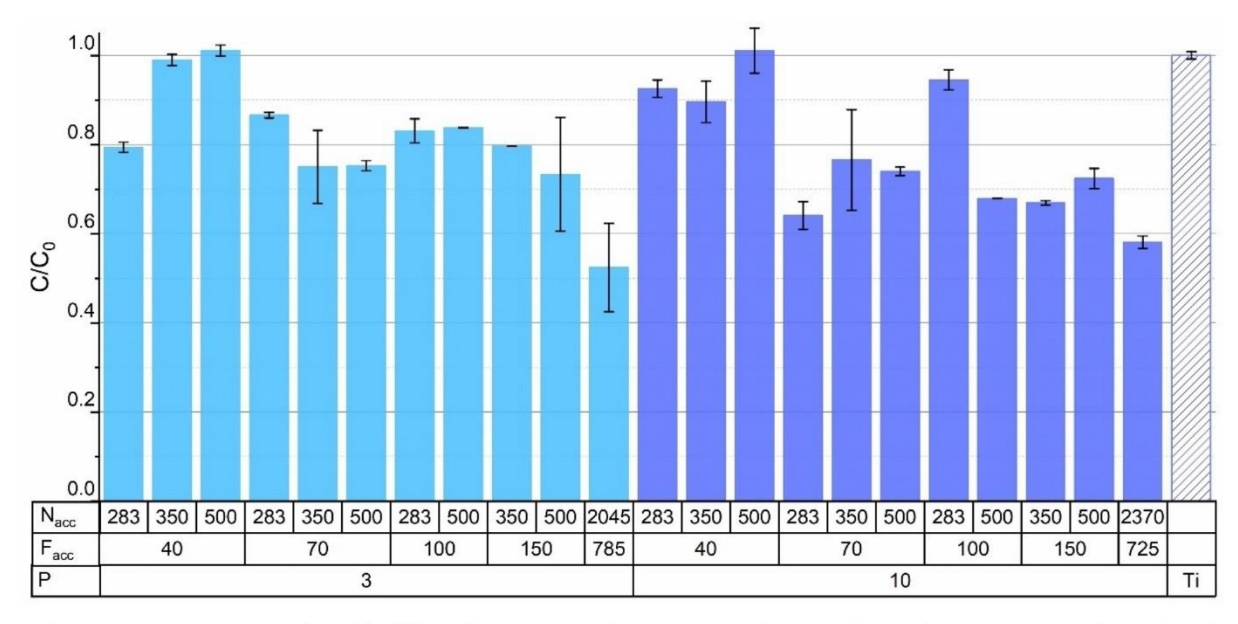


Figure 7. Change in MB-concentration achieved by different laser structures after 120 minutes of UV-A irradiation. The parameters varied are P (periodicity in  $\mu$ m),  $F_{acc}$  (accumulated fluence in J/cm<sup>2</sup>) and  $N_{acc}$  (number of pulses).

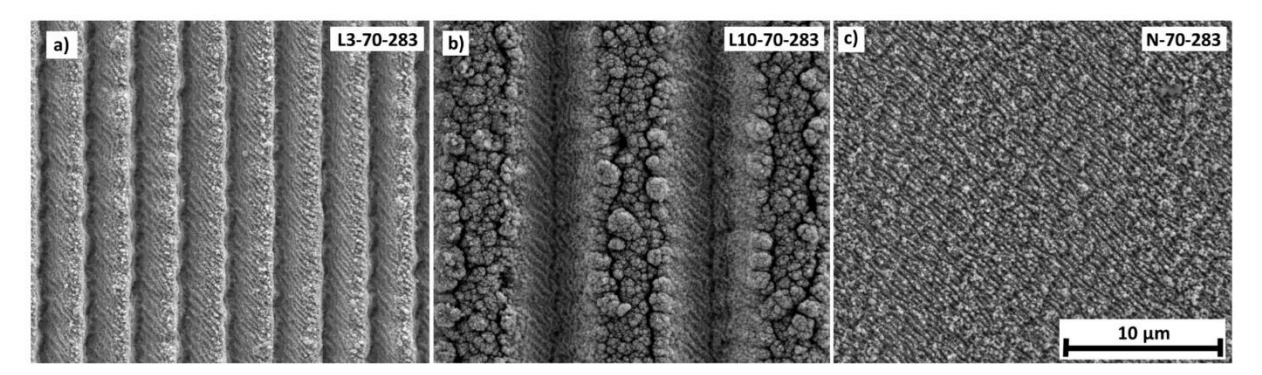


Figure 8. SEM images of samples with 3  $\mu m$  periodicity, 10  $\mu m$  periodicity and no interference pattern.

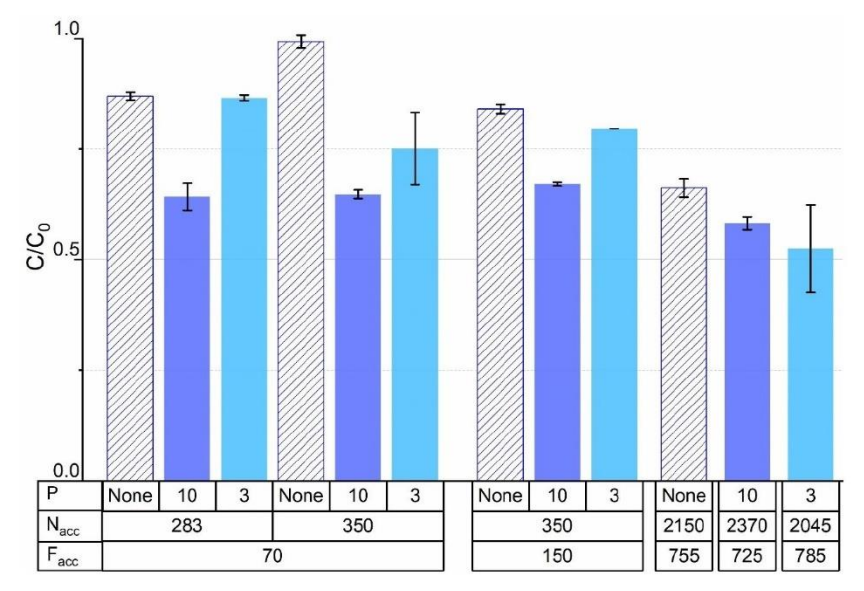


Figure 9. Effect of pattern type on MB degradation.

As can be seen from the plot in Figure 9, the two line-like patterns show a difference in reactivity for lower fluences. However, in the higher fluence regime both DLIP patterns show a larger activity than the sample that was laser-treated with only one beam.

These results can be explained by the oxide topography depicted in Figure 8. It was observed that the 10  $\mu$ m interference pattern offered more space for the agglomeration of oxides while only little oxide could agglomerate on the 3  $\mu$ m pattern. At higher accumulated fluences this effect was mitigated as the patterns become deeper and the topography peaks are more protected from the ablation plume occurring in the valleys. As was observed in Figure 1 the surface without interference pattern could not agglomerate oxide and instead expresses a relatively thin homogenous oxide layer that is not as photocatalytically active as the surfaces produced with a DLIP pattern.

#### Cycling stability

To investigate the stability of the produced surfaces over multiple cycles, two sample sets were tested four times in the same setup. All samples were cleaned with deionized water after each test to remove any residual MB. The results of the experiment are presented in Figure 10. While there is a minor trend towards a smaller activity, the overall activity did not decrease substantially over the observed number of cycles. Although promising, additional experiments are needed to ensure that the produced surfaces are stable for a number of cycles that is sufficient for industrial applications.

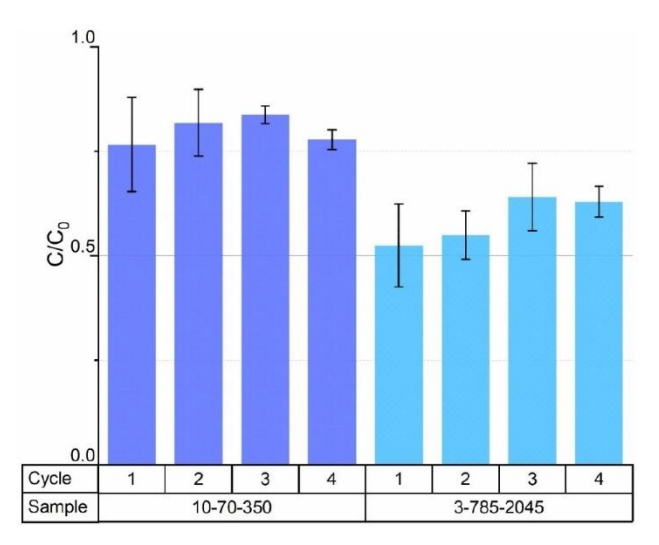


Figure 10. Cycling stability of two different surfaces over four identical cycles.

# Investigation of higher accumulated fluences and cross structures

As the previous experiments showed especially promising results for higher fluences, additional experiments with accumulated fluences between 100 and 1000 J/cm<sup>2</sup> and both line and cross structures with 10 µm periodicity were performed.

The results presented in Figure 11 show that the general trend towards larger activities for higher accumulated fluences continues. The cross structures tend to perform better than the line-like structures especially at higher pulse numbers. Additionally, for the cross-like structures, the number of pulses plays a significant role in the resulting activity as can be seen especially in the higher fluence regime where the samples produced with relatively few stronger pulses (30 µJ per pulse) performed better



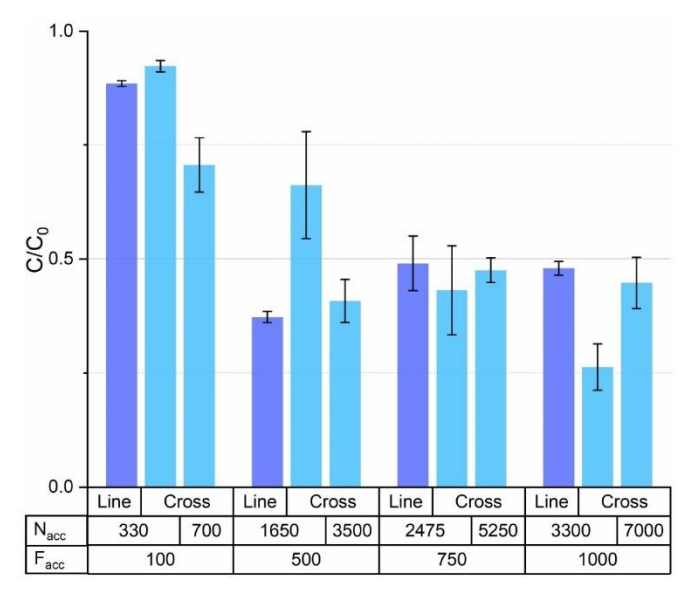


Figure 11. Cross and line structures with low and high pulse energy.

Table 1. Apparent kinetic constants after 120 minutes for the MB degradation of the line and cross patterns from Figure 11. F<sub>acc</sub> [J/cm<sup>2</sup>]  $N_{acc} \left[ -- \right]$  $k_{Line}$  [1/h] k<sub>Cross</sub> [1/h] 100  $0.061 \pm 0.003$ 330  $0.040 \pm 0.005$ 700  $0.175 \pm 0.034$ 500 1650  $0.209 \pm 0.074$  $0.462 \pm 0.045$ 3500  $0.449 \pm 0.048$ 750  $0.423 \pm 0.080$ 2475  $0.477 \pm 0.124$ 5250  $0.372 \pm 0.023$ 1000 3300  $0.669 \pm 0.078$  $0.367 \pm 0.011$ 7000  $0.403 \pm 0.051$ 

than those produced with a higher number of weaker pulses (10 µJ per pulse).

When correlating the results of the methylene blue degradation with the XRD analysis it can be observed that high amounts of both rutile and anatase are found in the more active samples while the metastable oxides hongquite and tistarite seem to lower the photocatalytic activity. As previous research has shown, tistarite can increase the photocatalytic activity if heterojunctions to rutile are present. Hence, it can be assumed that the reduced activity of the C10-500-1650 sample can be attributed to the abundance of TiO as well as amorphous titanium oxides that were not be detected by the XRD.[37,38] Additionally, as was discussed in section 2.1.1, the C10-500-1650 showed a much lower surface area than the other two samples prepared with 500 J/cm<sup>2</sup>. This likely also has a negative impact on its activity. For higher accumulated fluences the effect on the surface area was less pronounced as discussed in section 2.1.1. Additionally for the higher accumulated fluences the cross structures with fewer, stronger pulses tend to express more anatase as those with many weaker pulses.

From the measurements shown in Figure 11, the respective kinetic constants k were calculated using Eq. (1) assuming first order degradation kinetics. Here t represents the duration of the experiment which was two hours. The results for are listed in Table 1.

$$k = \frac{1}{t} \ln \left( \frac{C_o}{C} \right) \tag{1}$$

As there exists a wide variety of setups to perform this kind of degradation experiments, the comparison to results of different experiments is nontrivial. Table 2 gives an overview of different setups and the degradation rates that were observed. The highest degradation rate observed in this work is highlighted. While this rate is relatively low compared to several other publications, it should be noted, that those works for the

Table	2. Overview of degradation rates of diff	erent setups. The res	ults of this contributio	n are highlighted.	
	Material	Kinetic constant [1/h]	Concentration of MB solution [ $\mu$ M]	Radiation source	Ref.
1	DLIP patterning of S-HVOF TiO₂ sprayed coatings	0.12	10	1 μW/cm² @ 366 nm	Toma et al. 2021 <sup>[12]</sup>
2	P25	0.18	100	5.3 mW/cm <sup>2</sup> @ 360 nm	Zhang et al. 2001 <sup>[39]</sup>
3	P25 coated petri dish	0.25	1	Fluorescent lamp 900 mW/cm <sup>2</sup>	Bonetta et al. 2013 <sup>[40]</sup>
4	Anatase/Rutile hollow nanoparticles	0.35	62.5	solar radiation	Chaudhuri et al. 2014 <sup>[41]</sup>
5	Nanosized TiO <sub>2</sub> anatase	0.40	62.5	30 Lx	Dariani et al. 2016 <sup>[42]</sup>
6	DLIP Patterning of Titanium	0.67	50	Fluorescent lamp 36 W @ 365 nm	This work
7	TiO <sub>2</sub> and Au–TiO <sub>2</sub> composite films	0.78	11.6-16.3	60 μW/cm <sup>2</sup> @ 365 nm	Yogi et al. 2008 <sup>[43]</sup>
8	Cellulose/GO/ TiO <sub>2</sub> hydrogel	1.33	31	125 W Mercury lamp	Chen et al. 2020 <sup>[44]</sup>
9	P25	1.57	72	high pressure mercury lamp 125 W	Houas et al. 2001 <sup>[45]</sup>
10	TiO <sub>2</sub> anatase	0.71-4.61	12.5	11–132 $\mu$ W/cm <sup>2</sup>	Wu et al. 2006 <sup>[46]</sup>
11	TiO <sub>2</sub> nanoflowers	3	40	100 W lamp, 6.5 mW/cm <sup>2</sup>	Harris et al. 2020 <sup>[47]</sup>
12	rutile anatase film	4.08	500 (Urea)	200 W Xenon-Mercury lamp	Coto et al 2021 <sup>[5]</sup>
13	nanosize anatase/P25	1.75-4.17	9.3	100 W longwave mercury spot lamp	Won et al. 2018 <sup>[48]</sup>

most part employed stronger UV-sources and worked with nanoparticle solutions instead of patterned surfaces. In practice, nanoparticles come with a set of challenges. For water treatment they need to be removed from the processed solutions to be reused and to prevent their distribution in the environment while their use on surfaces requires additional coating steps that significantly reduce the active surface of the particles.

#### **Conclusions**

In this work, photocatalytically active surfaces were created by direct laser interference patterning of a titanium substrate for the first time. The activity of the resulting surfaces was evaluated using methylene blue degradation under 365 nm UV-A radiation. The results show that the oxide layers' topography and its chemistry can be modified by adjusting the accumulated laser fluence and the number of pulses by which this fluence is brought onto the surface. An increase in accumulated fluence leads to the formation of the more stable titanium oxides - rutile and anatase -, whereas lower accumulated fluences predominantly produced the metastable oxides TiO and Ti<sub>2</sub>O<sub>3</sub>. A smaller pulse energy - i.e., a higher pulse number - leads to a more porous oxide layer with a larger active surface for photocatalysis. Future research should investigate the spatial distribution of the oxidic phases within the oxide layer and the presence of amorphous phases in more detail to identify processing conditions with a favourable oxide heterostructure.

#### **Experimental Section/Methods**

#### Sample Preparation

Wire-cut electrical discharge machining (EDM) was used to cut  $5 \times 5$  mm samples out of a 1 mm thick titanium sheet (HMW Hanauer GmbH; 99.995 wt.%). The resulting samples were mirror-polished following a multi-step routine described in detail in a previous work. [49]

After cleaning the samples in ethanol, the laser patterning was performed using an Edgewave px picosecond laser with a pulse width of 12 ps, a wavelength of 532 nm, a repetition rate of 100 kHz and a maximum average power of 10 W. In direct laser interference patterning a single laser beam is split into coherent sub-beams that are then brought to interference on the sample surface. The resulting interference pattern depends only on the laser's wavelength, its polarization, and the angle between the beams while the general pattern type can be adjusted by the number of beams used. [50] Two beams are needed to create a line pattern while three or four beams can be used to produce point patterns. For the cross-like structures the samples were processed with a line pattern, rotated by 90° and processed with another line pattern.

The DLIP setup used in this work splits the main beam into four sub-beams using a diffractive optical element (DOE) as depicted in Figure 12. Behind the DOE, a prism is used to bring the beams on a parallel path before they pass the final lens and are overlapped within its focal length on the sample surface. The interference angle can be adapted by changing the distance between the prism and the DOE. At higher DEO/prism distance the beams will be more

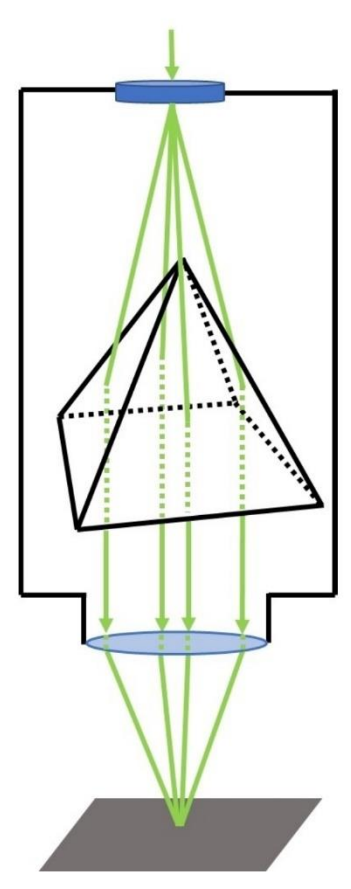


Figure 12. Simplified scheme of the DLIP optics head. The beam is first split into sub-beams, parallelized by a prism and then focused on the sample surface under an adjustable angle.

separated before being parallelized resulting in a higher interference angle and consequently a smaller DLIP periodicity *P* according to Eq. (2).

$$P = \frac{\lambda}{2\sin(\theta)} \tag{2}$$

The process parameters required to obtain the desired sample characteristics were calculated using a routine developed and reported in previous work. <sup>[49]</sup> While the line patterns were produced in a single process step with two beams, for the cross patterns two perpendicular line patterns each with half the total number of pulses were overlapped. The surfaces without an interference pattern were produced by blocking all but one beam and scanning the surface with a single beam. The samples were labeled using the following scheme (Table 3).

#### Methylene Blue Degradation

To determine the photocatalytic activity, the samples were placed in a sample holder where each sample was exposed to 125  $\mu$ L of 50  $\mu$ M methylene blue solution. UV-irradiation was performed using a commercially available UV-source ("Nailstar" model NS-01-UK&EU) employing four fluorescent lamps with a combined power of 36 W with a centered wavelength of 365 nm in a mirrored reaction chamber. During the experiment the sample holder was covered with a UV-transparent petri dish to minimize evaporation. After an initial waiting time of 30 minutes the samples were irradiated for a

wwnloaded from https://onlinelbrary.wiley.com/doi/10.1002/cmma.202300314 by Universitate Des Sarlandes, Wiley Online Library on [08/08/2023]. See the Terms and Conditions (thps://onlinelbrary.wiley.com/terms-and-conditions) on Wiley Online Library for rules of use; OA articles are governed by the applicable Creative Commons Licensus

Table 3. General la	belling scheme for the sample	s. The pattern type can be la	belled C for cross patterns, L for line pa	itterns and N for no pattern.
Parameter	Pattern type	Periodicity	Accumulated fluence	Number of pulses
Unit	-	μm	J/cm²	-
Example	C (Cross)	10	500	1650

Table 4. ICDD PDF numbers used for the XRD phase analysis.			
Phase ICDD PDF number			
$\alpha$ -Titanium	00-044-1294		
Rutil (TiO <sub>2</sub> )	01-079-5858		
Anatase (TiO <sub>2</sub> )	01-075-2545		
Tistarite (Ti <sub>2</sub> O <sub>3</sub>	04-005-4652		
Hongquiit (TiO)	04-004-2981		

total of 120 min. 90  $\mu L$  of solution were extracted after the experiment to determine the remaining MB concentration via UV-Vis spectroscopy. Between the experiment and the UV-Vis measurements the samples were stored for at least 24 hours. This was done in case any leuco-methylene blue that could distort the measurement formed during the experiment. The storage in ambient atmosphere ensures that any leuco-MB can oxidize back to MB so that the measurement only measures the irreversible degradation of MB. $^{[51]}$  The measurements were performed with a Lambda 750 spectrometer (Perkin Elmer Inc., Shelton, USA) equipped with a 100 mm integrating sphere. To determine the MB concentrations the sample solutions were filled in disposable cuvettes with a light path of 10 mm (UV-Cuvette micro, Band GmbH, Wertheim, Germany) and diluted with 160 µL of distilled water to achieve a sufficient sample volume. A cuvette with distilled water was used as a reference to subtract the solvent absorption. Measurements were performed at a wavelength of 664 nm and an integration time of 0.2 seconds. The concentration was then determined by comparing the resulting absorption with a calibration curve. Two to three replicates were performed per parameter.

#### **Surface Analysis**

#### SEM/FIB/EDS

Surface imaging was conducted using the secondary electron contrast of two SEM/FIB instruments (Thermo Fisher Helios G4 PFIB CXe and FEI Helios Nanolab600). The latter was also used to perform the FIB cross sectioning using a Ga ion source. The EDS measurements were performed with the PFIB (EDAX Octane Elite Super EDS detector and APEX v2 measurement and analysis software). An accelerating voltage of 5 kV was used for both, the SEM imaging and the EDS mappings. Secondary ion imaging was done using the proprietary ICE detector in the PFIB instrument.

#### X-Ray diffraction

Experiments were performed using a PANalytical X'Pert Pro MPD diffractometer and Copper  $K_a$  radiation using a Goebel mirror as incident beam optics. The measurements of the cross patterns were performed in a 2Theta range of 20–75° with a step size of 0.05° and a dwell time of 35 seconds. As the line patterns presented a better signal to noise ratio, they were performed with half the counting time. To restrict the information depth to the surface layer the measurements were performed in the grazing incidence mode with

an incidence angle of 0.8°. The patterns were oriented parallel to the incident beam to minimize shadowing of the pattern valleys. The ICDD codes of the powder diffraction files (PDF) used for phase analysis are given in Table 4.

#### **Acknowledgements**

The authors gratefully acknowledge funding in the ZuMat project, supported by the State of Saarland from the European Regional Development Fund (Europäischer Fonds für regionale Entwicklung, EFRE). Funding by the German Research Foundation (DFG) for both the PFIB/SEM instrument (INST 256/510-1 FUGG) and the picosecond DLIP machine (INST 256/470-1 FUGG) is greatly acknowledged. Funding for the PFIB/SEM instrument by German Research Foundation is greatly acknowledged (INST 256/510-1 FUGG). Francisco Cortés thanks the CUAA-DAHZ for the scholarship in the frame of the project I.DEAR-Materials (Project ID: D/14/07555). Pablo Delfino thanks the European Commission for the scholarship in the frame of the EMJMD AMASE (Project Nr. 619784). Open Access funding enabled and organized by Projekt DEAL.

#### **Conflict of Interests**

The authors declare no conflict of interest.

#### **Data Availability Statement**

The data that support the findings of this study are available from the corresponding author upon reasonable request.

**Keywords:** laser surface functionalization  $\cdot$  direct laser interference patterning (DLIP)  $\cdot$  photocatalytic materials  $\cdot$  titanium oxide  $\cdot$  methylene blue  $\cdot$  water purification  $\cdot$  pulsed laser ablation

- [1] S. McMichael, P. Fernández-Ibáñez, J. A. Byrne, Water 2021, 13, 1198.
- [2] H. Chouirfa, H. Bouloussa, V. Migonney, C. Falentin-Daudré, Acta Biomater. 2019, 83, 37.
- [3] J. Low, B. Cheng, J. Yu, Appl. Surf. Sci. 2017, 392, 658.
- [4] C. S. U. Demirel, C. N. Birben, M. Bekbolet, Chemosphere 2018, 211, 420.
- [5] M. Coto, S. C. Troughton, P. Knight, R. Joshi, R. Francis, R. V. Kumar, T. W. Clyne, Surf. Coat. Technol. 2021, 411, 127000.
- [6] S. G. Kumar, K. S. R. K. Rao, Appl. Surf. Sci. 2017, 391, 124.
- [7] H. M. Yadav, J. S. Kim, S. H. Pawar, Korean J. Chem. Eng. 2016, 33, 1989.
- [8] T. Kawahara, Y. Konishi, H. Tada, N. Tohge, J. Nishii, S. Ito, Angew. Chem. Int. Ed. 2002, 2, 2811.
- [9] A. Naldoni, M. Altomare, G. Zoppellaro, N. Liu, Š. Kment, R. Zbořil, P. Schmuki, ACS Catal. 2019, 9, 345.





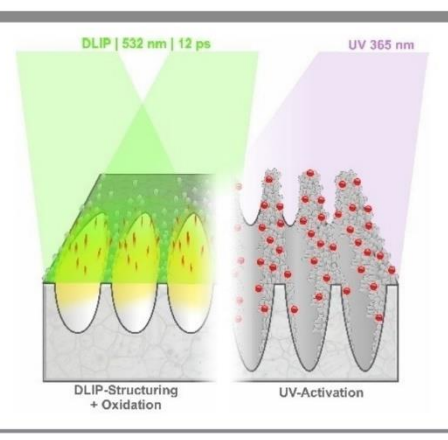
- [10] S. Jain, R. S. Williamson, M. Marquart, A. V. Janorkar, J. A. Griggs, M. D. Roach, J. Biomed. Mater. Res. Part B 2018, 106, 2284.
- [11] A. Das, M. Patra, R. R. Wary, P. Gupta, R. G. Nair, Conf. Ser.: Mater. Sci. Eng. 2018, 377, 012101.
- [12] F. L. Toma, S. Alamri, B. Leupolt, T. Kunze, M. Barbosa, J. Therm. Spray Technol. 2021, 30, 1159.
- [13] E. Westas, M. Hayashi, F. Cecchinato, A. Wennerberg, M. Andersson, R. Jimbo, J. R. Davies, J. Biomed. Mater. Res. Part A 2017, 105, 2321.
- [14] M. A. Henderson, Surf. Sci. Rep. 2011, 66, 185.
- [15] T. Křenek, L. Vála, T. Kovářík, R. Medlín, R. Fajgar, J. Pola, V. Jandová, V. Vavruňková, M. Pola, M. Koštejn, Dalton Trans. 2020, 49, 13262.
- [16] X. Y. Sun, F. J. Zhang, C. Kong, Colloids Surf. A 2020, 594, 124653.
- [17] X. Lang, S. Gopalan, W. Fu, S. Ramakrishna, Bull. Chem. Soc. Jpn. 2020, 94, 8.
- [18] W. Wang, R. Yang, T. Li, S. Komarneni, B. Liu, Composites Part B 2021, 205, 108512.
- [19] A. J. Antończak, Ł. Skowroński, M. Trzcinski, V. V. Kinzhybalo, Ł. K. Łazarek, K. M. Abramski, Appl. Surf. Sci. 2015, 325, 217.
- [20] A. Pérez Del Pino, P. Serra, J. L. Morenza, Appl. Surf. Sci. 2002, 197–198, 887.
- [21] T. Křenek, J. Pola, D. Docheva, T. Stich, R. Fajgar, T. Kovářík, M. Pola, J. Martan, D. Moskal, V. Jandová, J. Kupčík, P. Mikysek, Surf. Interfaces 2021, 26, 101304.
- [22] O. Van Overschelde, G. Guisbiers, M. Wautelet, J. Phys. Chem. C 2009, 113, 15343.
- [23] M. Qiao, J. Yan, L. Qu, B. Zhao, J. Yin, T. Cui, L. Jiang, ACS Appl. Mater. Interfaces 2020, 12, 41250.
- [24] E. C. Landis, K. C. Phillips, E. Mazur, C. M. Friend, J. Appl. Phys. 2012, 112, 2.
- [25] T. Nakajima, T. Tsuchiya, T. Kumagai, J. Solid State Chem. 2009, 182, 2560.
- [26] H. L. Ma, J. Y. Yang, Y. Dai, Y. B. Zhang, B. Lu, G. H. Ma, Appl. Surf. Sci. 2007, 253, 7497.
- [27] C. Florian, R. Wonneberger, A. Undisz, S. V. Kirner, K. Wasmuth, D. Spaltmann, J. Krüger, J. Bonse, Appl. Phys. A Mater. Sci. Process. 2020, 126. 1.
- [28] C. Zwahr, R. Helbig, C. Werner, A. F. Lasagni, Sci. Rep. 2019, 9, 1.
- [29] E. Verrelli, D. Tsoukalas, Solid-State Electron. 2014, 101, 95.
- [30] C. G. Levi, V. Jayaram, J. J. Valencia, R. Mehrabian, J. Mater. Res. 1988, 3, 969.
- [31] B. Xu, H. Y. Sohn, Y. Mohassab, Y. Lan, RSC Adv. 2016, 6, 79706.
- [32] S. Andersson, B. Collén, U. Kuylenstierna, A. Magnéli, *Acta Chem. Scand.* 1957, 11, 1641.

- [33] A. S. Bolokang, D. E. Motaung, C. J. Arendse, T. F. G. Muller, *Mater. Charact.* 2015, 100, 41.
- [34] C. N. Huang, J. S. Bow, Y. Zheng, S. Y. Chen, N. J. Ho, P. Shen, Nanoscale Res. Lett. 2010, 5, 972.
- [35] F. Schell, S. Alamri, A. Hariharan, A. Gebert, A. F. Lasagni, T. Kunze, Mater. Lett. 2022, 306, 130920.
- [36] L. Schweitzer, A. Cunha, T. Pereira, K. Mika, A. M. B. Do Rego, A. M. Ferraria, H. Kieburg, S. Geissler, E. Uhlmann, J. Schoon, *Materials* 2020, 13, 5342.
- [37] M. Xu, A. Zada, R. Yan, H. Li, N. Sun, Y. Qu, Phys. Chem. Chem. Phys. 2020, 22, 4526.
- [38] S. Mergenbayeva, T. S. Atabaev, S. G. Poulopoulos, Catalysts 2021, 11, 18.
- [39] T. Zhang, T. Oyama, A. Aoshima, H. Hidaka, J. Zhao, N. Serpone, J. Photochem. Photobiol. A 2001, 140, 163.
- [40] S. Bonetta, S. Bonetta, F. Motta, A. Strini, E. Carraro, AMB Express 2013, 3, 1.
- [41] R. Ghosh Chaudhuri, S. Paria, Dalton Trans. 2014, 43, 5526.
- [42] R. S. Dariani, A. Esmaeili, A. Mortezaali, S. Dehghanpour, Optik 2016, 127, 7143.
- [43] C. Yogi, K. Kojima, N. Wada, H. Tokumoto, T. Takai, T. Mizoguchi, H. Tamiaki, Thin Solid Films 2008, 516, 5881.
- [44] Y. Chen, Z. Xiang, D. Wang, J. Kang, H. Qi, RSC Adv. 2020, 10, 23936.
- [45] A. Houas, H. Lachheb, M. Ksibi, E. Elaloui, C. Guillard, J. M. Herrmann, Appl. Catal., B 2001, 31, 145.
- [46] C. H. Wu, J. M. Chern, Ind. Eng. Chem. Res. 2006, 45, 6450.
- [47] J. Harris, R. Silk, M. Smith, Y. Dong, W. Chen, I. N. Waterhouse, ACS Omega 2020, 5, 18919.
- [48] Y. Won, K. Schwartzenberg, K. A. Gray, Chemosphere 2018, 208, 899.
- [49] T. Fox, F. Mücklich, Adv. Eng. Mater. 2022, 25, 2201021.
- [50] A. F. Lasagni, C. Gachot, K. E. Trinh, M. Hand, A. Rosenkranz, T. Roch, S. Echhardt, T. Kunze, M. Bieda, D. Günther, V. Lang, F. Mücklich, Proc. SPIE 2017, 10092, 1009211.
- [51] A. Mills, Appl. Catal., B 2012, 128, 144.

Manuscript received: July 11, 2023 Revised manuscript received: July 13, 2023 Accepted manuscript online: July 14, 2023 Version of record online: ■■, ■■

#### **RESEARCH ARTICLE**

To maximize the photocatalytic activity of titanium dioxide, different titanium oxide phases need to be combined with a large surface area. Currently, this is mostly done using multistep processes involving nanoparticle synthesis and a coating process. In this work, highly active surfaces were produced in a single laser processing step and subsequently analyzed.



T. Fox\*, P. Maria Delfino, F. Cortés, Dr. C. Pauly, D. Wyn Müller, M. Briesenick, Prof. Dr. G. Kickelbick, Prof. Dr. F. Mücklich

1 - 13

Single-step Production of Photocatalytic Surfaces via Direct Laser Interference Patterning of Titanium

## Influence of heat treatments on the photocatalytic activity of TiO<sub>2</sub> surfaces produced by Direct Laser Interference Patterning

Tobias  $Fox^{I}$ ,  $Fabian Kay Bonner^{I}$ ,  $Christoph Pauly^{I}$ ,  $Guido Kickelbick^{2}$ ,  $Frank Mücklich^{I}$ 

Published "Advanced Materials Interfaces" 2025 (CiteScore 8.4 by 2023) https://doi.org/10.1002/admi.202400786

#### Abstract:

Direct Laser Interference Patterning (DLIP) has in previous work shown to be an effective tool for producing photocatalytic surfaces in a single relatively simple processing step. These surfaces could be interesting candidates for antifouling or self-cleaning surfaces, as well as substrates for photocatalytic water treatment. In this contribution, various heat treatments are performed both during and after the laser processing to create surfaces with even higher photocatalytic activities and to better understand the formation of various process oxides and their effect on the resulting activity. The photocatalytic activity of the samples is measured by methylene blue degradation and correlated to their chemical composition and morphology. Furthermore, a small prototype is built using low-cost materials to prove the scalability of the approach.

#### **Author Contributions**

Conceptualization: Lead; Formal analysis: Equal; Investigation: Equal; Methodology: Equal; Validation: Lead; Writing original draft: Lead; Writing - review & editing: Equal

<sup>&</sup>lt;sup>1</sup> Chair of Functional Materials, Department of Materials Science, Saarland University, 66123, Saarbrücken, Germany.

<sup>&</sup>lt;sup>2</sup> Inorganic Solid-State Chemistry, Department of Chemistry, Saarland University, 66123, Saarbrücken, Germany.



# Influence of Heat Treatments on the Photocatalytic Activity of TiO<sub>2</sub> Surfaces Produced by Direct Laser Interference Patterning

Tobias Fox,\* Fabian Kay Bonner, Christoph Pauly, Guido Kickelbick, and Frank Mücklich

Direct laser interference patterning (DLIP) has in previous work shown to be an effective tool for producing photocatalytic surfaces in a single relatively simple processing step. These surfaces can be interesting candidates for antifouling or self-cleaning surfaces, as well as substrates for photocatalytic water treatment. In this contribution, various heat treatments are performed both during and after the laser processing to create surfaces with even higher photocatalytic activities and to better understand the formation of various process oxides and their effect on the resulting activity. The photocatalytic activity of the samples is measured by methylene blue degradation and correlated to their chemical composition and morphology. Furthermore, a small prototype is built using low-cost materials to prove the scalability of the approach.

1. Introduction

Producing photocatalytic surfaces based on titanium and its oxides generally requires multi-step processes that require nanoparticle synthesis or wet chemical processing.<sup>[1-5]</sup> To facilitate the large-scale production of active surfaces, alternative processing routes like laser oxidation are becoming more prevalent.<sup>[6-12]</sup>

In previous work, it was shown that Direct Laser Interference Pattering (DLIP) can be used to produce photocatalytic surfaces in a single processing step through the creation of a suitable topography as well as the creation of photocatalytically active titanium oxides.<sup>[13]</sup> However, it was hypothesized that the activity

T. Fox, F. K. Bonner, C. Pauly, G. Kickelbick, F. Mücklich Functional Materials Saarland University 66123 Saarbrücken, Germany E-mail: tobias.fox@uni-saarland.de

T. Fox, F. K. Bonner, C. Pauly, G. Kickelbick, F. Mücklich Inorganic Solid-State Chemistry

Saarland University

Campus, Building C4 1, 66123 Saarbrücken, Germany

The ORCID identification number(s) for the author(s) of this article can be found under https://doi.org/10.1002/admi.202400786

© 2025 The Author(s). Advanced Materials Interfaces published by Wiley-VCH GmbH. This is an open access article under the terms of the Creative Commons Attribution License, which permits use, distribution and reproduction in any medium, provided the original work is properly cited.

DOI: 10.1002/admi.202400786

of these surfaces is diminished by a metastable TiO phase that forms during the pattering as well as possibly vast amounts of amorphous titanium oxides, both of which could potentially be removed via thermal activation. However, suitable heat treatment should not achieve temperatures high enough to transform the photocatalytically active, metastable TiO2 anatase phase in its less active rutile configuration. This study therefore investigates the effects of different heat treatments during and after the laser process on the oxide chemistry and morphology as well as the resulting photocatalytic activity. These treatments aim to increase the

activity of the surfaces as they allow the aforementioned more metastable phases to relax into more stable  ${\rm TiO_2}$  phases like rutile and anatase. Doing so could ideally increase the amount of anatase rutile heterojunctions, which would most likely have additional beneficial effects on the photocatalytic activity. [14–17]

Additionally, a prototype employing a patterned area of 80-200 mm and 1.5 L of methylene blue solution was built using easily available, low-cost materials to gain first insights regarding the scalability of the approach.

#### 2. Results and Discussion

#### 2.1. Surface Topography

Samples with periodic surface structures fabricated by DLIP can express hierarchical surface structures consisting of the actual DLIP pattern and a sub-structure. These sub-structures can be laser-induced periodic surface structures (LIPSS), remnants from the ablation process, or structures originating from the redeposition of material.[13,18-21] As expected from the results of previous work, the surfaces depicted in Figure 1 show a hierarchical structure where the material is ablated from the regions with maximal laser intensity, and a part of this material is then redeposited as oxide at the intensity minima of the applied interference pattern. This oxide layer has a porous substructure that depends on the pulse energy. For low pulse energies (L-samples) only small amounts of material are ablated per pulse. The ablated material then has time to oxidize and agglomerate at the interference minima. This leads to the formation of a complex, openpored oxide structure at those locations (Figure 1a,c). High pulse

2400786 (1 of 9)

 $\odot$  2025 The Author(s). Advanced Materials Interfaces published by Wiley-VCH GmbH

Adv. Mater. Interfaces 2025, 2400786

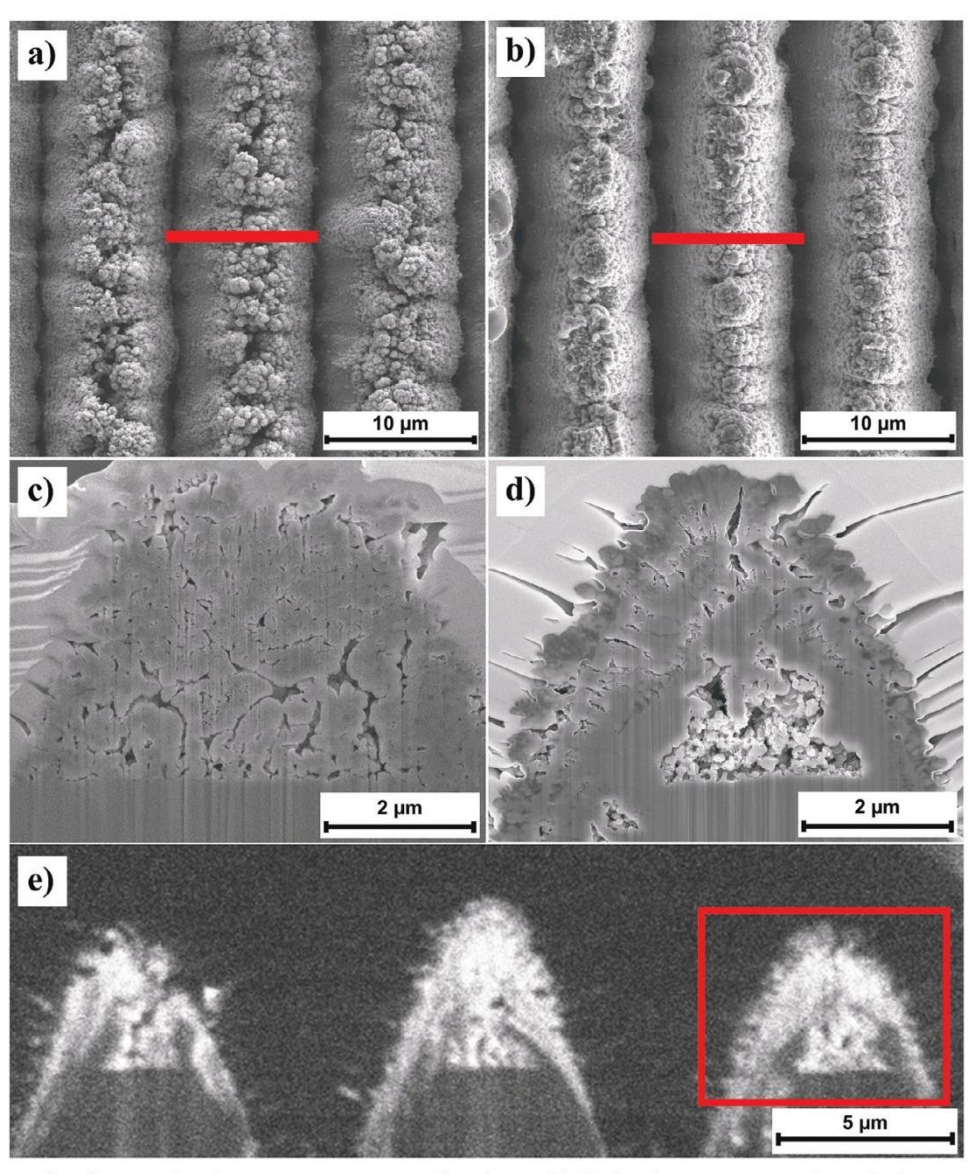


Figure 1. SEM images of surfaces produced at room temperature with a) low and b) high pulse energies together with close-ups of respective cross sections (c/d). e) Chemical contrast between titanium and oxide can be achieved by the secondary ion contrast using Xenon ions. The red markings in (a,b) indicate the approximate location of the respective cuts, whereas the red rectangle in e indicates the area depicted in (d).

energies (H-samples), on the other hand, produce molten material that forms a cone-shape on top of the maxima that is then covered with oxide (Figure 1b,d). Secondary ion imaging of the focused ion beam (FIB) cross-sections is applied and yields superior contrast between metal and oxide. The convolved mixture of metal and metal oxide on H-samples becomes visible (Figure 1e). The result of this formation process is a surface that rather shows large pores within the structure instead of an open "coral-like" oxide structure. In addition to this oxide structure, the surfaces produced at elevated temperatures show an extremely fine oxidic structure on top, as can be shown in Figure 2 depicting a sample produced with high pulse energy at 400 °C. The heat treatments after the patterning, on the other hand, had no visible effect on the observed porosity as the treatment temperature and time apparently were not sufficient to cause significant densification.

#### 2.2. Surface Chemistry

This section discusses the surface chemistry of the produced samples on the basis of X-ray diffraction (XRD) measurements. While respective measurements were performed for all samples, the observed trends are discussed using the most relevant diffractograms shown in **Figure 3**. These have been analyzed using Rietveld refinement to determine the relative phase concentrations that are presented in **Table 1**.

Generally speaking, a high anatase content is desirable as anatase is seen as the most photocatalytically active phase. A combination of anatase with rutile can further increase the activity as the combination of both phases facilitates charge separation and prevents recombination. [14,22,23] The oxygen-deficient phases hongquite and tistarite (TiO and  $\text{Ti}_2\text{O}_3$ ) have in former

2400786 (2 of 9)

© 2025 The Author(s). Advanced Materials Interfaces published by Wiley-VCH GmbH

is) on Wiley Online Library for rules of use; OA articles are governed by the applicable Creative C

21967350, 0, Downloaded from https://onlinelibrary.wiley.com/doi/10.1002/admi.202400786 by Tobias Fox

- Saarlaendische Universitaets- und Landesbibliothek Saarbrücken , Wiley Online Library on [09/01/2025]. See the Terms and Conditions (https://onlinelibrary.wiley.com/terms-and-conditions) on Wiley Online Library for rules of use; OA articles are governed by the applicable

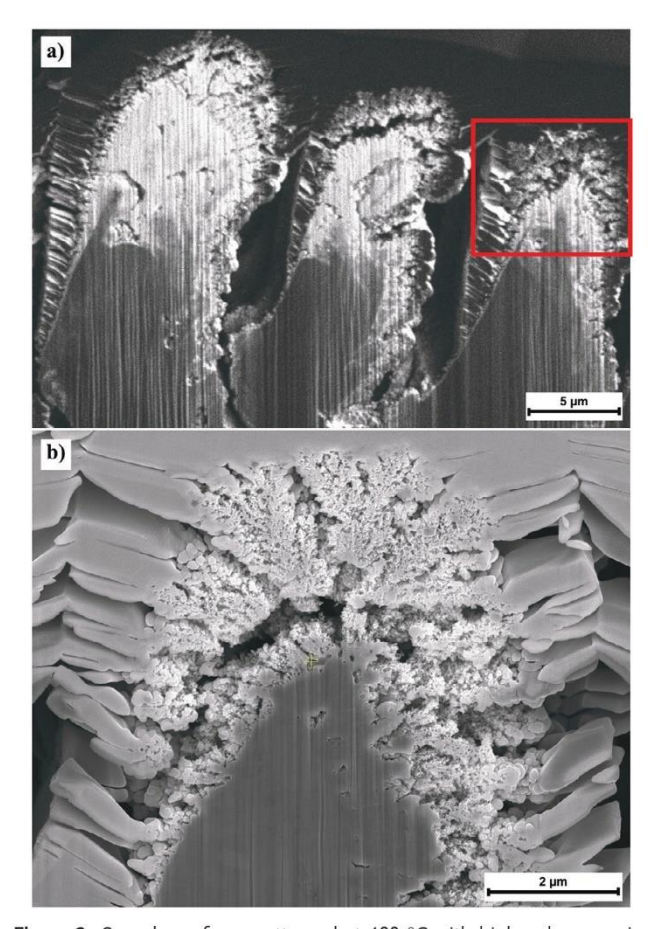


**Figure 2.** Sample surfaces patterned at 400 °C with high pulse energies showing vast amounts of oxide in the ion contrast overview a) and a very fine, porous oxide structure in the magnified SE image b) of the rightmost peak.

work shown to have a mostly negative impact on the photocatalytic activity.  $^{[13]}$ 

Although all samples were exposed to the same accumulated fluence it can be shown in Figure 3 and Table 1 that even the samples produced at room temperature show a significant difference in oxide composition depending on the applied pulse energy. While both sample sets show rutile and anatase the samples produced with high pulse energy show significantly more oxygendeficient oxides TiO and  $Ti_2O_3$ . This observation is in agreement

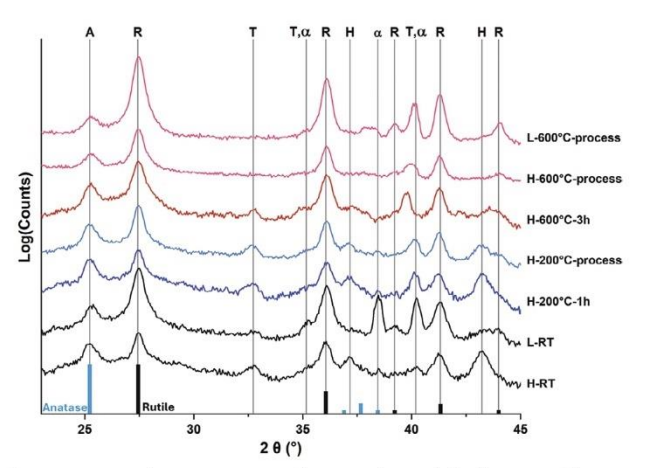


**Figure 3.** Exemplary XRD curves for samples with high (H) and low (L) pulse energies and different heat treatment temperatures and times. The observed peaks are indicated using the PDF files listed in Section 3.3.2 and labeled with the respective phases. A: Anatase; R: Rutile;  $\alpha$ :  $\alpha$ -Titanium; T: Tistarite (Ti<sub>2</sub>O<sub>3</sub>); H: Hongquite (TiO). At the bottom of the graph, the reference spectra for rutile and anatase are plotted with their respective intensities according to the PDF cards listed in the methods section.

with former work<sup>[13]</sup> and likely stems from the fact that more titanium is ablated per pulse at high pulse energies. As a result, the oxygen content in the resulting plasma is not sufficient to fully oxidize the material. It is additionally observed that for lower pulse energies the diffractograms show pronounced peaks of alpha titanium. However, as it was seen by scanning electron microscopy (SEM) that the surface of the peaks is covered in oxides, it is suggested that the lower pulse energies produce less oxide in the topographic troughs while the higher pulse energies produce a thin oxide layer even in these valleys. For the samples exposed to higher temperatures, a shift of the  $\alpha$ -Ti reflections toward lower angles can be observed. This shift can be explained by the incorporation of oxygen into the titanium lattice, whichaffects the lattice constant and the c/a ratio. [24,25]

Simultaneously the oxygen-deficient phases hongquite and tistarite (TiO and  $\rm Ti_2O_3$ ) partially disappear during the heat treatments. Especially the hongquite signal that was relatively strong at room temperature (H-RT in Figure 3) is greatly reduced when the sample is patterned at 200 °C. This reduction in signal implies that the heat treatment halved the amount of TiO from 22 mass% for the room temperature sample to 11 mass% for the sample patterned at 200 °C. For both laser treatments at 600 °C

**Table 1.** Phase concentrations in mass% determined from the XRD measurements shown in Figure 3 via Rietveld refinement. The error of the measurement is 1 mass% for all measurements.

Sample	TiO <sub>2</sub> [rutile]	TiO <sub>2</sub> [anatase]	Ti <sub>2</sub> O <sub>3</sub> [tistarite]	TiO [hongquite]	alpha-Ti
L-RT	79	14	0	4	3
H-RT	49	20	8	22	1
H-200°-1 h	47	23	10	18	2
H-200°-process	55	23	9	11	2
H-600°-3 h	66	21	3	8	2
H-600°-process	77	19	0	2	3
L-600°-process	88	7	0	2	2

2400786 (3 of 9)

ADVANCED MATERIALS INTERFACES

hongquite is barely visible. Tistarite behaves similarly, although in contrast to honquite some amount of tistarite appears to be remaining in the sample heat treated at 600 °C after the patterning.

When regarding the left side of the diffractograms, the anatase and rutile peaks can clearly be distinguished. For the room temperature samples, the area below the peaks also indicates the presence of a significant amount of amorphous phase as is to be expected with regard to the high cooling rates that result during the redeposition process. Anatase has a higher Gibbs energy than rutile at all temperatures and therefore generally exists as a metastable phase and will transform into rutile at pprox600 °C although observations vary from 400 to 1200 °C. Anatase is however more stable than rutile at particle sizes below 40 nm as it possesses a smaller surface energy. As a result, the redeposited material that is partially amorphous or has very small grain sizes likely is the main source of anatase on the surface. At elevated temperatures, the amorphous material appears to gradually transform into rutile. Even at 600 °C some anatase still remains both in the sample heated after the laser patterning and the sample that was patterned at 600 °C. Particularly the fact that the sample patterned at 600 °C still shows anatase indicates that very small grains of anatase are formed during the process and did not have the time to grow and transform into rutile.[26-29]

It must be noted though, that the information depth of the XRD measurements is limited to  $\approx\!125$  nm as a result of the small angle of incidence of  $0.8^{\circ}$  when assuming the absorption characteristics of rutile. This means that the oxide composition below the surface cannot be assessed by these measurements. The different holding times did not cause visible differences in the resulting spectra for any of the samples, which is why they were not plotted in Figure 3.

#### 2.3. Photocatalytic Activity

Methylene Blue (MB) degradation experiments were performed as described in Section 3.3.3. After the experiment, the remaining concentrations were measured via UV–vis spectroscopy (Section 3.3.4) and compared to the initial concentration  $C_0$  (50  $\mu$ m). As previous work. [13] could already show stable cycling stability for similar surfaces, this work did not investigate multiple degradation cycles.

Figure 4 depicts the results of the degradation experiments for samples that were heat-treated after the patterning. For two reference measurements, one containing only the methylene blue solution without any sample and one including untreated titanium, the methylene blue concentrations remained unchanged  $(C/C_0 = 1)$ , which is why they were not plotted here. For the two outliers at 200 °C-1h-H and 200 °C-3h-L, it was observed after the experiment that air bubbles had remained at the sample surfaces, which likely resulted in a decreased activity. In a small-scale repetition of the experiment, 200 °C-3h-L showed an activity similar to the other L samples. Overall, it could be observed that all heat treatments improved the activity of the surface and there is no significant difference between different pulse energies. This is consistent with former experiments without heat treatments.<sup>[13]</sup> It can additionally be observed that all but the 200 °C-1 h treatment resulted in a major increase in photocatalytic activity. This increased performance can likely be attributed to an increase in

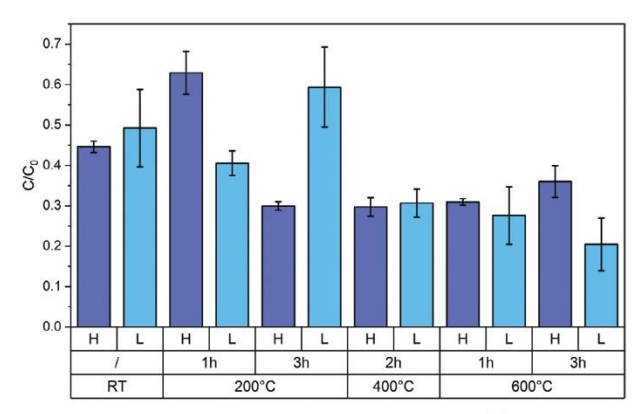


**Figure 4.** Remaining MB concentrations as measured by UV–vis spectroscopy. The methylene blue concentration after the experiment was divided by the initial concentration  $C_0$  to determine a percentual decrease for various heat-treated samples and the laser patterned reference that remained at room temperature (RT). H and L indicate high and low pulse energies.

crystallinity as amorphous oxides crystallize and the peak for rutile becomes more pronounced. [30] Even though the pulse energy influences both the surface topography and chemistry (mainly by producing more TiO at higher pulse energies), it tends to have only a small impact on the photocatalytic activity. This is especially true after the heat treatment where the oxygen-deficient phases crystallize to form rutile. Overall, this crystallization can be assumed to be the main cause of the increase in activity for the heat-treated samples as the presence of oxygen-deficient phases has in a former study shown to decrease the activity of the surface. [13]

The results of the experiments employing the heat treatment during the patterning process are shown in **Figure 5**. To assess the effect of the heat treatment in air without patterning, an unpatterned reference was produced for each temperature. Especially the reference at 400 °C showed a minor photocatalytic activity that is consistent with the results of a former study that observed a mixture of anatase and rutile in samples produced at 450 °C.<sup>[31]</sup> As these results show, an increase in temperature to

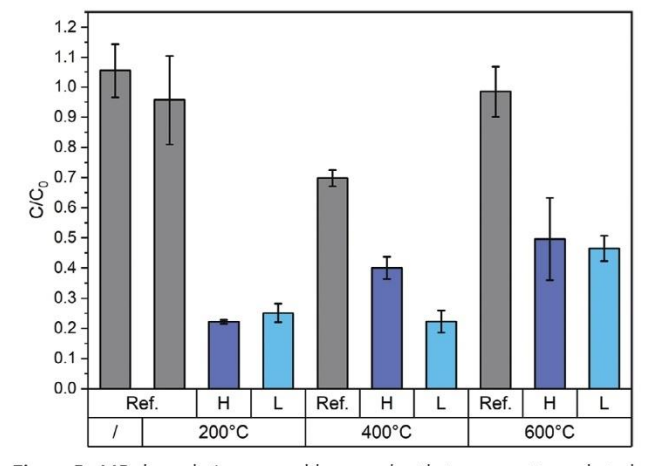


**Figure 5.** MB degradation caused by samples that were patterned at elevated temperatures.

2400786 (4 of 9)

Table 2. Kinetic constants for all patterned samples.

Processing temperature [°C]	Heat-treatment temperature [°C]	Heat-treatment time [h]	Pulse energy	Kinetic constant [1/h]
RT	200	1	Н	0.23 ± 0.04
			L	$0.45 \pm 0.04$
		3	Н	$0.60 \pm 0.02$
			L	$0.27 \pm 0.09$
	400	2	Н	$0.61 \pm 0.04$
			L	$0.59 \pm 0.06$
	600	1	Н	$0.59 \pm 0.01$
			L	$0.66 \pm 0.12$
		3	Н	$0.51 \pm 0.02$
			L,	$0.83 \pm 0.09$
		_	Н	$0.40 \pm 0.02$
			L	$0.36 \pm 0.09$
200		_	Н	$0.75 \pm 0.01$
			L	$0.69 \pm 0.06$
400		_	Н	$0.46 \pm 0.05$
			Ĺ	$0.76 \pm 0.08$
600		_	Н	$0.37 \pm 0.13$
			L	$0.38 \pm 0.04$

only 200 °C during the laser patterning was enough to achieve very high activities. In fact, the first-order kinetic constant of the sample produced with a high pulse energy at 200 °C is with 0.75 1/h one of the three highest of the whole study, as can be seen in **Table 2**. This correlates well with the observed anatase content of 23% (Table 1), which was one of the highest observed in this study.

As mentioned above, the increase in photocatalytic activity is most likely a result of increased crystallinity and a lower content of TiO. As amorphous  ${\rm TiO}_2$  is generally considered inactive, its presence can reduce the activity of the surface, and its crystallization into anatase is very beneficial. However, rutile is thermodynamically more stable than anatase except for nanostructured grains (<40 nm) where anatase's smaller surface energy stabilizes the phase. $^{[26-28,32]}$  As a result, an effective heat treatment needs to deliver sufficient activation energy for the nucleation of amorphous  ${\rm TiO}_2$  and the transformation of  ${\rm TiO}$  into pure  ${\rm Ti}$  and  ${\rm TiO}_2$  without resulting in crystal growth and the formation of rutile

Additional synergistic effects can be expected if anatase and either rutile or  ${\rm Ti_2O_3}$  are present in the surface, and if an electrically conductive connection (heterojunction) between those phases exists. This is because such heterojunctions can facilitate charge separation and thereby decrease the probability that charge carriers recombine right after their formation. [32–39]

As some of the heat treatments performed in this work resulted in major increases in photocatalytic activity without a vast increase in anatase content (Figure 3), it can be assumed that the increase in activity is a result of an increased charge carrier mobility and the formation of heterojunctions. To validate this hypothesis, Transmission Electron Microscopy (TEM) analysis was attempted. However, as a result of the complex surface topogra-

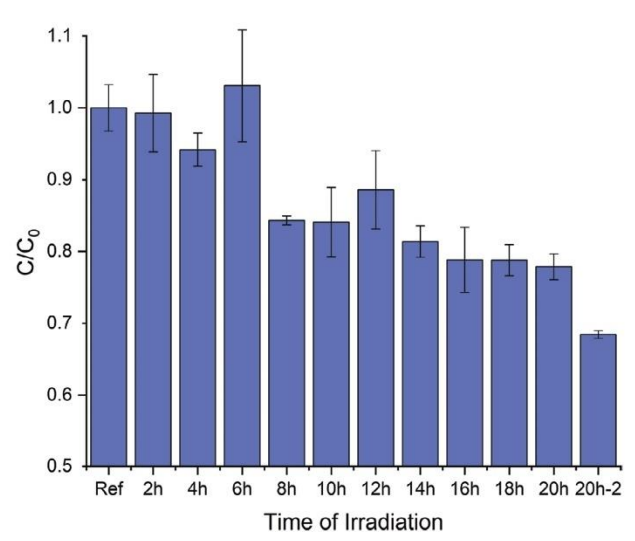


**Figure 6.** Methylene blue degradation achieved by the prototype. The measurement labeled as 20h-2 was performed after the evaporation of 200 mL was compensated.

phy, the preparation of sufficiently thin TEM lamella without the loss of the porous surface oxides still proved challenging by the time of publication. Future research will follow up on this question.

#### 2.4. Upscaling of the Approach

In order to gain insights regarding the scalability of the approach, laser patterning was performed on an  $80 \times 200$  mm area and tested with 1.5 liters of methylene blue solution using a 30 W UV lamp. The setup is explained in greater detail in Section 3.4.

Samples of the methylene blue solution were retrieved in intervals of 2 h of UV irradiation. By the end of the experiment, 200 mL of water had evaporated and were replaced. Therefore, two data points exist for 20 h of irradiation, one before and one after the evaporation was compensated. The resulting degradation is shown in Figure 6. It can be seen that the concentration is continuously reduced with increasing irradiation time. After evaporation was compensated by adding water it was revealed that the concentration of the methylene blue solution had been reduced by  $\approx\!30\%$ .

To try and compare the performance of the prototype with that of the lab setup the number of degraded molecules per hour, watt, and cm² was calculated for both setups using the k values of the RT-H sample from Table 2 and the 20h-2 sample from Figure 6. Although the setups are vastly different, one employing a mirrored chamber and UV lamps, the other using an LED source and a vastly different scale, accounting for the active surface, exposure time, and UV power should show if both setups achieve comparable degradation rates. The result of this comparison is shown in Table 3. The time constant k is much smaller for the prototype than for the lab setup that can be explained by the smaller surface-to-volume fraction of the prototype given the large sample volume of 1.5 L. When comparing the actual normed degradation speeds of both setups it becomes apparent that both achieve similar efficiencies with the prototype having a slightly better

2400786 (5 of 9)

und Landesbibliothek Saarbrücken , Wiley Online Library on [09/01/2025]. See the Terms and Conditions (https://onlinelibrary.wiley.com/term

conditions) on Wiley Online Library for rules of use; OA articles are governed by the applicable Creative Commons

Table 3. Comparing the prototype to the normal lab setup discussed be-

	Lab setup	Prototype
MB Solution [μL]	125	$1.5 \times 10^{6}$
Active Area [cm <sup>2</sup> ]	0.25	160
UV-Power [W]	32	30
k [1/h]	$0.4 \pm 0.015$	$0.019 \pm 0.002$
С <sub>0</sub> [µм]	$50 \pm 4.37$	$50 \pm 0.93$
Amount of MB [nMol]	6.25 ± 0.546	75 000 ± 1.395
Degradation Efficiency nMol/(cm <sup>2</sup> *W*h)	$0.216 \pm 0.019$	0.247 ± 0.006

performance. This increased performance can be attributed to the higher efficiency of the employed LED light source for the prototype compared to the efficiency of the lamps employed in the lab setup. Another factor could be the larger overall reduction of methylene blue for the lab setup, which could lead to a depletion of MB that results in a smaller degradation speed toward the end of the experiment. This effect could be amplified as the prototype employed a continuous flow of solution that ensured an even distribution of MB over the surface without the formation of diffusion-limited depletion zones.

#### 3. Experimental Section

#### 3.1. Sample Preparation

The titanium samples used in this work were mirror-polished with a multi-step polishing routine described in previous work.[40] Before the laser patterning the samples were cleaned using water and soap.

The pattering was performed with an edgewave px picosecond laser with 532 nm wavelength, a pulse duration of 12 ps, a maximum repetition rate of 100 kHz, and a maximum average power of 10 W. The optical setup used to split the primary beam into multiple sub-beams and then interfere with those beams on the sample surface was described in detail in a former study.[13]

For the patterning, two different pulse energies namely 10 and 30.7 µJ were used. The resulting spot diameters of 94.7 and 113.5  $\mu m$  resulted in pulse fluences of 0.143 and 0.309 J cm<sup>-2</sup> respectively. These sample sets were therefore labeled as low pulse energy (L) and high pulse energy (H). The overlap between pulses was varied by employing pulse distances of 0.134 and 0.409 μm. Thereby the total number of pulses on a given point in the surface was set to be 5250 for the low pulse energy and 2475 for the high one. This scanning procedure achieved an accumulated fluence of 750 J cm<sup>-2</sup> for both sample sets, which was desired to ensure comparability of both sets. The values were calculated using the calculation routine developed in.[40]

#### 3.2. Heat Treatment

The heat treatment after the patterning was conducted in an oven equipped with a vacuum tube  $(9.0 \times 10^{-5} \text{ to } 4.6 \times 10^{-5} \text{ mbar})$  to

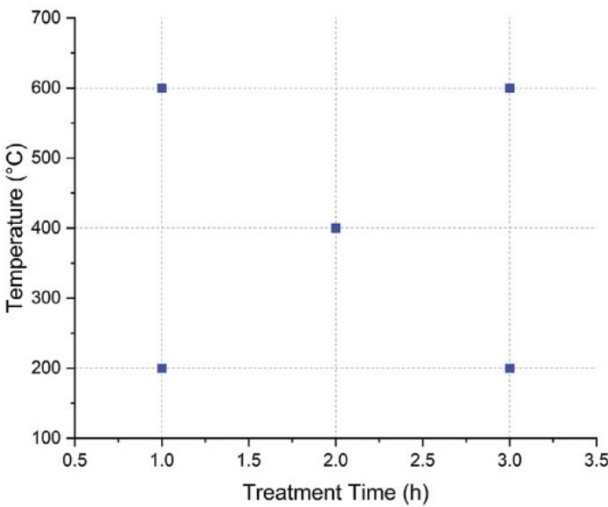


Figure 7. Parameter matrix for the heat treatments after the laser pattern-

ensure that the existing metastable oxides can relax into more stable phases without the formation of additional oxides. The minimum and maximum temperatures were chosen as 200 and 600 °C and the holding times as 1 and 3 h. Additionally, a center point was chosen at 400 °C and 2 h. The heating and cooling rate was set as 1 °C min-1. The experiment matrix is depicted in Figure 7. The maximum temperature of 600 °C was chosen because the literature reports the formation of pure rutile at higher temperatures (e.g., 750 °C by Barbour et al.[1]). In 2016 Wang et al.[31] have shown that a 6 h heat treatment at 450 °C produces a mixture of rutile and anatase in the surface. It should be noted that these studies were performed in oxygen-rich atmospheres. The experiments in this work however aim not to create additional oxide but only to transform existing metastable phases. As these processes were expected to require less diffusion than the formation of a thick oxidic film on the surface, the treatment times were varied on a shorter time scale.

For the heat treatment during the patterning, the samples were placed on a heating plate made of stainless steel that was equipped with two 200 W heating elements. The samples were placed on this plate before it was heated with a heating rate of 5 °C min<sup>-1</sup>. The patterning was started 5 min after the target temperature was reached.

#### 3.3. Surface Analysis

#### 3.3.1. SEM/FIB/EDS

FIB cross-sectioning and SEM imaging were performed using both a Ga-FIB/SEM (FEI Helios Nanolab600) and one employing a xenon ion source (Thermo Fisher Helios G4 PFIB). Secondary electron imaging was done at an acceleration voltage of 5 kV. Secondary ion imaging was done using the xenon ion beam at 30 kV and the proprietary ICE detector.

2400786 (6 of 9)



 Table 4. Crystallographic references used for the evaluation of the XRD

Phase	ICDD-Reference Code	
α-Titanium (Ti)	00-044-1294	
Rutile (TiO <sub>2</sub> )	01-079-5858	
Anatase (TiO <sub>2</sub> )	01-075-2545	
Tistarite (Ti <sub>2</sub> O <sub>3</sub> )	04-005-4652	
Hongquiite (TiO)	04-004-2981	

#### 3.3.2. X-Ray Diffraction

The grazing incidence XRD measurements were performed using Copper K $\alpha$  radiation in a diffractometer equipped with a Goebel mirror (PANalytical X'Pert Pro MPD). The 2Theta range was  $20^{\circ}-75^{\circ}$  with a step size of  $0.05^{\circ}$ , an incidence angle of  $0.8^{\circ}$ , and a dwell time of 35 s per step. For the measurements, the orientation of the pattern was adjusted to be parallel to the incoming beam to minimize shadowing effects. The powder diffraction files that were used for the analysis are given in **Table 4**.

Rietfeld<sup>[41,42]</sup> refinement was performed using the analysis software TOPAS from Bruker.<sup>[43]</sup> The respective crystallographic data were sourced from the Pearson-Database.<sup>[44]</sup>

#### 3.3.3. Methylene Blue Degradation

To quantify the photocatalytic activity of the surfaces, three individual 5  $\times$  5 mm samples for each parameter were placed in glass vials and brought in contact with 125  $\mu L$  of a 50  $\mu M$  methylene blue (MB) solution. The vials were then randomly placed in a holder and covered with a UV-transparent PMMA cover to minimize evaporation. The holder was then placed in a commercially available UV source (Naistar NS 01 UK&EU) employing four 8 W fluorescence lamps with a central wavelength of 365 nm. After an irradiation time of 2 h 90  $\mu L$  of the solution was retrieved to determine the remaining MB concentration via UV–vis spectroscopy. For this, the 90  $\mu L$  samples were diluted with 160  $\mu L$  of distilled water to achieve a sample volume of 250  $\mu L$ .

These samples were placed in a Perkin Elmer Lambda 750 spectrometer where their absorption was measured in a wavelength range from 600 to 700 nm with a 4 nm step size. The optical path of the used cuvette was 10 mm. The concentration was determined by comparing the sample's absorption at 664 nm with a calibration curve. To plot the results the remaining concentration was normalized with the initial concentration. The fraction  $C/C_0$  therefore indicates the amount of MB left in the solution after two h of irradiation. The first-order kinetic constant was calculated using Equation (1):

$$k = \frac{1}{t} \times \ln\left(\frac{C_0}{C}\right) \tag{1}$$

#### 3.4. Preparation of the Prototype

To produce a prototype on a larger scale, a commercially available grade 1 titanium foil with 0.1 mm thickness was bought from



**Figure 8.** Prototype for the upscaled degradation experiment consisting of a plastic container, a pump, the patterned foil, and a UV source. The methylene blue solution circulated by a small pump located underneath the nozzle on the right and flows over the patterned foil. The UV source in the background is placed on top of the UV-transparent lid of the box.

Evek GmbH via a German supermarket chain (Kaufland Stiftung & Co. KG). After cleaning with ethanol, the foil was placed in a customized sample holder and laser patterned without any prior surface treatment. To keep it as simple as possible, the patterning was performed at room temperature with the high pulse energy setting. A total area of  $200 \times 80$  mm was patterned.

To remove any loose oxide particles the sample was washed with deionized water and then placed in a polymer container as depicted in **Figure 8**. To circulate the methylene blue solution a small pump was placed under the sample holder and the nozzle was fixed near the top end of the foil. As a UV source, a generic 30 W LED lamp with a center wavelength of 365 nm was bought from Amazon marketplace. To start the experiment 1.5 L of 50  $\mu \rm M$  methylene blue solution was added, the pump was switched on, the lid of the box was closed, and the UV lamp was placed on the UV-transparent lid.

Before starting both the lamp and the timer, the setup was left to run in the dark for 30 min. Afterward, the first sample was withdrawn to mark the initial concentration. Additional samples were withdrawn every 2 h. Every time, three samples of 90  $\mu$ L were withdrawn to ensure that the subsequent measurement parameters for the UV–vis were identical to those of the previous measurements. After every withdrawal, the setup was left for several minutes to let the UV lamp cool down. After 20 h of UV exposure, a total of 200 mL of water had evaporated and was replaced after which another sample (20 h-2) was retrieved.

#### 4. Conclusion

It could be shown that heat treatments after and during laser processing can improve the photocatalytic activity of the resulting surfaces. Especially the laser treatment at 200 °C appears to be a feasible approach when producing photocatalytic surfaces at a larger scale without adding a second processing step. It could further be shown that the increase in activity mainly stems from the transition of amorphous and oxygen-deficient phases (especially TiO) into crystalline anatase and rutile phases. It is further hypothesized that a large number of heterojunctions between those phases exist, which could further explain the increase in

2400786 (7 of 9)

www.advancedsciencenews.com



www.advmatinterfaces.de

reactivity. Finally, one of the patterns was chosen for a larger-scale prototype employing everyday materials. The prototype achieved a degradation efficiency of 0.25 mMol per hour, cm², and watt of UV irradiation. Given that this laser treatment can be applied on large surfaces relatively easily, this approach could facilitate wastewater treatment using sunlight and respective photoreactors.

#### Acknowledgements

The authors gratefully acknowledge funding for the ZuMat project, supported by the State of Saarland from the European Regional Development Fund (Europäischer Fonds für regionale Entwicklung, EFRE). Funding by the German Research Foundation (DFG) for both the PFIB/SEM instrument (INST 256/510-1 FUGG) and the picosecond DLIP machine (INST 256/470-1 FUGG) is greatly acknowledged. Technical assistance for this work was provided by the Service Center X-ray Diffraction, with financial support from Saarland University and the German Science Foundation (project number INST 256/349-1). The authors thank Dr. Oliver Janka for the support in the interpretation of the X-ray diffraction data presented in this paper. Special thanks go to Bruno Alderete for proofreading and providing language corrections.

#### **Conflict of Interest**

The authors declare no conflict of interest.

#### **Data Availability Statement**

The data that support the findings of this study are available from the corresponding author upon reasonable request.

#### **Keywords**

direct laser interference patterning (DLIP), heat treatment, laser surface functionalization, photocatalytic materials, pulsed laser ablation, titanium oxide, water purification

Received: October 1, 2024 Revised: December 19, 2024 Published online:

- T. Křenek, J. Pola, D. Docheva, T. Stich, R. Fajgar, T. Kovářík, M. Pola, J. Martan, D. Moskal, V. Jandová, J. Kupčík, P. Mikysek, Surf. Interfaces 2021, 26, 101304.
- [2] S. Obregón, V. Rodríguez-González, J. Sol-Gel Sci. Technol. 2022, 102, 125.
- [3] X. Lang, S. Gopalan, W. Fu, S. Ramakrishna, Bull. Chem. Soc. Jpn. 2020, 94, 8.
- [4] T. Gupta, J. C. Samriti, J. Prakash, Mater. Today Chem. 2021, 20, 100428.
- [5] S. Dey, S. C. Roy, Nano Express 2021, 2, 010028.

Adv. Mater. Interfaces 2025, 2400786

- [6] P. Fathi-Hafshejani, H. Johnson, Z. Ahmadi, M. Roach, N. Shamsaei, M. Mahjouri-Samani, J. Laser Appl. 2021, 33, 012014.
- [7] M. Mahjouri-Samani, P. Fathi-Hafshejani, H. Johnson, Z. Ahmadi, M. Roach, N. Shamsaei, ACS Omega 2020, 5, 16744.

- [8] A. Medvids, P. Onufrijevs, J. Kaupužs, R. Eglitis, J. Padgurskas, A. Zunda, H. Mimura, I. Skadins, S. Varnagiris, Opt. Laser Technol. 2021, 138, 106898.
- [9] L. Grase, P. Onufrijevs, D. Rezevska, K. Racenis, I. Skadins, J. Karosas, P. Gecys, M. Iesalnieks, A. Pludons, J. Kroica, G. Raciukaitis, *Nanomaterials* 2023, 13, 2032.
- [10] A. Białous, M. Gazda, K. Grochowska, P. Atanasov, A. Dikovska, N. Nedyalkov, J. Reszczyńska, A. Zaleska-Medynska, G. liwiński, *Thin Solid Films* 2016, 601, 41.
- [11] M. Tošić, V. Rajić, D. Pjević, S. Stojadinović, N. Krstulović, S. Dimitrijević-Branković, M. Momčilović, *Photonics* 2024, 11, 284.
- [12] A. Barylyak, R. Wojnarowska-Nowak, M. Kus-Liśkiewicz, P. Krzemiński, D. Płoch, B. Cieniek, Y. Bobitski, J. Kisała, Sci. Rep. 2024, 14, 20926.
- [13] T. Fox, P. Maria Delfino, F. Cortés, C. Pauly, D. W. Müller, M. Briesenick, G. Kickelbick, F. Mücklich, ChemNanoMat 2023, 9, 202300314
- [14] J. Low, B. Cheng, J. Yu, Appl. Surf. Sci. 2017, 392, 658.
- [15] T. Kawahara, T. Ozawa, M. Iwasaki, H. Tada, S. Ito, J. Colloid Interface Sci. 2003, 267, 377.
- [16] Y. Gao, J. Zhu, H. An, P. Yan, B. Huang, R. Chen, F. Fan, C. Li, J. Phys. Chem. Lett. 2017, 8, 1419.
- [17] M. Qiao, J. Yan, L. Qu, B. Zhao, J. Yin, T. Cui, L. Jiang, ACS Appl. Mater. Interfaces. 2020, 12, 41250.
- [18] C. Zwahr, A. Welle, T. Weingärtner, C. Heinemann, B. Kruppke, N. Gulow, M. große Holthaus, A. Fabián Lasagni, Adv. Eng. Mater. 2019, 21, 1900639.
- [19] D. W. Müller, T. Fox, P. G. Grützmacher, S. Suarez, Sci. Rep. 2020, 10, 3647.
- [20] C. Schäfer, P. M. Delfino, P. Leonhard-Trautmann, V. Ott, S. Suarez, M. Stüber, F. Mücklich, C. Pauly, Adv. Eng. Mater. 2024, 2400435, https://doi.org/10.1002/adem.202400435.
- [21] S. Marie Lößlein, R. Merz, Y. Rodríguez-Martínez, F. Schäfer, P. G. Grützmacher, D. Horwat, M. Kopnarski, F. Mücklich, J. Colloid Interface Sci. 2024, 670, 658.
- [22] M. Gao, L. Zhu, W. L. Ong, J. Wang, G. W. Ho, Catal. Sci. Technol. 2015, 5, 4703.
- [23] S. G. Kumar, K. S. R. K. Rao, Appl. Surf. Sci. 2017, 391, 124.
- [24] S. Andersson, B. Collén, U. Kuylenstierna, A. Magnéli, Acta Chem. Scand. 1957, 11, 1641.
- [25] H. Okamoto, J. Phase Equilib. Diffus. 2011, 32, 473.
- [26] S. J. Smith, R. Stevens, S. Liu, G. Li, A. Navrotsky, J. Boerio-Goates, B. F. Woodfield, Am. Mineral. 2009, 94, 236.
- [27] O. Van Overschelde, G. Guisbiers, M. Wautelet, J. Phys. Chem. C 2009, 113, 15343.
- [28] D. A. H. Hanaor, C. C. Sorrell, J. Mater. Sci. 2010, 46, 855.
- [29] Y. Li, T. Ishigaki, J. Cryst. Growth 2002, 242, 511.
- [30] P. W. Chou, Y. S. Wang, C. C. Lin, Y. J. Chen, C. L. Cheng, M. S. Wong, Surf. Coat. Technol. 2009, 204, 834.
- [31] G. Wang, J. Li, K. Lv, W. Zhang, X. Ding, G. Yang, X. Liu, X. Jiang, Sci. Rep. 2016, 6, 31769.
- [32] V. Etacheri, C. Di Valentin, J. Schneider, D. Bahnemann, S. C. Pillai, J. Photochem. Photobiol., C 2015, 25, 1.
- [33] D. K. Sharma, S. Shukla, K. K. Sharma, V. Kumar, *Mater. Today Proc.* 2020, 49, 3028.
- [34] A. Das, M. Patra, R. R. Wary, P. Gupta, R. G. Nair, Conf. Ser.: Mater. Sci. Eng. 2018, 377, 012101.
- [35] G. Zerjav, K. Zizek, J. Zavasnik, A. Pintar, J. Environ. Chem. Eng. 2022, 10, 107722.
- [36] H. Liu, W. Yang, Y. Ma, J. Yao, Appl. Catal., A 2006, 299, 218.
- [37] T. Hu, P. Feng, L. Guo, H. Chu, F. Liu, Nanomaterials 2023, 13, 2125.

2400786 (8 of 9)

www.advancedsciencenews.com



www.advmatinterfaces.de

- [38] S. Mergenbayeva, T. S. Atabaev, S. G. Poulopoulos, *Catalysts* **2021**, *11*, 18.
- [39] H. Zhang, B. Zhang, X. Wang, L. Zou, J. You, S. Lin, Sust. Energy Fuels. 2024, 8, 2357.
- [40] T. Fox, F. Mücklich, Adv. Eng. Mater. 2022, 25, 2201021.
- [41] H. M. Rietfeld, Acta Crystallogr. 1967, 22, 151.

- [42] H. M. Rietfeld, J. Appl. Cryst. 1969, 2, 65.
- [43] Topas, Version 5, Bruker AXS Inc, Karlsruhe, Germany 2014.
- [44] P. Villars, K. Cenzual, Pearson's Crystal Data: Crystal Structure Database for Inorganic Compounds, ASM International, Materials Park, OH, USA 2023.

Adv. Mater. Interfaces 2025, 2400786

21967350, 0, Downloaded from https://online.library.wiley.com/doi/10.1002/admi.202.400786 by Tobias Fox - Saardaendische Universitaets- und Landesbibliothek Saarbtocken, Wiley Online Library for rules of use, O; A articles are governed by the applicable Creiter Commons Licinsus, on [09:01-2025]. See the Terms and Conditions (https://online.library.wiley.com/rem--sad-conditions) on Wiley Online Library for rules of use, O; A articles are governed by the applicable Creiter Commons Licinsus, on [09:01-2025]. See the Terms and Conditions (https://online.library.wiley.com/rem--sad-conditions) on Wiley Online Library for rules of use, O; A articles are governed by the publicable Creiter Commons Licinsus, on [09:01-2025].

# **6 Unpublished Results**

Over the course of this thesis, a variety of scientific results have been produced that have not been published (yet). Especially the analysis of the oxidic surfaces produced in this thesis via TEM was suggested by multiple reviewers and attempted many times. It is therefore not for a lack of trying that the publications presented in this thesis do not include TEM results and this section will briefly discuss the attempts that were made in this direction and explain why no conclusive results could be obtained.

However, the focus of this section are the various theses of students that did produce meaningful results which were not published as a part of this thesis. For the most part these results are not yet published because they only touched on the main objective of this thesis but did not contribute to its core. As is explained in the respective sections below, this was sometimes planned from the start and sometimes a result of the exploratory nature of a thesis where it was that found that the initial idea could not be put into practice. As a result, the focus of the thesis was then shifted in another direction away from the photocatalytic effect. These results have, until now, only been published in the respective theses. However, they are still relevant and helped to guide this work in the right direction. Therefore, these theses and their results are highlighted briefly in the following sections.

#### 6.1 Master Thesis Walter Garcia

Walter Garcia started his master's thesis as the first student under my direct supervision only a few weeks before the first Covid-19 lockdown in 2020. Despite this hurdle, he managed to write an excellent thesis that he finished in time i.e. within his fourth AMASE semester.

The initial objective of his work was to investigate if the photocatalytic effect of samples produced by DLIP using the femtosecond laser could be used to achieve antibacterial properties and self-disinfecting surfaces. However, parallel to his work, initial methylene blue experiments showed that the surfaces produced by femtosecond laser pulses did not show significant methylene blue degradation. The femtosecond laser was used for these initial experiments because it was expected to produce greater amounts of metastable oxide instead of the stable but inactive rutile phase. However, these initial experiments showed that the total amount of oxide was too small to achieve meaningful activities.

As a result, the topic of the master thesis was changed to the adhesion of bacteria on these surface. For this, a variety of surface patterns with a periodicity of 3  $\mu$ m was produced. Substrates were pure titanium and titanium that had been thermally oxidised to form a thick rutile oxide layer (sets 1 and 2). Additionally, laser patterns on pure titanium were subsequently heat-treated to produce a thin, more metastable oxide layer (set 3).

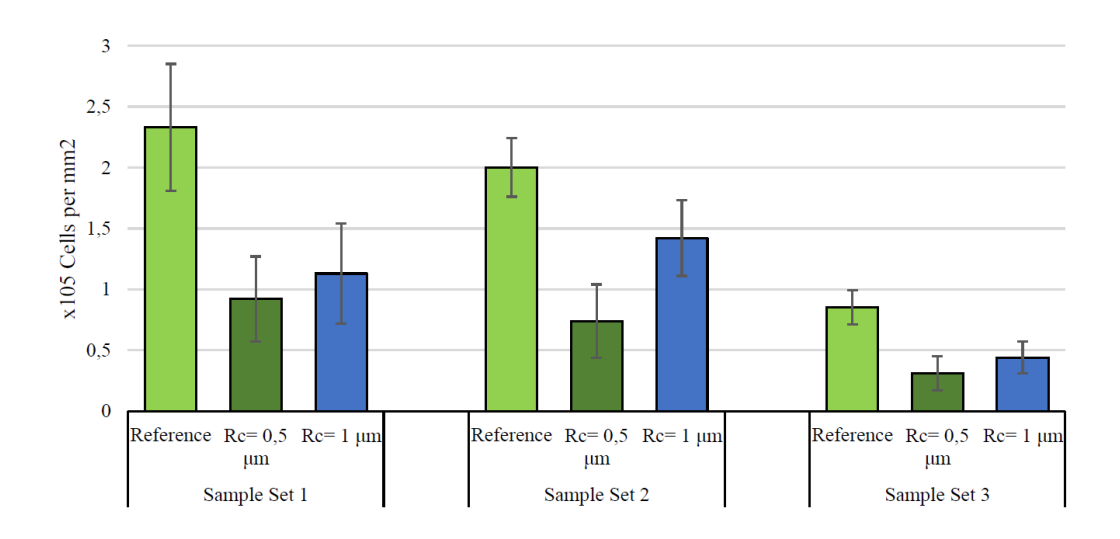


Figure 10: Key results regarding bacterial adhesion on laser patterns on different substrates with depths of 0.5 and 1  $\mu$ m. Reproduced from [86]

Figure 10 shows the number of bacteria that attached to the sample surfaces and could not be removed by rinsing with water. It can be seen that both the laser patterning and the substrate heat treatment after the patterning had significant effects on the bacteria and resulted in a significant reduction in bacterial adhesion.

#### 6.2 Bachelor and Master Theses Niklas Müller

In his bachelor thesis, Niklas Müller performed in-depth investigations of the ablation phenomena caused by femtosecond DLIP of titanium including the simulation of ablation. He also considered the effect of the laser polarization on the resulting laser structure and investigated the effects of multi-pulse accumulation and how the roughening and the oxidation caused by the previous pulses influence the subsequent ones. [87]

In his master's thesis, he extended this rather fundamental approach to include copper as a second substrate and the use of picosecond DLIP. He managed to use both, the beam profile of the lasers and the shape of the intensity distribution caused by DLIP to independently determine the ablation thresholds of both substrate materials (copper and titanium) for the two pulse durations investigated. Overall he obtained a deep understanding of the physical phenomena that are relevant for DLIP which is why his work will likely be published within the next months. [88]

#### 6.3 Master Thesis Francisco Udo Almeida

The master thesis of Francisco [89] was less related to titanium and more a result of a former cooperation with the technical university UPC in Barcelona, more specifically the collaboration with Marta Pegueroles regarding the surface modification of polymeric stents. Former work has employed patterned mandrels as scaffolds onto which the polymer ink was printed to produce stents that show a surface pattern on their insides. The objective of Francisco's work was to assess the limits of this approach. For this, a wide variety of laser patterns was produced on flat steel samples using picosecond DLIP. Line, cross and point patterns with various depths were produced and characterized. The resulting surfaces were then used as moulds for biopolymer (PLLA) to investigate where the limits of this approach lie. It was found that especially for deep point patterns the polymer film cannot be removed from the surfaces without destroying it as the bond between the laser-patterned mould and the polymer film becomes too strong. A second, more prevalent problem lies in the oxidation of the sample surface during laser patterning

and the subsequent transfer of oxide to the PLLA film. Oxide that gets embedded in the biopolymer could later detach and cause a multitude of problems for the patient. For this reason, initial tests using nitrogen as a protective gas during the patterning were also conducted in this thesis.

#### **6.4** TEM-Analysis

TEM-analysis of the photocatalytic surfaces investigated in this work could lead to a deeper insight into the chemical and phase composition as well as the distribution and morphology of oxides within the complex oxidised layer. For this reason, several attempts have been made to find out where which oxides are present in the surface using selected area electron diffraction and HR-TEM. Ideally, HR-TEM could also resolve type two heterojunctions between rutile and anatase. These conductive connections of the two phases would likely have very meaningful impact on the activity of the surface as described in section 2.4.5 and was imaged via HR-TEM before by Qiao et al. [43].

#### 6.4.1 Selected Area Electron Diffraction (SAED)

Initial experiments were performed with a JEOL JEM 2010F TEM using an acceleration voltage of 200 kV as a part of the master thesis of Fabian Bonner with the aim to better understand the phase composition and how it is affected by various heat treatments. As is shown in Figure 11, various diffraction patterns were obtained from different sample locations.

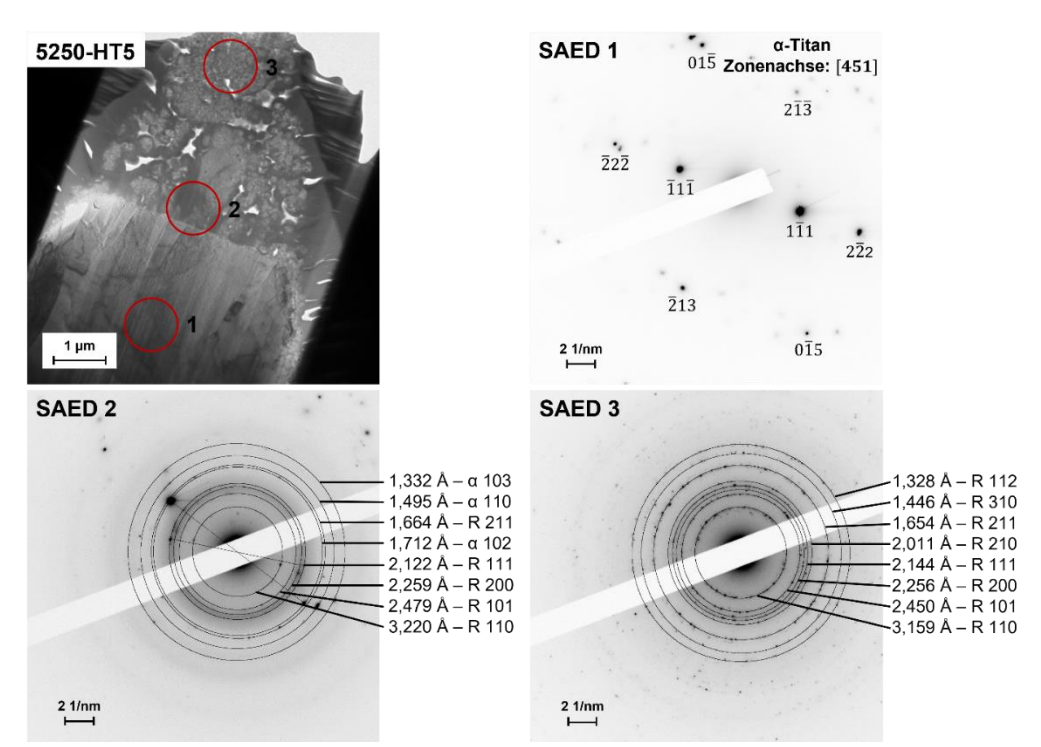


Figure 11: Image reproduced from [90] showing the transition from titanium in the substrate (SAED 1) to titanium and rutile (SAED 2) to pure rutile (SAED 3). The sample was one of the samples investigated in the third publication that is included in this thesis. It was produced with a pulse energy of 10 uJ and heat treated after the patterning for 3 hours at 600°C.

However, it must be said that the results from this analysis were non-conclusive and could not be used in the respective publication. As an example, several measurements observe high amounts of oxide in the substrate material. In retrospect, it cannot be said if this is a result of contamination or if the data was falsely labelled and various SAEDs were confused.

#### 6.4.2 HR-TEM

High-resolution TEM images were taken by Jörg Schmauch with a JEOL JEM-ARM200F with an acceleration voltage of 200 kV. The aim was to locally determine the atomic distance and thereby the phase. Ideally, a type 2 heterojunction between anatase and rutile would also be observable. However, the sample preparation proved extremely challenging as especially the thinnest, uppermost parts of the porous oxide layer would easily break off. The platinum that was deposited into the porous structure to stabilize it led to additional problems as it contaminated the sample and made it impossible to obtain a clear image. As a result, atomic distances could only be determined in a few areas with relatively large crystallites. In those cases, Inverse Fast Fourier Transformation (IFFT) mostly resulted in atomic distances corresponding to anatase. As a result of these problems, the HR-TEM analysis could not deliver on its promise to locally determine the phase and was instead restricted to a few locations close to the substrate or within larger particles. An overview of the HR-TEM results is given in Figure 12.

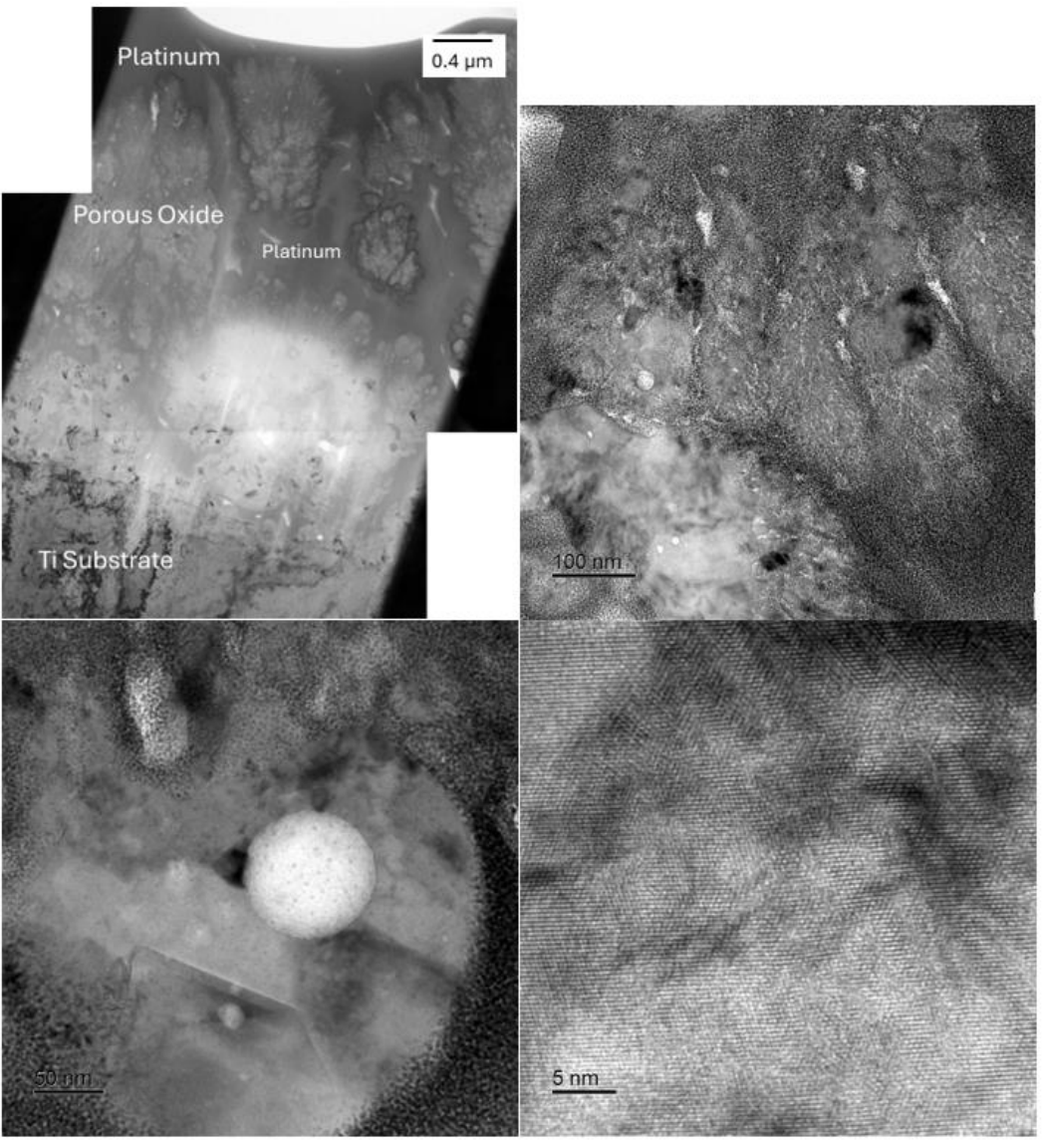


Figure 12: Results from HR-TEM analysis of a sample produced with high pulse energy (30.7  $\mu$ J) at room temperature. The overview in a) shows how platinum was used to fill the porous structure. b) and c) show the contamination of large areas caused by platinum redeposition during the thinning procedure. d) shows a high-resolution image of a crystalline area close to the substrate. The lattice constants were measured using Inverse Fast Fourier Transformation indicate anatase (3.54 nm, 2.45 nm, 1.86 nm).

### 7 Conclusions and Outlook

In this work, it was shown for the first time that direct laser interference patterning can be used to produce photocatalytic surfaces on a titanium substrate in a single processing step. It was hypothesized that both the morphology and the chemistry of the resulting oxide layers depend on the laser parameters such as the accumulated fluence on the surface, the fluence of a single laser pulse and the number of pulses that interacted with a given point in the surface.

To test this hypothesis, a wide variety of processing parameters was employed to produce various surfaces. These surfaces were then analysed regarding both, their topography and chemistry. The photocatalytic degradation efficiency of the surfaces was evaluated via methylene blue degradation. After a suitable lab setup had been developed and tested, the degradation experiments could be correlated to the surface parameters. Based on these observations a model for the underlying phenomena could be established. Namely, the experiments revealed that the high photocatalytic activities do require high amounts of TiO<sub>2</sub> in its anatase phase as was expected. However, the presence of amorphous and most importantly oxygen-deficient TiO phases plays a far greater role than was initially assumed. The presence of these phases was found to be directly linked to the employed laser parameters as higher laser intensities led to higher titanium concentrations in the resulting plasma plume and thereby the formation of oxygen-deficient phases. Similarly, higher pulse numbers result in the continuous re-ablation of material and as a result the gradual increase in oxygen content. Another increase in activity could be observed when employing cross-structures instead of line patterns. This is likely a result of different kinetics within the plasma plume during processing as the plume itself is confined by the pattern. The author hypothesizes that the confinement not only influences the amount of oxygen within the plasma but also the expansion of the gaseous phases. This directly influences the cooling speed of this plume, the density of material within it and the distance any ablated particles travel within the plume before being ejected. As a result, the confinement by the pattern is expected to strongly influence the crystal growth, chemistry and phase composition especially as the most active anatase phase is only thermodynamically stable at grain sizes below 40 nm as mentioned in section 2.4.5. While this hypothesis is supported by the observed phase compositions and photocatalytic activities, further work is needed to verify it. However, as this future work should include extensive thermodynamic and MD simulations it did exceed the scope of this work. While the cross patterns showed an increase in activity compared to line structures, the effect was not large enough the justify the increase in patterning time as the production of cross patterns requires a second scanning process that is perpendicular to the first resulting in an effective doubling of the processing time. Further experiments were therefore performed with line patterns to keep the process as time- and cost-effective as possible. Based on the observations made in previous experiments, it was concluded that the existing process could benefit from thermal activation either during the patterning process or in a subsequent heat treatment step. To test this hypothesis, samples were laser pattered at various temperatures up to 600°C. Additional heat treatments after the patterning were performed in a vacuum to prevent the formation of a stable oxide layer consisting of the most stable oxidic phase rutile which shows very minor photocatalytic activity. These experiments were highly successful. The samples produced showed far higher photocatalytic activities than the untreated samples which can be traced back to the desired reduction in oxygen-deficient phases and an overall increase in crystallinity. In this way, the maximum photocatalytic activity achieved by laser-patterned samples could be steadily increased over the course of this project. From initial line structures to cross patterns and eventually heat-treated line patterns, the maximum activity was

significantly increased in each step. For the line patterns, the concentration of the methylene blue solution decreased by around 50% in the 2 hours under UV light. In contrast, the cross structures achieved a degradation of almost 75% in the same time period and finally, the heat-treated samples degraded approximately 80% of the methylene blue under the same conditions. Considering these results, it can be assumed that cross structures could be promising candidates for future experiments to investigate if the increase in processing time is worth the increase in activity. Although a change in pattern periodicity did not show major effects on the activity, this field could also be further investigated, as well as different pattern types such as point structures. Further research in this direction should also focus on examining the phase composition and distribution in more detail. In particular, TEM analysis was attempted multiple times in this work but consistently failed to produce satisfying results, as the preparation TEM lamellae from the patterns proved extremely challenging. The porous oxidic structures would either break off during preparation or had to be filled with large amounts of platinum, which then complicated the subsequent analysis.

Finally, the laboratory setup to evaluate the degradation efficiency was scaled up from only 125 µl of methylene blue solution per sample up to 1.5 litres. This was done as a proof of concept to showcase the approach's potential to produce photocatalytic surfaces on a larger scale using off-the-shelf materials and still achieve comparable results. It was thereby shown that the direct laser structuring of titanium could be used to build, for example, photocatalytic reactors for water treatment or to combat environmental pollution. Future experiments should further assess the scalability, especially regarding the long-term stability of the reactive surface. Secondly, the degradation of actual pollutants instead of model chemicals presents a logical next step. However, as the working principle of TiO<sub>2</sub> photocatalysis is well tested, it can be expected that various pollutants such as complex organic molecules (e.g. medication), nitric oxides and even PFAS can be degraded. The approach still presents a promising alternative to existing photocatalytic surfaces, which are very cost-intensive and fragile. This could eliminate the need for solar concentrators that are often used to focus sunlight and make the best use of a small amount of reactive area. Instead, a simplified reactor design employing large-scale patterned surfaces could be a viable way to facilitate the use of photocatalytic materials and remove a variety of pollutants from waterways, public places and even the air.

At the time of this writing, a DFG proposal is being prepared in collaboration with the IFOS in Kaiserslautern and RPTU Kaiserslautern (Jun. Prof. Simon Stefan) with the aim of investigating the wetting behaviour of those surfaces. If approved, this work will focus on the time-dependent adsorption of hydrocarbons on the functionalized surfaces and its effect on the wetting behaviour as was done on copper in a former collaboration (DFG 435334669). Applying this research to photocatalytic surfaces, however, also enables the active removal of those hydrocarbon contaminations to directly influence and control the wetting behaviour. Additionally, the molecular dynamics simulations performed by Prof. Stefan aim to gain a deeper understanding of both, the accumulation and degradation phenomena on a molecular level.

# 8 Bibliography

- [1] J. Low, B. Cheng, J. Yu, Surface modification and enhanced photocatalytic CO2 reduction performance of TiO2: a review, Appl. Surf. Sci. 392 (2017) 658–686. https://doi.org/10.1016/j.apsusc.2016.09.093.
- [2] S. McMichael, P. Fernández-Ibáñez, J.A. Byrne, A review of photoelectrocatalytic reactors for water and wastewater treatment, Water. 13 (2021) 1198. https://doi.org/10.3390/w13091198.
- [3] Y. Nosaka, A.Y. Nosaka, Generation and Detection of Reactive Oxygen Species in Photocatalysis, Chemical Reviews. 117 (2017) 11302–11336. https://doi.org/10.1021/acs.chemrev.7b00161.
- [4] P.V. Laxma Reddy, B. Kavitha, P.A. Kumar Reddy, K.H. Kim, TiO2-based photocatalytic disinfection of microbes in aqueous media: A review, Environmental Research. 154 (2017) 296–303. https://doi.org/10.1016/j.envres.2017.01.018.
- [5] C.S. Uyguner-demirel, C.N. Birben, M. Bekbolet, AC SC, (2018). https://doi.org/10.1016/j.chemosphere.2018.07.121.
- [6] H2Nano, H2Nano, (n.d.). https://www.h2nano.ca/.
- [7] Sparc Hydrogen, www.sparchydrogen.com, (2024). www.sparchydrogen.com.
- [8] D. Uner, I. Bayar, T. Tabari, The influence of relative humidity on photocatalytic oxidation of nitric oxide (NO) over TiO 2, Applied Surface Science. 354 (2015) 260–266. https://doi.org/10.1016/j.apsusc.2015.07.045.
- [9] S. Devahasdin, C. Fan, K. Li, D.H. Chen, TiO 2 photocatalytic oxidation of nitric oxide: Transient behavior and reaction kinetics, Journal of Photochemistry and Photobiology A: Chemistry. 156 (2003) 161–170. https://doi.org/10.1016/S1010-6030(03)00005-4.
- [10] H.M. Yadav, J.S. Kim, S.H. Pawar, Developments in photocatalytic antibacterial activity of nano TiO2: A review, Korean Journal of Chemical Engineering. 33 (2016) 1989–1998. https://doi.org/10.1007/s11814-016-0118-2.
- [11] V. Etacheri, C. Di Valentin, J. Schneider, D. Bahnemann, S.C. Pillai, Visible-light activation of TiO2 photocatalysts: Advances in theory and experiments, Journal of Photochemistry and Photobiology C: Photochemistry Reviews. 25 (2015) 1–29. https://doi.org/10.1016/j.jphotochemrev.2015.08.003.
- [12] S.G. Ullattil, S.B. Narendranath, S.C. Pillai, P. Periyat, Black TiO2 Nanomaterials: A Review of Recent Advances, Chemical Engineering Journal. 343 (2018) 708–736. https://doi.org/10.1016/j.cej.2018.01.069.
- [13] T. Leshuk, H. Krishnakumar, D. de O. Livera, F. Gu, Floating photocatalysts for passive solar degradation of naphthenic acids in oil sands process-affected water, Water (Switzerland). 10 (2018). https://doi.org/10.3390/w10020202.
- [14] S. Linley, T. Leshuk, F.X. Gu, Magnetically separable water treatment technologies and their role in future advanced water treatment: A patent review, Clean Soil, Air, Water. 41 (2013) 1152–1156. https://doi.org/10.1002/clen.201100261.
- [15] A. Haruna, F.K. Chong, Y.C. Ho, Z.M.A. Merican, Preparation and modification methods of defective titanium dioxide-based nanoparticles for photocatalytic wastewater treatment—a comprehensive review, Environmental Science and Pollution Research. 29 (2022) 70706–70745. https://doi.org/10.1007/s11356-022-22749-8.
- [16] J. Wang, J. Li, S. Qian, G. Guo, Q. Wang, J. Tang, H. Shen, X. Liu, X. Zhang, P.K. Chu, Antibacterial Surface Design of Titanium-Based Biomaterials for Enhanced Bacteria-Killing and Cell-Assisting Functions Against Periprosthetic Joint Infection, ACS Applied Materials and Interfaces. 8 (2016) 11162–11178. https://doi.org/10.1021/acsami.6b02803.

- [17] S. Reghunath, D. Pinheiro, S.D. KR, A review of hierarchical nanostructures of TiO2: Advances and applications, Applied Surface Science Advances. 3 (2021). https://doi.org/10.1016/j.apsadv.2021.100063.
- [18] M.P. Diebold, Optimizing the benefits of TiO2 in paints, Journal of Coatings Technology and Research. 17 (2020) 1–17. https://doi.org/10.1007/s11998-019-00295-2.
- [19] M.C. Chen, P.W. Koh, V.K. Ponnusamy, S.L. Lee, Titanium dioxide and other nanomaterials based antimicrobial additives in functional paints and coatings: Review, Progress in Organic Coatings. 163 (2022) 106660. https://doi.org/10.1016/j.porgcoat.2021.106660.
- [20] M.J. Llana, M.S. Tolentino, N.C.C. Valeza, J.P. Reyes, B.A. Basilia, Release Analysis of Nano-Titanium Dioxide (TiO 2) from Paint: An Accelerated Weathering Experiment, IOP Conference Series: Materials Science and Engineering. 1117 (2021) 012029. https://doi.org/10.1088/1757-899x/1117/1/012029.
- [21] D.A.H. Hanaor, C.C. Sorrell, Review of the anatase to rutile phase transformation, Journal of Materials Science Science. 46 (2010) 855–874. https://doi.org/10.1007/s10853-010-5113-0.
- [22] A. Fujishima, K. Honda, Electrochemical Photolysis of Water at a Semiconductor Electrode, Nature. 238 (1972) 38–40. https://doi.org/10.1038/238038a0.
- [23] Y.J. Yuan, D. Chen, Z.T. Yu, Z.G. Zou, Cadmium sulfide-based nanomaterials for photocatalytic hydrogen production, Journal of Materials Chemistry A. 6 (2018) 11606–11630. https://doi.org/10.1039/c8ta00671g.
- [24] A. Naldoni, M. Altomare, G. Zoppellaro, N. Liu, Š. Kment, R. Zbořil, P. Schmuki, Photocatalysis with reduced TiO 2: From Black TiO 2 to cocatalyst-free hydrogen production, ACS Catalysis. 9 (2019) 345–364. https://doi.org/10.1021/acscatal.8b04068.
- [25] J. Low, B. Cheng, J. Yu, Surface modification and enhanced photocatalytic CO 2 reduction performance of TiO 2: a review, Applied Surface Science. 392 (2016) 658–686. https://doi.org/10.1016/j.apsusc.2016.09.093.
- [26] Y. Uesugi, H. Nagakawa, M. Nagata, Highly Efficient Photocatalytic Degradation of Hydrogen Sulfide in the Gas Phase Using Anatase/TiO2(B) Nanotubes, ACS Omega. 7 (2022) 11946–11955. https://doi.org/10.1021/acsomega.1c07294.
- [27] S. Jain, R.S. Williamson, M. Marquart, A. V. Janorkar, J.A. Griggs, M.D. Roach, Photofunctionalization of anodized titanium surfaces using UVA or UVC light and its effects against Streptococcus sanguinis, Journal of Biomedical Materials Research Part B Applied Biomaterials. 106 (2018) 2284–2294. https://doi.org/10.1002/jbm.b.34033.
- [28] M. Gao, L. Zhu, W.L. Ong, J. Wang, G.W. Ho, Structural design of TiO2-based photocatalyst for H2 production and degradation applications, Catalysis Science and Technology. 5 (2015) 4703–4726. https://doi.org/10.1039/c5cy00879d.
- [29] J. Zhang, P. Zhou, J. Liu, J. Yu, New understanding of the difference of photocatalytic activity among anatase, rutile and brookite TiO2, Physical Chemistry Chemical Physics. 16 (2014) 20382–20386. https://doi.org/10.1039/c4cp02201g.
- [30] S. Gligorovski, R. Strekowski, S. Barbati, D. Vione, Environmental Implications of Hydroxyl Radicals (•OH), Chemical Reviews. 115 (2015) 13051–13092. https://doi.org/10.1021/cr500310b.
- [31] S.G. Kumar, K.S.R.K. Rao, Comparison of modification strategies towards enhanced charge carrier separation and photocatalytic degradation activity of metal oxide semiconductors (TiO 2, WO 3 and ZnO), Applied Surface Science. 391 (2017) 124–148. https://doi.org/10.1016/j.apsusc.2016.07.081.
- [32] G. Veréb, L. Manczinger, G. Bozsó, A. Sienkiewicz, L. Forró, K. Mogyorósi, K. Hernádi, A. Dombi, Comparison of the photocatalytic efficiencies of bare and doped

- rutile and anatase TiO2 photocatalysts under visible light for phenol degradation and E. coli inactivation, Applied Catalysis B: Environmental. 129 (2013) 566–574. https://doi.org/10.1016/j.apcatb.2012.09.045.
- [33] W. Choi, A. Termin, M.R. Hoffmann, The role of metal ion dopants in quantum-sized TiO2: Correlation between photoreactivity and charge carrier recombination dynamics, Journal of Physical Chemistry. 98 (1994) 13669–13679. https://doi.org/10.1021/j100102a038.
- [34] A. Fujishima, T.N. Rao, D.A. Tryk, Titanium dioxide photocatalysis, Journal of Photochemistry and Photobiology C: Photochemistry Reviews. 1 (2000) 1–21. https://doi.org/10.1016/S1389-5567(00)00002-2.
- [35] X. Chen, L. Liu, P.Y. Yu, S.S. Mao, Increasing solar absorption for photocatalysis with black hydrogenated titanium dioxide nanocrystals, Science. 331 (2011) 746–750. https://doi.org/10.1126/science.1200448.
- [36] T. Nakajima, T. Tsuchiya, T. Kumagai, Pulsed laser-induced oxygen deficiency at TiO2 surface: Anomalous structure and electrical transport properties, Journal of Solid State Chemistry. 182 (2009) 2560–2565. https://doi.org/10.1016/j.jssc.2009.07.006.
- [37] T. Nakajima, T. Nakamura, K. Shinoda, T. Tsuchiya, pulsed laser-induced oxygen release and enhanced, Journal of Materials Chemistry A. (2014) 6762–6771. https://doi.org/10.1039/c4ta00557k.
- [38] X. Chen, D. Zhao, K. Liu, C. Wang, L. Liu, B. Li, Z. Zhang, D. Shen, Laser-Modified Black Titanium Oxide Nanospheres and Their Photocatalytic Activities under Visible Light, ACS Applied Materials and Interfaces. 7 (2015) 16070–16077. https://doi.org/10.1021/acsami.5b04568.
- [39] R. Abe, K. Sayama, H. Arakawa, Efficient hydrogen evolution from aqueous mixture of I- and acetonitrile using a merocyanine dye-sensitized Pt/TiO2 photocatalyst under visible light irradiation, Chemical Physics Letters. 362 (2002) 441–444. https://doi.org/10.1016/S0009-2614(02)01140-5.
- [40] Y.P. Yuan, L.W. Ruan, J. Barber, S.C. Joachim Loo, C. Xue, Heteronanostructured suspended photocatalysts for solar-to-fuel conversion, Energy and Environmental Science. 7 (2014) 3934–3951. https://doi.org/10.1039/c4ee02914c.
- [41] T. Kawahara, T. Ozawa, M. Iwasaki, H. Tada, S. Ito, Photocatalytic activity of rutile-anatase coupled TiO2 particles prepared by a dissolution-reprecipitation method, Journal of Colloid and Interface Science. 267 (2003) 377–381. https://doi.org/10.1016/S0021-9797(03)00755-0.
- [42] Y. Gao, J. Zhu, H. An, P. Yan, B. Huang, R. Chen, F. Fan, C. Li, Directly Probing Charge Separation at Interface of TiO2 Phase Junction, Journal of Physical Chemistry Letters. 8 (2017) 1419–1423. https://doi.org/10.1021/acs.jpclett.7b00285.
- [43] M. Qiao, J. Yan, L. Qu, B. Zhao, J. Yin, T. Cui, L. Jiang, Femtosecond Laser Induced Phase Transformation of TiO2with Exposed Reactive Facets for Improved Photoelectrochemistry Performance, ACS Applied Materials and Interfaces. 12 (2020) 41250–41258. https://doi.org/10.1021/acsami.0c10026.
- [44] D.K. Sharma, S. Shukla, K.K. Sharma, V. Kumar, A review on ZnO: Fundamental properties and applications, Materials Today: Proceedings. 49 (2020) 3028–3035. https://doi.org/10.1016/j.matpr.2020.10.238.
- [45] A. Das, M. Patra, R.R. Wary, P. Gupta, R.G. Nair, Photocatalytic performance analysis of Degussa P25 under various laboratory conditions, Conf. Ser.: Mater. Sci. Eng. 377 (2018) 012101. https://doi.org/10.1088/1757-899X/377/1/012101.
- [46] G. Zerjav, K. Zizek, J. Zavasnik, A. Pintar, Brookite vs. rutile vs. anatase: What's behind their various photocatalytic activities?, Journal of Environmental Chemical Engineering. 10 (2022). https://doi.org/10.1016/j.jece.2022.107722.
- [47] T. Kawahara, Y. Konishi, H. Tada, N. Tohge, J. Nishii, S. Ito, A patterned TiO2

- (anatase)/TiO2 (rutile) bilayer-type photocatalyst: effect of the anatase/rutile junction on the photocatalytic activity, Angewandte Chemie. 15 (2002) 2935–2937.
- [48] S.J. Smith, R. Stevens, S. Liu, G. Li, A. Navrotsky, J. Boerio-Goates, B.F. Woodfield, Heat capacities and thermodynamic functions of TiO2 anatase and rutile: Analysis of phase stability, American Mineralogist. 94 (2009) 236–243. https://doi.org/10.2138/am.2009.3050.
- [49] O. Van Overschelde, G. Guisbiers, M. Wautelet, Nanocrystallization of Anatase or Rutile TiO 2 by Laser Treatment, Journal of Physical Chemistry C. 113 (2009) 15343–15345.
- [50] M.E. Barbour, N. Gandhi, A. El-Turki, D.J. O'Sullivan, D.C. Jagger, Differential adhesion of Streptococcus gordonii to anatase and rutile titanium dioxide surfaces with and without functionalization with chlorhexidine, Journal of Biomedical Materials Research Part A. 90 (2009) 993–998. https://doi.org/10.1002/jbm.a.32170.
- [51] G. Wang, J. Li, K. Lv, W. Zhang, X. Ding, G. Yang, X. Liu, X. Jiang, Surface thermal oxidation on titanium implants to enhance osteogenic activity and in vivo osseointegration, Scientific Reports. 6 (2016) 1–13. https://doi.org/10.1038/srep31769.
- [52] M.D. Roach, R.S. Williamson, I.P. Blakely, L.M. Didier, Tuning anatase and rutile phase ratios and nanoscale surface features by anodization processing onto titanium substrate surfaces, Materials Science and Engineering C. 58 (2016) 213–223. https://doi.org/10.1016/j.msec.2015.08.028.
- [53] S. Jain, R.S. Williamson, M. Marquart, A. V. Janorkar, J.A. Griggs, M.D. Roach, Photofunctionalization of anodized titanium surfaces using UVA or UVC light and its effects against Streptococcus sanguinis, Journal of Biomedical Materials Research Part B Applied Biomaterials. 106 (2018) 2284–2294. https://doi.org/10.1002/jbm.b.34033.
- [54] Ł. Haryński, D. Czylkowski, B. Hrycak, J. Karczewski, J. Gumieniak, A. Kramek, J. Ryl, K. Grochowska, M. Dors, K. Siuzdak, Nitrogen plasma-induced crystallization of anodic TiO2 nanotubes for solar photoelectrochemistry, Applied Surface Science. 615 (2023). https://doi.org/10.1016/j.apsusc.2023.156472.
- [55] M.L. Puga, J. Venturini, C.S. ten Caten, C.P. Bergmann, Influencing parameters in the electrochemical anodization of TiO2 nanotubes: Systematic review and meta-analysis, Ceramics International. 48 (2022) 19513–19526. https://doi.org/10.1016/j.ceramint.2022.04.059.
- [56] T. Gupta, Samriti, J. Cho, J. Prakash, Hydrothermal synthesis of TiO2 nanorods: formation chemistry, growth mechanism, and tailoring of surface properties for photocatalytic activities, Materials Today Chemistry. 20 (2021) 100428. https://doi.org/10.1016/j.mtchem.2021.100428.
- [57] S. Dey, S.C. Roy, Designing TiO 2 nanostructures through hydrothermal growth: influence of process parameters and substrate position Designing TiO 2 nanostructures through hydrothermal growth: in fluence of process parameters and substrate position, Nano Express. 010028 (2021). https://doi.org/10.1088/2632-959X/abe844.
- [58] S. Obregón, V. Rodríguez-González, Photocatalytic TiO2 thin films and coatings prepared by sol–gel processing: a brief review, Journal of Sol-Gel Science and Technology. 102 (2022) 125–141. https://doi.org/10.1007/s10971-021-05628-5.
- [59] M. Dell'Edera, C. Lo Porto, I. De Pasquale, F. Petronella, M.L. Curri, A. Agostiano, R. Comparelli, Photocatalytic TiO2-based coatings for environmental applications, Catalysis Today. 380 (2021) 62–83. https://doi.org/10.1016/j.cattod.2021.04.023.
- [60] T. Křenek, L. Vála, T. Kovářík, R. Medlín, R. Fajgar, J. Pola, V. Jandová, V. Vavruňková, M. Pola, M. Koštejn, Novel perspectives of laser ablation in liquids: The

- formation of a high-pressure orthorhombic FeS phase and absorption of FeS-derived colloids on a porous surface for solar-light photocatalytic wastewater cleaning, Dalton Transactions. 49 (2020) 13262–13275. https://doi.org/10.1039/d0dt01999b.
- [61] T. Křenek, L. Vála, R. Medlín, J. Pola, V. Jandová, V. Vavruňková, P. Mikysek, P. Belsky, M. Koštejn, A novel route of colloidal chemistry: room temperature reactive interactions between titanium monoxide and silicon monoxide sols produced by laser ablation in liquid resulting in the formation of titanium disilicide, Dalton Transactions. 51 (2022) 13831. https://doi.org/10.1039/d2dt02065c.
- [62] A. Datcu, L. Duta, A. Pérez Del Pino, C. Logofatu, C. Luculescu, A. Duta, D. Perniu, E. György, One-step preparation of nitrogen doped titanium oxide/Au/reduced graphene oxide composite thin films for photocatalytic applications, RSC Advances. 5 (2015) 49771–49779. https://doi.org/10.1039/c5ra07853a.
- [63] P. Fathi-Hafshejani, H. Johnson, Z. Ahmadi, M. Roach, N. Shamsaei, M. Mahjouri-Samani, Laser-assisted selective and localized surface transformation of titanium to anatase, rutile, and mixed phase nanostructures, Journal of Laser Applications. 33 (2021). https://doi.org/10.2351/7.0000316.
- [64] M. Mahjouri-Samani, P. Fathi-Hafshejani, H. Johnson, Z. Ahmadi, M. Roach, N. Shamsaei, Phase-selective and localized TiO2 coating on additive and wrought titanium by a direct laser surface modification approach, ACS Omega. 5 (2020) 16744–16751. https://doi.org/10.1021/acsomega.0c01671.
- [65] A. Medvids, P. Onufrijevs, J. Kaupužs, R. Eglitis, J. Padgurskas, A. Zunda, H. Mimura, I. Skadins, S. Varnagiris, Anatase or rutile TiO2 nanolayer formation on Ti substrates by laser radiation: Mechanical, photocatalytic and antibacterial properties, Optics and Laser Technology. 138 (2021). https://doi.org/10.1016/j.optlastec.2020.106898.
- [66] A.F. Lasagni, Technische Universität Dresden, Fraunhofer IWS, DLIP Quickly Changing Surface Functionalization, Photonics.Com. (2016). https://www.photonics.com/Articles/DLIP\_Quickly\_Changing\_Surface\_Functionalization/a60796.
- [67] A. Lasagni, Advanced design of periodical structures by laser interference metallurgy in the micro / nano scale on macroscopic areas, Universität des Saarlandes, 2006.
- [68] A.F. Lasagni, Advanced design of periodical structures by laser interference metallurgy in the micro / nano scale on macroscopic areas, Saarland University, 2006.
- [69] B. Voisiat, A.I. Aguilar-Morales, T. Kunze, A.F. Lasagni, Development of an analytical model for optimization of direct laser interference patterning, Materials. 13 (2020) 1–10. https://doi.org/10.3390/ma13010200.
- [70] D.W. Müller, T. Fox, P.G. Grützmacher, S. Suarez, Applying Ultrashort Pulsed Direct Laser Interference Patterning for Functional Surfaces, Scientific Reports. (2020) 1–14. https://doi.org/10.1038/s41598-020-60592-4.
- [71] A.F. Lasagni, C. Gachot, K.E. Trinh, M. Hans, A. Rosenkranz, S. Eckhardt, T. Kunze, M. Bieda, D. Günther, V. Lang, Direct laser interference patterning, 20 years of development: from the basics to industrial applications, SPIE. 10092 (2017). https://doi.org/10.1117/12.2252595.
- [72] A. Pérez Del Pino, P. Serra, J.L. Morenza, Oxidation of titanium through Nd:YAG laser irradiation, Applied Surface Science. 197–198 (2002) 887–890. https://doi.org/10.1016/S0169-4332(02)00447-6.
- [73] A.J. Antończak, Ł. Skowroński, M. Trzcinski, V. V. Kinzhybalo, Ł.K. Łazarek, K.M. Abramski, Laser-induced oxidation of titanium substrate: Analysis of the physicochemical structure of the surface and sub-surface layers, Applied Surface Science. 325 (2015) 217–226. https://doi.org/10.1016/j.apsusc.2014.11.062.

- [74] N. Rasti, E. Toyserkani, F. Ismail, Chemical modification of titanium immersed in hydrogen peroxide using nanosecond pulsed fiber laser irradiation, Materials Letters. 65 (2011) 951–954. https://doi.org/10.1016/j.matlet.2011.01.002.
- [75] Y. Li, T. Ishigaki, Thermodynamic analysis of nucleation of anatase and rutile from TiO2 melt, Journal of Crystal Growth. 242 (2002) 511–516. https://doi.org/10.1016/S0022-0248(02)01438-0.
- [76] E.C. Landis, K.C. Phillips, E. Mazur, C.M. Friend, Formation of nanostructured TiO 2 by femtosecond laser irradiation of titanium in O 2, Journal of Applied Physics. 112 (2012) 2–7. https://doi.org/10.1063/1.4752276.
- [77] T.D. Robert, L.D. Laude, V.M. Geskin, R. Lazzaroni, R. Gouttebaron, Micro-Raman spectroscopy study of surface transformations induced by excimer laser irradiation of TiO2, Thin Solid Films. 440 (2003) 268–277. https://doi.org/https://doi.org/10.1016/S0040-6090(03)00819-8.
- [78] G. Yang, C. Li, Y. Wang, Phase Formation of Nano-TiO 2 Particles during Flame Spraying with Liquid Feedstock, 14 (2005) 480–486. https://doi.org/10.1361/105996305X76487.
- [79] H.-L. Ma, J.-Y. Yang, B. Lu, G.-H. Ma, Phase transformation and nanograting structure on TiO 2 rutile single crystal induced by infrared femtosecond laser, Chinese Physics. 16 (2007) 3328–3331. https://doi.org/10.1088/1009-1963/16/11/031.
- [80] H.-L. Ma, J.Y. Yang, Y. Dai, Y.B. Zhang, B. Lu, G.H. Ma, Raman study of phase transformation of TiO 2 rutile single crystal irradiated by infrared femtosecond laser, Applied Surface Science. 253 (2007) 7497–7500. https://doi.org/10.1016/j.apsusc.2007.03.047.
- [81] T. Křenek, J. Pola, D. Docheva, T. Stich, R. Fajgar, T. Kovářík, M. Pola, J. Martan, D. Moskal, V. Jandová, J. Kupčík, P. Mikysek, Porous micro/nano structured oxidic titanium surface decorated with silicon monoxide, Surfaces and Interfaces. 26 (2021) 101304. https://doi.org/10.1016/j.surfin.2021.101304.
- [82] C. Zwahr, R. Helbig, C. Werner, A.F. Lasagni, Fabrication of multifunctional titanium surfaces by producing hierarchical surface patterns using laser based ablation methods, Scientific Reports. 9 (2019) 1–13. https://doi.org/10.1038/s41598-019-43055-3.
- [83] F.L. Toma, S. Alamri, B. Leupolt, T. Kunze, M. Barbosa, Functionalization of Suspension Sprayed HVOF TiO2 Coatings by Direct Laser Interference Patterning, Journal of Thermal Spray Technology. 30 (2021) 1159–1173. https://doi.org/10.1007/s11666-021-01181-3.
- [84] Olympus, 3D Measuring Laser Microscope OLS4100 Bringing Answers to the Surface, Olympus Product Specification. (2014). https://www.olympusims.com/en/metrology/ols4100/.
- [85] Olympus, Surface Roughness Measurement Parameters, (2024). https://www.olympus-ims.com/en/metrology/surface-roughness-measurement-portal/parameters/#!cms[focus]=004.
- [86] W. García Herrera, Ultra-Short Pulsed Direct Laser Interference Patterning of Titanium Surfaces for Functional Anti-bacterial Effect, Saarland University, 2020.
- [87] N. Müller, Beurteilung der Laserablation an Titan durch fs-Ultrakurzpulse anhand einer FEM- Simulation nach dem Zwei-Temperatur-Modell und DLIP-strukturierten Titanoberflächen von Niklas Philipp Müller, Saarland University, 2022.
- [88] N. Müller, Studie zur Ablation metallischer Werkstoffe: Ablationsschwelle und Oberflächenmodifikation an USP-DLIP- Strukturen am Beispiel von Kupfer und Titan von Niklas Philipp Müller, Saarland University, 2024.
- [89] F.U.M. Almeida, Investigation of pattern transfer from Direct Laser Interference Patterned steel surfaces to Poly-L-Lactic Acid films, Saarland University, 2023.

[90] F.K. Bonner, Erzeugung photokatalytisch aktiver Titanoberflächen durch psgepulstes DLIP in Kombination mit Wärmebehandlungen, Universität des Saarlandes, 2022.